Performance evaluation of siding materials subjected to radiant heat loads: Structural protection in the Wildland Urban Interface

by

Eder Alain Villa Coronel

A thesis submitted in partial fulfillment of the requirements for the degree of

Master of Science

Department of Mechanical Engineering
University of Alberta

ABSTRACT

A methodology was developed to evaluate the performance of different commercially available siding materials under radiant heat loads of 57 kW/m^2 (high heat load condition, HHC) and 20 kW/m^2 (low heat load condition, LHC). The siding materials that were selected for this study were engineered wood, fibre cement board, cedar siding, and vinyl siding, while Oriented Strand Board (OSB) was used as a control material. The prototypes that were fabricated for the experimental tests (burn tests) consisted of a siding material, a weather barrier, and OSB. Time to ignition and surface temperature data gathered from the burn tests of the siding material prototypes served to gauge the effect of the heat load on the prototypes and to establish their failure point.

A variance analysis (ANOVA) showed that the performance of some siding materials was significantly different. Results from the burn tests showed that cedar siding was the least ignition resistant material while fibre cement board was the most ignition resistant material under both radiant heat loads. In fact, the siding of the latter prototype did not ignite. Under the HHC, the results suggested that the use of engineered wood material represents no advantage when compared to bare OSB. Under the LHC, independent of the failure mechanism of engineered wood and vinyl siding, there was no significant difference between their times to reach the failure point. Transient temperature profiles were obtained from a transient heat conduction model that was used to predict the time to ignition. The predicted values resulted in lower error when compared with other solutions found in the literature.

ACKNOWLEDGEMENTS

I would like to thank Dr. André McDonald for giving me the opportunity to form part of his renowned research group. The academic and professional training I received from Dr. McDonald had and will continue to have great impact on my future career. Thank you.

Special thanks go to Ms. Jobey Wills from the Telus Centre of the University of Alberta for being an important element into my successful application to this university. Thanks to Mr. Razim Refai for all his advices and support either as a colleague in the research group and, eventually, as our client. Also, I want to thank to Mr. Chad Gardeski and Mr. Rex Hesieh from FPInnovations team and to Mr. Stephen Paskaluk and Mr. Mark Ackerman for their insights during our stay at the Northwest Territories and at the Protective Clothing and Equipment Research Facility. Additional thanks to all my research group colleagues for the time spent on knowledgeable conversations when was needed.

I want to thank the most valuable pillar of my life, my parents Edith Coronel and Everardo Villa. Nothing of this could have been done without your incessant support and understanding.

In general, I want to thank all my family and friends that stood with me during this journey.

TABLE OF CONTENTS

LIST OF FIGURES

LIST OF TABLES

NOMENCLATURE

i. List of symbols

A,B,C	constants of integration
c	heat capacity (J/kg-K)
F	function in the Green's function referred to the initial conditions of the system (°C)
f	function in the Green's function referred to the boundary condition
g	gravitational constant, 9.81 m/s^2
G	Green's function (°C)
h	heat transfer coefficient (W/m^2-K)
k	thermal conductivity (W/m-K)
L	thickness of material (m)
q''	incident heat flux (W/m^2)
T	temperature (°C)
$T(t)$	time-dependant temperature (°C)
T_∞	ambient temperature (°C)
t	time (s)
V	free stream velocity (m/s)

v oxygen mass fraction (kg/kg)

x x coordinate (m)

x' x coordinate dummy variable (m)

Pr Prandtl number

$$\mathrm{Pr} = \frac{\mu \cdot c}{k}$$

Re Reynolds number

$$\mathrm{Re} = \frac{V \cdot L}{\upsilon}$$

Ra Raleigh number

$$\mathrm{Ra} = \frac{g \cdot \beta \cdot \left[T(t) - T_{\infty}\right] \cdot L^3 \cdot \mathrm{Pr}}{\upsilon^2}$$

Gr Grashof number

$$\mathrm{Gr} = \mathrm{Ra} / \mathrm{Pr}$$

ii. Greek letters

α thermal diffusivity (m^2/s)

β volume expansion coefficient for ideal gases (K^{-1})

ε emissivity

ρ density (kg/m^3)

σ Stefan-Boltzmann constant (5.67×10^{-8} $W/m^2 \cdot K^4$)

τ time dummy variable (s)

λ eigenvalue of the single-region medium (m^{-1})

ν kinematic viscosity (m^2/s)

$$\upsilon = \mu / \rho$$

μ dynamic viscosity (kg/m-s)

ρ the density (kg/m^3)

δ thickness of the material (m)

iii. Subscripts

c carbon

n summation index

i i-th boundary condition

f film of fluid at a surface

o zeroth solution for the eigenvalue

∞ infinity

1. INTRODUCTION

1.1 Wildfires and the Wildland Urban Interface

As a combination of inappropriate forest management practices, road and rail construction, grassland conversion to agriculture, urbanization, rural development, and climate change [1], wildland fires or wildfires have increased damage to alarming levels. Forest management practices of the 20th-century minimized the occurrence of small ground fires; the reduction in 20th-century wildfire across western forests in the United States has been termed as ‘‘fire deficit” [2]. These fires would have broken up forests, thereby reducing the size of the area influenced by uncontrolled wildfires in the modern era. Currently, forests exhibit high landscape connectivity of conditions that support large and severe fires [1]. These uncharacteristic large wildfires or “mega fires”, which take place when trees are layered in denser conditions generating more extreme fire weather, are able to burn up to 100,000 acres (approximately 4,050 km^2) [3]. Although wildland fires are a natural and beneficial ecosystem process, the magnitude of the current wildfires can cause large impact to human-built structures and infrastructure [4].

Buildings within or nearby fire-prone landscapes are known as the Wildland Urban Interface (WUI). The WUI definition leaves out industrial structures (e.g., Oil and Gas facilities) and infrastructure values (e.g., roads, railways, or powerlines). Johnston and Flannigan (2018) [4] estimated that of the total national land area in Canada, the WUI represents 3.8%, the “wildland-industrial interface” accounts for 1.2%, and the “wildland-infrastructure interface” for 13.0%, where direct and indirect costs of wildland fires are the highest in the WUI [4].

To date, the most destructive fires in Canadian history have been Slave Lake and Fort McMurray wildfires [5]. The first one, in 2011 where, accounting for only direct costs of suppression, evacuation, insurance, and recovery, resulted in over $1 billion [5], and the second, in 2016, which has been considered as the most costly disaster in Canadian history with an estimated insurable loss of $3.5 billion [6]. The number of structures lost per year has increased significantly, due in part to larger spread into the WUI areas, fuel management policies, and climate change, all of which are projected to increase in the future [2, 6, 7].

1.2 Ignition in the WUI communities: Vulnerabilities and mitigation measures

Three fundamental pathways have been identified for the spread of fire into and within WUI communities [7–9]:

- *Firebrand or ember showers* which are small pieces of burning vegetation or structures that are launched into the fire plume and transported by wind ahead of the fire front.
- *Direct flame contact* which occur whenever the fire front of the wildfire or flames from smaller fires are in contact with adjacent structural elements.
- *Radiant heat* which can be generated from large flames from vegetation or structures on fire, e.g., radiation from a home-to-home fire.

Conversely, mitigation measures, which are steps to reduce vulnerability to disaster impacts such as injuries and loss of life and property [10], suitable for the WUI communities are:

- *Vegetation management* which consists in guidelines for fuel treatment such as reduction or elimination of ignitable material around a structure. These guidelines are defined as FireSmart Priority Zones [11]. These Priority Zones consist on four concentric, immediate areas that surround a structure where fuel thinning, removal or conversion is required: Priority Zone 1A (added in 2017 [12]), Priority Zone 1, Priority Zone 2, and Priority Zone 3 (Figure 1). Hazard reduction criteria are most stringent closest to the home and relax as distance from the home increases [9].
- *Structural protection* which are structural components to protect a home from a fire. The most hazardous structural factors recognized by the National Fire Protection Association (NFPA) and the FireSmart Wildfire Assessment System [11] that make homes vulnerable are the roofing materials and the building exterior materials, such as siding materials for exterior wall coverings [9]. After the roof, the siding material is the structural component that is most vulnerable to fires [11].

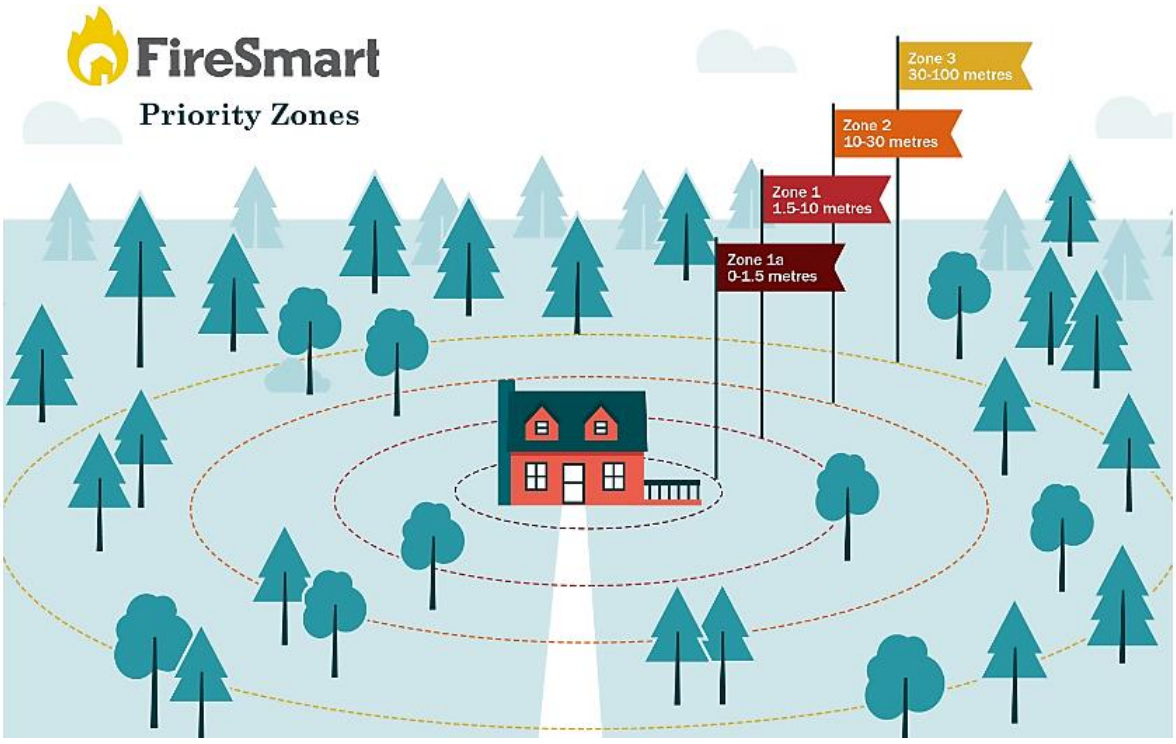

Figure 1 *FireSmart Priority Zones for fuel thinning and or fuel removal [12].*

Firebrand or embers showers have been reported as the most common cause of home ignition. However, the firebrand showers problem can be (to some extent) mitigated by the use of non-combustible roofing materials, such as asphalt. The aftermath from the Fort McMurray wildfire indicated that homes built with asphalt roofs that were exposed to ember showers and intense radiant heat, remained intact and showed no signs of fire starts [9].

The effect of direct flame contact and radiant exposure can be mitigated or eliminated through proper vegetation management. Walkinshaw, *et al.* [13] evaluated the Priority Zones 1 and 2 around two structures located at different orientations, and within different fuel (vegetative material). After a prescribed fire, it was found that the Priority Zones were adequate to prevent structural ignition. Nevertheless, the influence of other nearby structures and their impact on radiant exposure must be taken into account, i.e., adequate clearance between homes and or wildland vegetation should exist to eliminate structural ignition effectively [8]. It has been reported that if separated by less than five metres, structures can become the principal ignition source for other nearby structures [9]. The National Institute of Standards and Technology (NIST) assessed the structure separation distance in multi-structure fires [14]. In these experiments, it was observed that it took less than 80 seconds for flames from a simulated house with combustible external walls to ignite a similar structure 1.8 m (6 ft) away. As a means of addressing multi-structure separation problems, the Alberta Building Code 2014, Section 3.2.3.7, does not allow the use of combustible siding materials for residential occupancies and requires from 45 minutes to one hour of fire-resistance rating of the siding material (Table 1) [15]. Table **2** shows Table 3.2.3.1.B of the Alberta Building Code 2014 where the limiting separation

distances to which buildings must comply depends on the area of a specific exposed building face, percentage of the unprotected opening area in an exposed face, and long to wide ratio of an exposed wall [15]. According to the Alberta Building Code, an opening can be any aperture or orifice existent in a surface such as vents, windows, doors, or air-intakes in walls.

Table 1 *Minimum Construction Requirements for Exposing Building Faces (Table 3.2.3.7 from the Alberta Building Code 2014) [15]*

Occupancy Classification of Building or Fire Compartment	**Maximum Area of Unprotected Openings Permitted, % of Exposing Building Face Area**	**Minimum Required Fire-Resistance Rating**	**Type of Construction Required**	**Type of Cladding Required**
Group A, B, C or Group F, Division 3	0 to 10	1 h	Non-combustible	Non-combustible
	>10 to 25	1 h	Combustible or Non-combustible	Non-combustible
	>25 to 50	45 min	Combustible or Non-combustible	Non-combustible
	>50 to 100	45 min	Combustible or Non-combustible	Combustible or Non-combustible[(1)]
Group E, or Group F, Division 1 or 2	0 to 10	1 h	Non-combustible	Non-combustible
	>10 to 25	1 h	Combustible or Non-combustible	Non-combustible
	>25 to 50	45 min	Combustible or Non-combustible	Non-combustible
	>50 to 100	45 min	Combustible or Non-combustible	Combustible or Non-combustible

[(1)]The cladding on Group C buildings conforming to Article 3.2.2.50, and on Group D buildings conforming 3.2.2.58, shall be non-combustible.

A non-combustible material is defined as a material that meets the acceptance criteria of CAN/ULC S114 [16] which are:

- The mean of maximum temperature rise for three (or more) specimens does not exceed 36°C.

- There is no flaming of any of the three (or more) specimens during the last 14 min and 30 s of the test, where any surface flash, transitory flaming, or sustained flaming is considered flaming.
- The maximum mass loss of any of the specimens does not exceed 20%.

As it relates to the Minimum Required Fire-Resistance Rating (Table 1), the time required by the NFPA 1710 (2020 Edition, Section 4.1.2.1) for a first-due firefighting unit to respond, shall be 320 seconds (5 minutes and 20 seconds), from the turnout time to the arrival at a fire suppression incident [2]. Thus, whenever home-to-home separations are shorter than the limiting distance, complete structural ignition may occur before the arrival time of the first responders, thereby reducing the chances of survival of the building.

Table 2 *Unprotected Opening Limits for a Building or Fire Compartment that is not Sprinklered Throughout (Table 3.2.3.1.B from the Alberta Building Code 2014) [15]*

Exposing Building Face		**Area of Unprotected Opening for Groups A, D, and F, Division 3 Occupancies, %**																												
Max. Area, m^2	Ratio (L/H or H/L)[1]	**Limiting Distance, m**																												
		0	1.2	1.5	2.0	2.5	3	4	5	6	7	8	9	10	11	12	13	14	15	16	17	18	20	25	30	35	40	45	50
10	Less than 3:1	0	8	10	18	29	46	91	100																				
	3:1 to 10:1	0	8	12	21	33	50	96	100																				
	over 10:1	0	11	18	32	48	68	100																					
15	Less than 3:1	0	7	9	14	22	33	63	100																				
	3:1 to 10:1	0	8	10	17	25	37	67	100																				
	over 10:1	0	10	15	26	39	53	87	100																				
20	Less than 3:1	0	7	9	12	18	26	49	81	100																			
	3:1 to 10:1	0	8	10	15	21	30	53	85	100																			
	over 10:1	0	9	14	23	33	45	72	100																				
25	Less than 3:1	0	7	8	11	16	23	41	66	98	100																		
	3:1 to 10:1	0	8	9	13	19	26	45	70	100																			
	over 10:1	0	9	13	21	30	39	62	90	100																			
30	Less than 3:1	0	7	8	11	15	20	35	56	83	100																		
	3:1 to 10:1	0	7	9	12	17	23	39	61	88	100																		
	over 10:1	0	8	12	19	27	36	56	79	100																			
40	Less than 3:1	0	7	8	10	13	17	28	44	64	89	100																	
	3:1 to 10:1	0	7	8	11	15	20	32	48	69	93	100																	
	over 10:1	0	8	11	17	24	31	47	66	88	100																		
50	Less than 3:1	0	7	8	9	12	15	24	37	53	72	96	100																
	3:1 to 10:1	0	7	8	10	14	18	28	41	57	77	100																	
	over 10:1	0	8	10	15	21	28	41	57	76	97	100																	
60	Less than 3:1	0	7	8	9	11	14	21	32	45	62	81	100																
	3:1 to 10:1	0	7	8	10	13	16	25	36	49	66	85	100																
	over 10:1	0	8	10	14	20	25	38	51	67	85	100																	
80	Less than 3:1	0	7	7	8	10	12	18	26	36	48	62	79	98	100														
	3:1 to 10:1	0	7	8	9	11	14	21	29	40	52	67	84	100															
	over 10:1	0	8	9	13	17	22	32	44	56	70	86	100																
100	Less than 3:1	0	7	7	8	9	11	16	22	30	40	51	65	80	97	100													
	3:1 to 10:1	0	7	8	9	11	13	18	25	34	44	56	69	84	100														
	over 10:1	0	8	9	12	16	20	29	39	49	61	74	89	100															

[1] *Apply whichever ratio is greater. L= length of the exposing building face, H= height of the exposing building face.*

1.3 Breaking the disaster sequence: Making homes resistant to ignition

The Fort McMurray wildfire occurred following a pattern known as "wildland-urban interface disaster sequence". The sequence begins when wildland fire occurs under conditions of severe fire danger leading to extreme fire behavior in forest, brush, or grassland fuels. When wildfire subsequently spreads towards an urban area, multiple vulnerable homes quickly ignite and fire spreads to adjacent homes. Burning clusters of homes then combine into a continuous urban fire which overwhelms the capability of any conceivable urban firefighting response [9]. This sequence can be controlled increasing substantially the proportion of homes resistant to ignition.

As part of the structural fire protection solutions for the WUI, siding materials can help to withstand the adverse effects of direct flame contact or radiant heat originated from a fire preventing structural ignition and consequently, better controlling the spread of fire among buildings. However, there is limited research available that has assessed quantitatively the failure point of siding materials. Biswas, *et al*. [17] performed a series of material ignition tests to validate and calibrate an ignition assessment model developed by the United States Department of Homeland Security. Dietenberger [18] extended the developed protocols in ASTM E 1321 to analyze common siding materials such as cedar, redwood, pine, factory-primed hardboard, and vinyl that may be stained, painted, dried or sawed. Experimental tests were based on the LIFT apparatus [19]. These tests consisted in exposing the siding materials to varying irradiance until time to piloted ignition was observed. Close agreement for ignition temperature, thermal diffusivity and thermal conductivity values were found comparing ignitability tests and empirical results derived from a finite element model solution. Although melting of vinyl siding was not observed at radiant heat loads of

70 kW/m^2, flaming ignition of the shrunk siding material occurred when exposed to 33 kW/m^2 of radiant heat. The thermo-physical properties presented were considered to direct inclusion into the Structure Ignition Assessment Model (SIAM) [20].

Quarles and Sindelar [21] evaluated fibre cement board, wood, plywood T1-11, and two types of vinyl siding under a radiant heat of 35 kW/m^2. Reported times to ignition (*TTI*) of wood and plywood were 4 and 16 minutes, respectively. Both types of vinyl were reported to melt within a minute of exposure without observing flaming ignition. The fibre cement board siding was tested on a re-entrant corner configuration where the sheathing materials were the siding was mounted, ignited with flaming ignition after 33 minutes of exposure to the radiant heat load. It was concluded that the vulnerability of the re-entrant corner is more dependent on flame contact exposure from burning debris and vegetation than purely radiant exposure.

Other analyses have focused on semi-quantitative inspections after prescribed burnings determining firebrand production, flame propagation, and vulnerabilities from ember exposures. Manzello, *et al.* [22], determined the vulnerabilities of vinyl and polypropylene siding when exposed to firebrand showers. It was observed that embers melted both types of siding, but only on the vinyl siding, holes developed through the material. Suzuki and Manzello [23], studied the firebrand size production and propagation generated by wall assemblies with and without cedar siding material. Their findings suggested that lighter and smaller firebrands were produced using cedar siding as compared to experiments constructed of only Oriented Strand Board (OSB) or wood studs. These results suggest siding treatments do indeed influence of the firebrand production process. More recently, Manzello, *et al.* [24] investigated the effect of a wall assembly constructed with vinyl

siding on the propagation of flames through the wall with adjacent mulch beds. It was observed that the vinyl siding did not influence the ignition of the mulch beds and that the use of a vinyl siding was an important parameter as to whether flames propagates to the back of the wall or not.

Furthermore, studies have analyzed the performance of supplementary materials such as intumescent coatings, wrapping materials, and wildfire chemicals that can be applied on the surface of the siding materials, particularly to combustible siding materials, to provide enhanced protection to buildings [25]. Zhou [26] analyzed the fire protection effectiveness of ten different fire-rated coatings (such as FX-100, FX-WF, and A-18), seven composite wraps (such as Firezat HD, Firezat LD, and S-Barrier), and one wildfire chemical (Thermo-Gel 200L). Results showed that wrappings performed better than the fire-rated coatings; some coatings tended to detach due to their exposure to fire, uncovering the sheathing materials. The use of fire-retardant chemicals, however, will not suffice if non-combustible building materials are required for a specific structure. According to the Appendix A, Section D-4.2.3 of the Alberta Building Code, "…the addition of a fire-retardant chemical is not sufficient to change a combustible product to a non-combustible product" [15]. Besides, these types of coatings or wrapping materials will represent an additional expense to the homeowners.

Siding materials that do not withstand radiant heat loads are still being considered as suitable options for the WUI. After the Fort McMurray wildfire, vinyl siding was recommended as an option to include in the reconstruction of the buildings [27]. Conversely, studies and agency reports [11, 21, 28] do not recommend vinyl siding, as it is likely to fail when it is exposed to high heat from fires.

During a fire, thermal radiation occurs prior to the arrival of a flame front. This radiant heat from the flames can raise the temperature of the exterior of a building to the point of ignition [29]; therefore, incident radiant heat flux loads have been used to evaluate the fire resistance of construction materials [25, 26, 30, 31]. Heat flux on surfaces provides a value that is easy to relate to the specific amount of energy to which an object will be exposed [32]. Heat fluxes around 20 kW/m^2 are sufficient to cause flashovers [33]. Silvani and Morandini [34], recommended irradiance levels of 18 to 50 kW/m^2 to be used in thermal degradation studies in order to provide reliable data relevant to wildfires. The National Institute of Standards and Technology (NIST) assessed the structure separation distance in multi-structure fires, where heat fluxes reported were to be between 20 and 70 kW/m^2, with a value of 50 kW/m^2 for much of the fire event [14]. Many design choices in the built environment are based upon knowledge of fire behavior and its effects on risk [8].

In this study, the goal was to provide quantitative information on the failure point of different commercially available siding materials by evaluating their performance when subjected to high and low radiant heat fluxes that are representative to both wildland fires and fires in the proximity of structures. Results from this study will help frame recommendations for choosing optimal siding materials for structures in the WUI.

2. OBJECTIVES

The main objective of this research project was to:

Evaluate the fire-resistant effectiveness of different commercially available siding materials when subjected to incident radiant heat loads by:

1. Evaluating the siding materials under
    a. A constant, high radiant heat load condition (HHC) of 50 kW/m^2;
    b. A constant, low radiant heat load condition (LHC) of 20 kW/m^2;

2. Determine the effect that radiant heat load has over the time to ignition;

3. Obtain ignition temperatures for the siding material prototypes; and

4. Develop an analytical model to predict the time to ignition based on transient temperature profiles.

3. THESIS ORGANIZATION

Chapter 1 presents an introduction to the thesis topic, including a definition of the Wildland Urban Interface (WUI) and the imminent risk to which they are exposed due to their proximity to forests. Here, a few recent examples of catastrophes in Canada that were related to wildfires are given as well as the aftermath of the damages. The principal causes of a fire in the WUI are presented and the most common practices and investigations that have been done to minimize the risk of a fire in these communities are explained.

Chapter 2 and Chapter 3 describe the objectives and the organization of this thesis, respectively.

Chapter 4 focuses on the experimental method. In this chapter the equipment, materials, test procedure, and failure criteria are described. A major focus of this chapter was centered on the methodology to test the heating source and to measure the heating conditions at which the siding material prototypes will be exposed.

In Chapter 5, the result from the burn tests are presented as well as the statistical analysis that was conducted. The time to ignition and the ignition temperatures of the different siding material prototypes are reported.

Chapter 6 presents the analytical model that was proposed to predict the time to ignition. A method to determine the heat losses is presented and used to obtain the transient temperature profiles of the siding materials.

4. EXPERIMENTAL METHOD

4.1 Materials

The siding materials that were used for testing were vinyl siding (Double 4.5 inch Dutchlap, Ply Gem Canada, Calgary, Alberta, Canada), cedar siding (Western red cedar, Windsor Plywood, Westlock, Alberta, Canada), engineered wood (fibre substrate, 76 Series Cedar Lap Siding, LP SmartSide, Louisiana-Pacific Corporation, Nashville, Tennessee, USA), and fibre cement board (HZ5 Hardie Plank lap siding, Hardie Board, James Hardie, Fontana, California, USA). OSB was used as the control material for the experiments. The dimensions of the composite wall (referred to as 'prototype' in this report) were 533 x 533 mm^2 (21 x 21 $inch^2$). The prototype was comprised of the siding material, a moisture barrier (Typar building wrap, Old Hickory, Tennessee, USA), and a 11 mm (0.4375 inch)-thick untreated OSB (APA Wood, Tacoma, Washington, USA).

Cedar and vinyl sidings are typical exterior siding materials in the WUI [18]. Stucco and aluminum/steel are considered to be fire-resistant by the FireSmart Hazard Assessment System; however, homes in Fort McMurray received a poor rating by this assessment due to the uncommon use of stucco, aluminium or fibre cement board [9]. Nonetheless, fibre cement board is being widely recommended and is becoming more popular for the WUI communities [17, 21, 35]. Testing engineered wood may provide useful information regarding its performance under a fire scenario since it has been stated that this material is less prone to breakage than fibre cement board [36]; also, no previous work was found to include this siding material in a set of siding materials to evaluate their response under radiant heat loads.

No insulation was considered for the construction of the prototypes. Insulation decreases the heat loss through the back of the prototype, causing prototypes to fail at faster rates. With both faster and potentially coincident failure, distinguishing between the performances of siding materials would be challenging.

4.2 Equipment

Figure 2 shows the experimental assembly. An electric-powered radiant heater (Omegalux QH-121260, Omega Engineering, Inc., Laval, QC, Canada) was used to generate radiant energy that was incident on the siding materials. A multi-channel data acquisition unit (34970A Data Acquisition/Data Logger Switch Unit, Keysight Technologies Inc., Santa Rosa, California, USA), and stainless steel braided J-Type 24 gauge thermocouples (Omega Engineering Inc., Laval, QC, Canada) were used to measure temperatures and collect data from:

- The exposed surface of the siding material (Figure 3(a), surface A).
- The interface surface; comprised by the internal surface of both the OSB and the siding material (Figure 3(a), surface B).
- The unexposed or backside surface of the OSB (Figure 3(a), surface C).

A metal skid was used to mount the prototype steel holder and the radiant heater panel. The steel holder was used to hold in place either the prototypes or a Schmidt-Boelter heat flux sensor (Model No.: 64-10T-10R (CaF2W)-20898, MEDTHERM Co., Huntsville, Alabama, USA) that was used to measure the heat fluxes.

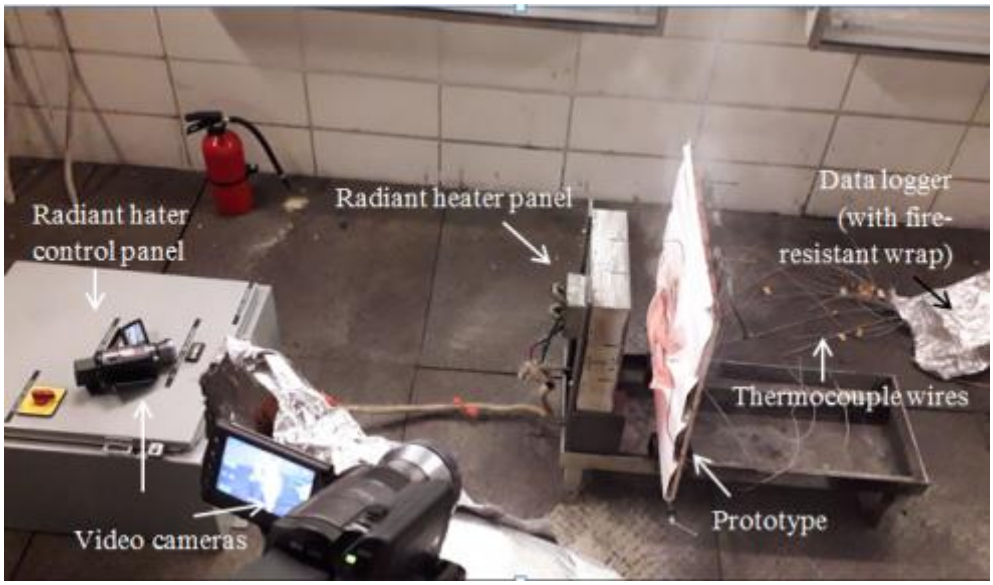

Figure 2 *Experiment assembly consisting of a radiant heater, skid and sample holders, control panel, prototype, set of video cameras, set of thermocouple wires, and data logger.*

4.3 Thermocouple arrangement

Five thermocouples were used in order to have one measuring point arranged along the vertical and horizontal centerlines. Figure 3(b), 3(c), and 3(d) show a schematic of the thermocouple location. A total of fifteen thermocouples were used for the siding material prototypes while only ten were required for the OSB (control material). In this report, thermocouples are represented with the letter 'T' and its corresponding number to identify the location of the thermocouple. For example, T1 is located on the center of the exposed surface while T11 is located on the center of the backside of the OSB. The sampling frequency was se to 0.3 Hertz, i.e., the data acquisition system was set to take one temperature measurement each three seconds.

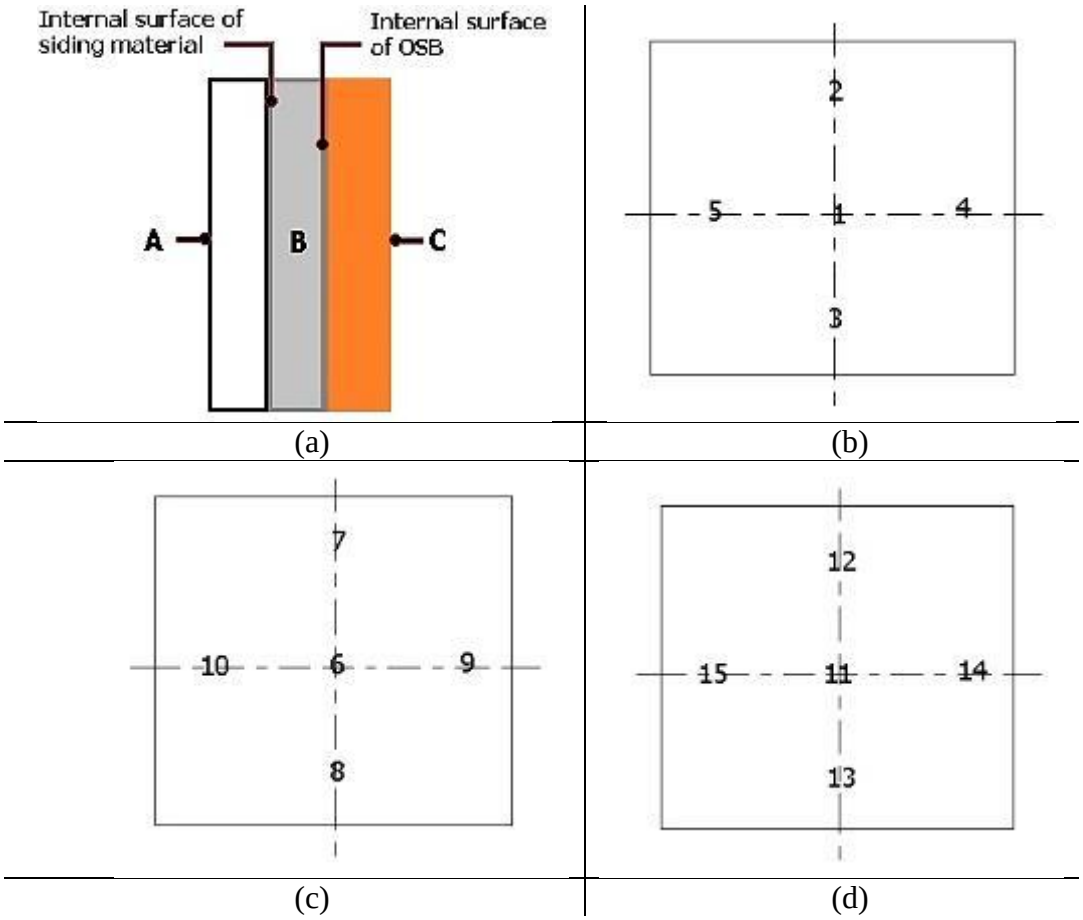

Figure 3 *Schematic of (a) the composite wall comprised of the siding material exposed surface (A), the siding material-OSB interface (B), and the unexposed or back surface of the OSB (C), (b) the thermocouple arrangement on the exposed surface, (c) the thermocouple arrangement on the interior surface of the OSB in the interface surface, and (d) the thermocouple arrangement on the unexposed or back surface.*

4.4 Burn tests

The burn tests for the present study were conducted at the Protective Clothing and Equipment Research Facility (PCERF) at the University of Alberta. In order to expose the prototypes to a constant incident heat flux condition, a 2.5 inches-thick insulation board (shutter) (M-board, Industrial Insulation Group, Augusta, GA, USA) was used to shield the prototypes from incident radiation during the period in which the heat flux from the radiant

heater panel was increasing to a steady state. Upon achieving steady state conditions of heat flux, the shutter was removed. This was considered as the starting point of the test (at $t = 0$).

Tests were terminated after 30 minutes or if a prototype failed; whichever occurred earlier. The failure criteria was defined as the time to ignition (*TTI*) of the prototype, where ignition could be due to flaming ignition of the siding material, or flaming or glowing ignition of the OSB behind the siding material. Use of the *TTI* of exclusively the siding materials as the absolute test termination criterion was not suitable for these tests since the siding materials that were evaluated were both combustible materials (such as OSB and cedar siding) and non-combustible materials (such as vinyl siding).

To gather quantitative evidence of the failure of the prototypes, the transient temperature profiles from the thermocouples were used to both determine the failure point and to analyze the temperature variation of the surfaces (thermal response) of the prototypes. To generate sufficient data for statistical consistency, a minimum of three burn tests of each type of prototype was performed ($n = 3$) for the heat flux condition.

4.5 Heat flux conditions

A high heat flux condition (HHC) of 50 kW/m^2 and a low heat flux condition (LHC) of 20 kW/m^2 were selected to test the siding materials. These conditions are representative of heat fluxes in both wildland fires and fires in the proximity of structures [17–21, 34].

Anderson [37] obtained different heat flux values by varying two parameters: the set-point temperature of a radiant heater (HST) and the distance between a heat flux sensor and a radiant heater panel (stand-off distance). For the present study, 114 mm (4.5-inches) stand-off distance was chosen so as to provide sufficient space to use the shutter between either the prototypes or the heat flux sensor and the radiant heater panel.

To estimate a maximum heat flux value that can be achieved with the radiant heater used for the present study, the radiant heater was allowed to reach its maximum temperature in open air conditions (no equipment or devices on its vicinity). An infrared camera (EXTECH VIR50 Dual laser video IR thermometer, Nashua, New Hampshire, USA), with a temperature range from -50 to 2000°C and an adjustable emissivity range from 0.1 to 1.0, was used to monitor the heater screen temperature. In addition, an emissivity for a perfect black body (ε = 1) was assumed for the heater screen. These values, the measured temperature and the assumed emissivity, were used as input into the expression for the radiation emitted by a blackbody [38]:

$$E_b = \sigma T^4 . \qquad (1)$$

According to the manufacturer's specifications [39], the IR camera was located in front of the radiant heater at a distance of 2500 mm (98 inches), (Figure 4). Figure 5(a) shows the radiant heater surface temperature that was estimated for the blackbody assumption. With

this camera, the following conditions were also measured: IR maximum temperature (IR), IR differential temperature (DIF), average temperature (AVG), ambient temperature (AT), and relative humidity (RH). The blackbody radiation value was estimated to be 56.6 kW/m^2. Consequently, no heat flux values measured should be greater than this estimated value.

Values of $\varepsilon = 0.92$ and $\varepsilon = 0.95$, which are typical emissivity values for glass [39], were used to determine the real maximum screen temperature of the radiant heater. The resulting temperatures measured for both emissivity values where around 746 ± 1.4 °C (Figure 5(b) and 5(c)). This temperature value was the maximum temperature at which the siding materials prototypes were exposed.

These screen temperature measurements were conducted because it was found that the probe, which was used to sense the screen temperature and to provide feedback to the temperature control system, was highly affected by a re-irradiation phenomenon.

The re-irradiation was generated from both the heater radiation and the radiation emitted from the shutter. It was observed that the probe measured temperatures of 850°C when the shutter was in place; however, once the shutter was removed, the heater screen temperature decreased and it maintained a relatively constant temperature of 746°C, therefore, 850°C was a ‘false measurement’. Knowing that this re-irradiation was affecting the probe was important to avoid the use of inaccurate heater set-point temperatures to establish the heat flux conditions.

Figure 6 shows four OSB trial tests where different thermal responses were obtained using ‘false heater set-point temperatures’. Figure 6(a) and 6(b) were at ‘false temperatures’ of 750°C and 800°C; the corresponding real screen temperatures were approximately 694°C and 738°C, respectively. Figure 6(c) and 6(d) were at a ‘false temperature’ of 850°C; the real screen temperature was approximately 750°C. An exercise to confirm if flaming ignition of the OSB (Figure 6(c) and 6(d)) was obtained within the capable range of temperatures of the radiant heater panel, the transient temperature profile of the heater screen was plotted indicating the time when flaming ignition of the OSB was observed (Figure 7).

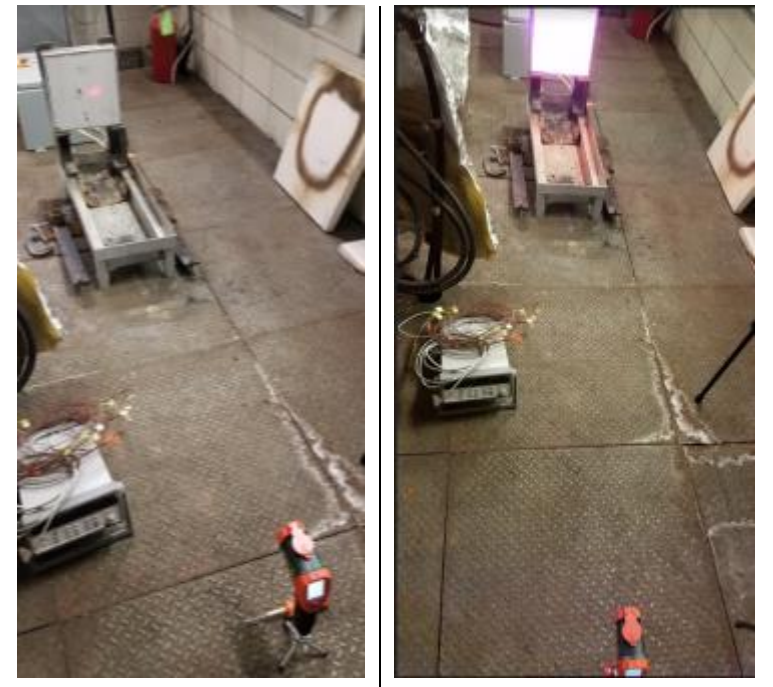

(a) (b)

Figure 4 *Assembly in open air conditions of the IR camera and radiant panel when (a) the radiant heater was off and (b) the radiant heater was emitting energy.*

(a) (b) (c)

Figure 5 *Heater screen temperature measured with (a) ε = 1, (b) ε = 0.92, and (c) ε = 0.95. The letter "A" in the display represented the emissivity, ε.*

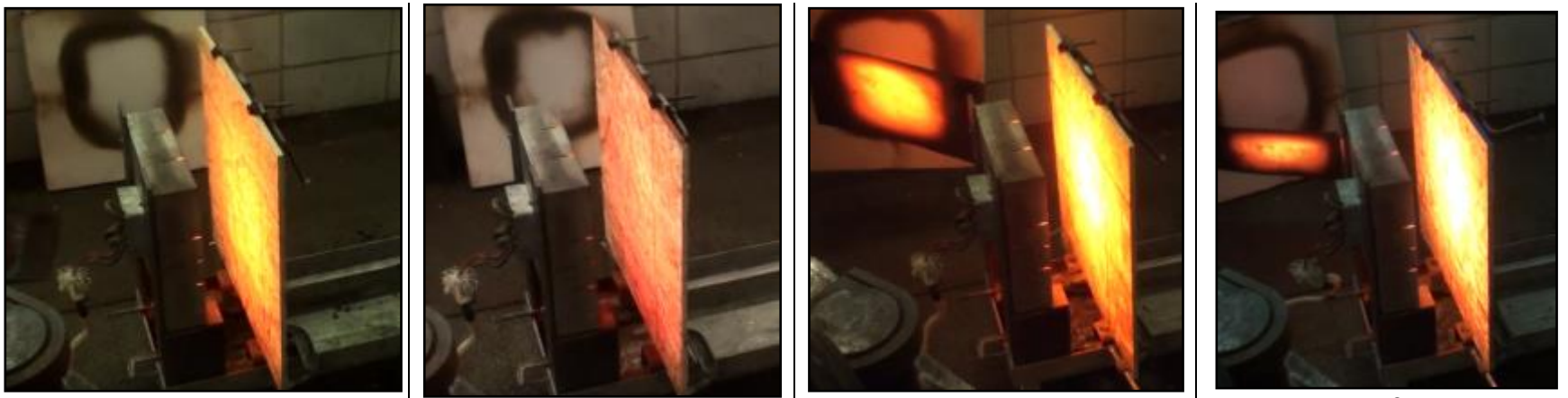

t = 0 s	t = 0 s	t = 0 s	t = 0 s
t = 475 s	t = 384 s	t = 15 s	t = 10 s
(a)	(b)	(c)	(d)

Figure 6 *OSB trial tests exposed to radiation emitted from the radiant heater panel with 'false' heater set-point temperatures at (a) 750°C (real temperature was 694°C), (b) 800°C (real temperature was 738°C), and (c) and (d) at 850°C (real temperature was 750°C).*

Figure 7 show the transient temperature profile of the heater screen as the temperature stabilized after removing the shutter. Figure 8 show the control panel displaying the temperatures measured by the probe and the corresponding OSB behaviour over time. Flaming ignition of the OSB was observed at a heater temperature of 748.3°C. This temperature showed close agreement with the maximum temperature that was measured for the radiant heater panel, which was 746 ± 1.4 °C (Figure 5).

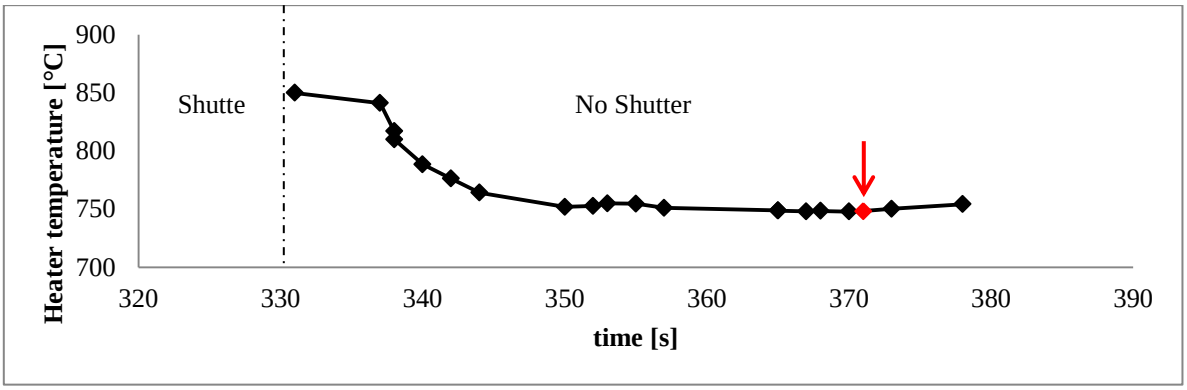

Figure 7 *Screen transient temperature profile. The rhombus pointed with the arrow indicates the TTI of the OSB.*

Therefore, based on calibration done using the Schmidt-Boelter heat flux sensor, the radiant panel was able to output a constant heat flux of 57 kW/m^2 and 20.3 kW/m^2. At a stand-off distance of 114 mm (4.5-inches) and radiant heater panel surface temperature of 746°C (1375°F), an incident heat flux of 56.99 ± 0.36 kW/m^2 (n = 3) was obtained, which is slightly higher than the estimated blackbody radiation. Figure 9 shows the high heat flux condition (HHC) profile as a function of time. At the same stand-off distance and a heater panel surface temperature of 520°C (968°F), a value of 20.3 ± 0.31 kW/m^2 (n = 3) was measured. Figure 10 shows the low heat flux condition (LHC) profile as a function of time.

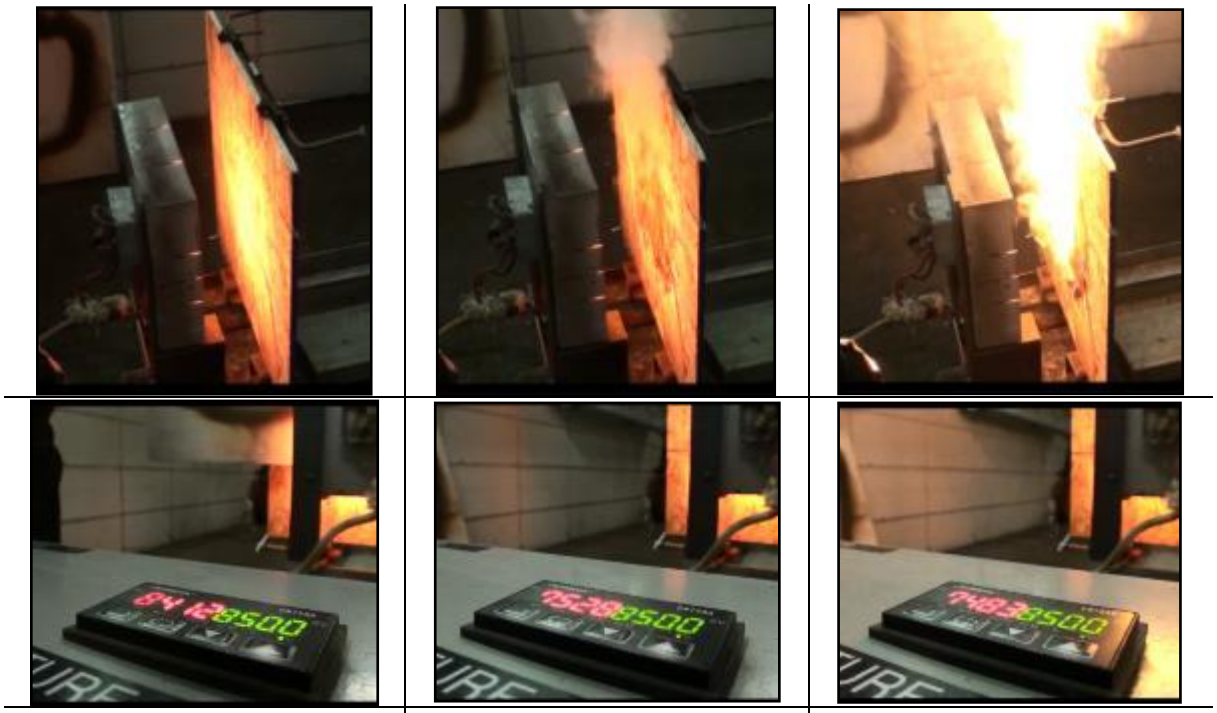

(a) $t = 0$ s (b) $t = 15$ s (c) $t = 34$ s

Figure 8 *Heater temperature decreased from (a) the removal of the shutter to (c) ignition of the OSB. Bottom images correspond to the control panel displaying the temperatures measured by the probe.*

In Figure 9 and 10, a rapid increase in the heat flux value resulted from a direct exposure of the heat flux sensor to the heat load when the shutter was removed. These rapid increases were observed at $t \approx 360$ s for the HHC and at $t \approx 130$ s for the LHC. After these increases, the heat flux measurement stabilized, thereby, steady state was considered. The oscillating profiles observed during steady state in Figure 9 and Figure **10** were caused by temperature fluctuations that consequently were reflected in the heat flux measurement. Fluctuations are more noticeable in the LHC since these heat flux values are relatively low as compared to the heat flux of the HHC.

The data and figures that are presented in Figure 7, Figure **9**, and Figure **10** were used to assess the heat flux and temperature measurement systems and calibrate them as needed.

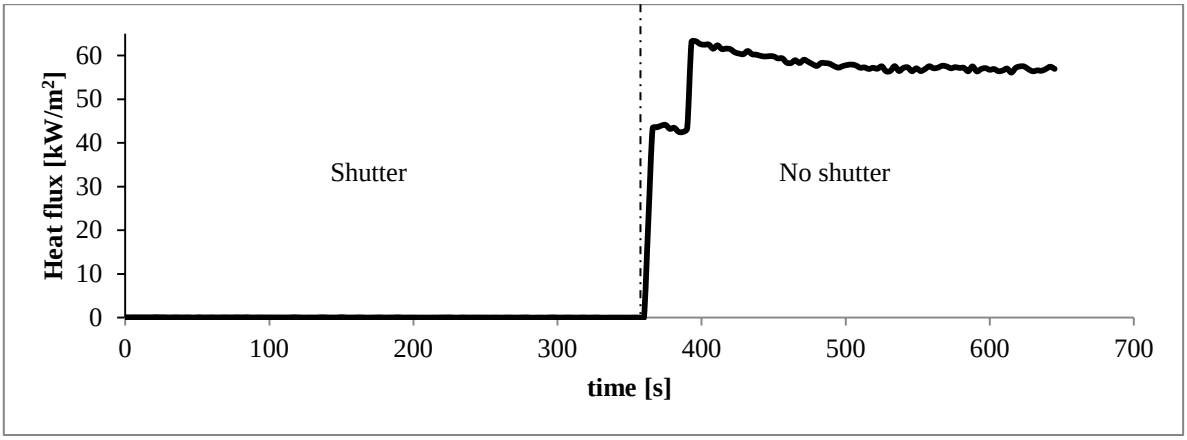

Figure 9 *High heat flux profile as a function of time.*

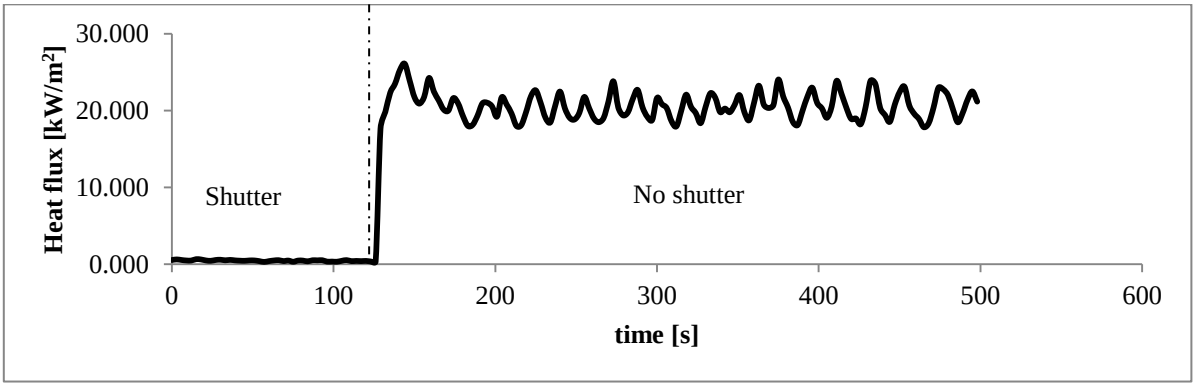

Figure 10 *Low heat flux profile as a function of time.*

5. EXPERIMENTAL RESULTS AND DISCUSSION ANALYSIS

5.1 Experimental results for the Time to Ignition (TTI)

5.1.1 Oriented strand board (OSB)

Oriented strand board (OSB) was used as the control material. No siding material or building paper was considered for these tests. Only ten thermocouples were used since no siding material was required.

Under the HHC, flaming ignition of the OSB occurred at $t = 433 \pm 66.70$ s of exposure to the incident radiant heat flux. An indication of the ignition of the OSB can be observed in Figure 11(a) and Figure **11**(b) which corresponds to the burn test No. 3, which showed a sudden increase in both the exposed and back surface transient temperatures at this time.

Figure 11(c) and Figure **11**(d) show the exposed and back surface transient temperature profiles resulting from the burn test No. 3 of the OSB under the LHC. These tests were terminated when glowing ignition was observed on the exposed surface, which occurred after $t = 544 \pm 33.45$ s of exposure to the incident radiant heat flux. Under this condition, no flaming ignition was expected or observed, which was in accordance with results obtained from [30]. Figure 12 shows a comparison between the HHC and LHC burn tests of the OSB.

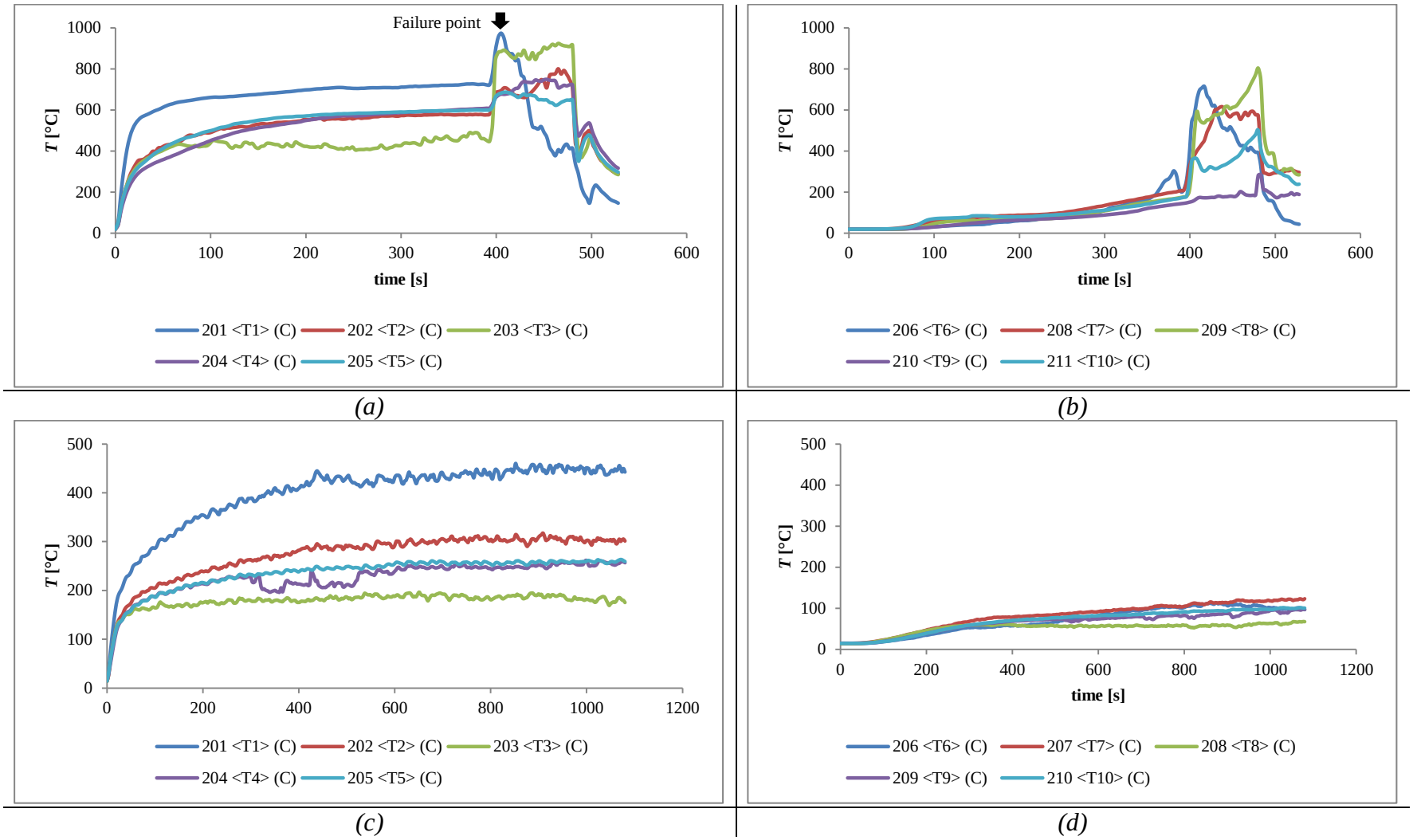

Figure 11 *Transient temperature profiles of the OSB for (a) the exposed surface and (b) the back surface, both under the HHC, and (c) the exposed surface and (d) the back surface, both under the LHC.*

(a) *(b)*

Figure 12 *Comparison of the burn tests of the OSB between (a) the HHC and (b) the LHC.*

5.1.2 Vinyl siding (VS)

Observations from the video footage showed that the vinyl siding (VS) melted after approximately 5-10 seconds of exposure under the HHC. Figure 13 shows the transient surface temperature profiles of the vinyl prototype burn test No. 3 under the HHC, Figure **13**(a) and Figure **13**(b); and for the burn test No. 2 under the LHC, Figure 13(c) and Figure **13**(d). Figure 13(a) shows the exposed surface transient temperature profiles. Since dislodgement of the thermocouples on the exposed surface occurred in all the burn tests for this siding material (Figure 14), the exposed surface temperatures were not useful to describe the thermal response of the siding material. Figure 13(b), shows the interface surface transient temperature profiles where a sudden increase in the temperatures occurred after $t = 69 \pm 10.39$ s of exposure to the incident radiant heat flux, at this time, the ignition event occurred. Figure 15 show the ignition of the VS prototype.

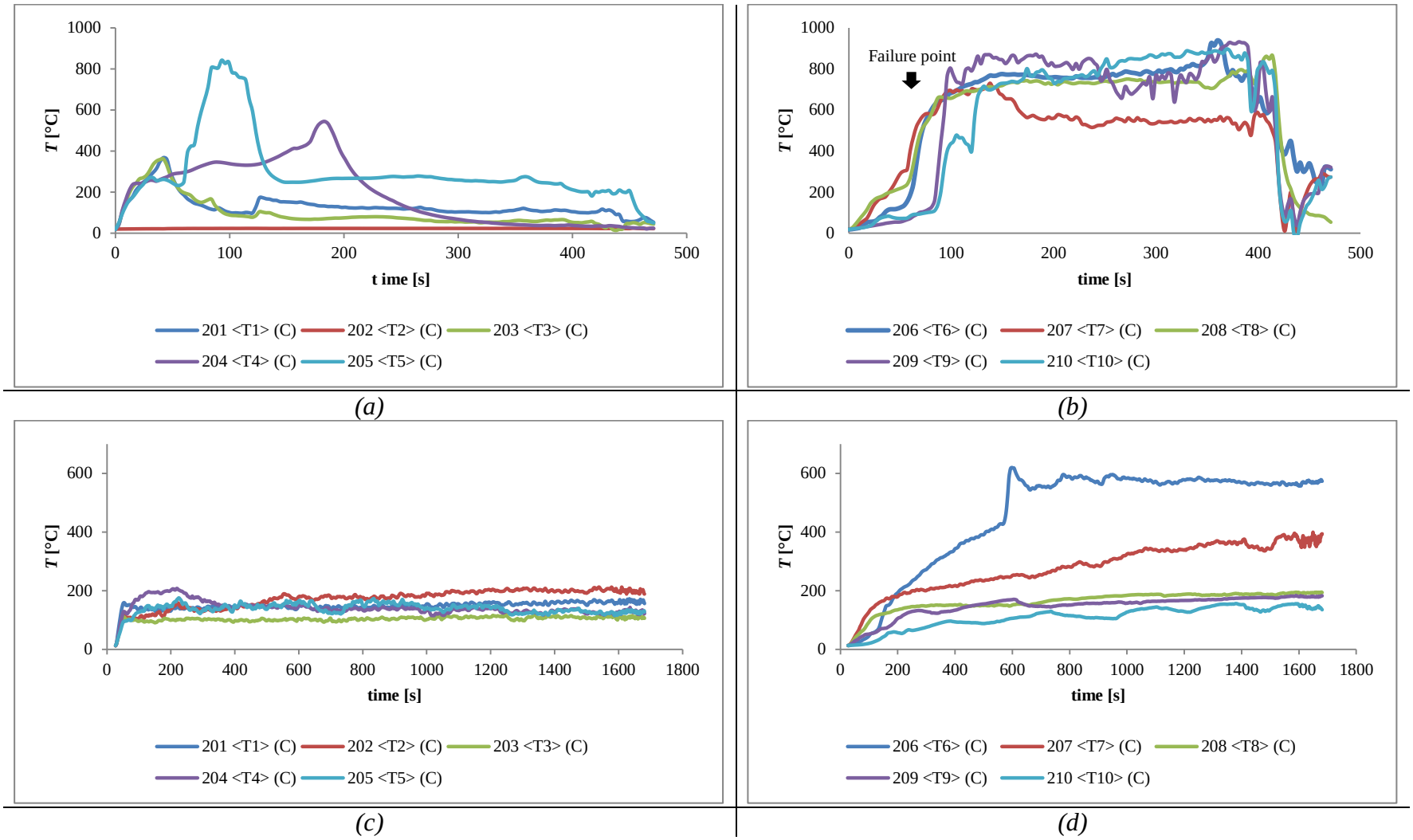

Figure 13 *Transient temperature profiles of the VS for (a) the exposed surface and (b) the interface surface, both under the HHC, and (c) the exposed surface and (d) the interface surface, both under the LHC.*

(a) *(b)*

Figure 14 *Thermocouples (a) dislodged and (b) trapped into the deformed vinyl siding.*

(a) *(b)*

Figure 15 *Images of (a) deformed VS prior to ignition and (b) VS prototype igniting under the HHC.*

The melting of the vinyl siding took slightly longer under LHC in comparison to HHC, based on video evidence from the footage captured. It was also confirmed that no flaming ignition occurred under this heat load condition for either of the VS or the OSB that was part of this prototype. After an exposure time of $t = 1162 \pm 303.42$ s, glowing ignition was visible on the OSB surface at the interface surface. Figure 13(c) and Figure **13**(d) show the temperature variation of the exposed and interface surfaces of the VS prototype under the

LHC. Figure 16 shows a comparison between the HHC and LHC burn tests of the VS prototype.

(a) *(b)*

Figure 16 *Comparison of the burn tests of the VS prototype under (a) the HHC and (b) the LHC. The red circle indicates the region where glowing ignition was observed.*

5.1.3 Engineered wood (EW)

Flaming ignition was observed under both exposure conditions. Figure 17 shows the transient temperature profiles of the engineered wood (EW) burn test No. 3 under the HHC and the burn test No. 1 under the LHC. Figure 17(a) and Figure **17**(b) show the resulting temperature profiles for the exposed and the interface surfaces under the HHC. Correspondingly, Figure 17(c) and Figure **17**(d) show the temperature profiles for the exposed and the interface surfaces under the LHC. The occurrence of flaming ignition was visible by way of a nearly singular, rapid increase in the temperature of the exposed surface; hence, under the HHC the *TTI* was 424 ± 3.46 s. Figure 18 shows the ignition of the EW prototype under the HHC.

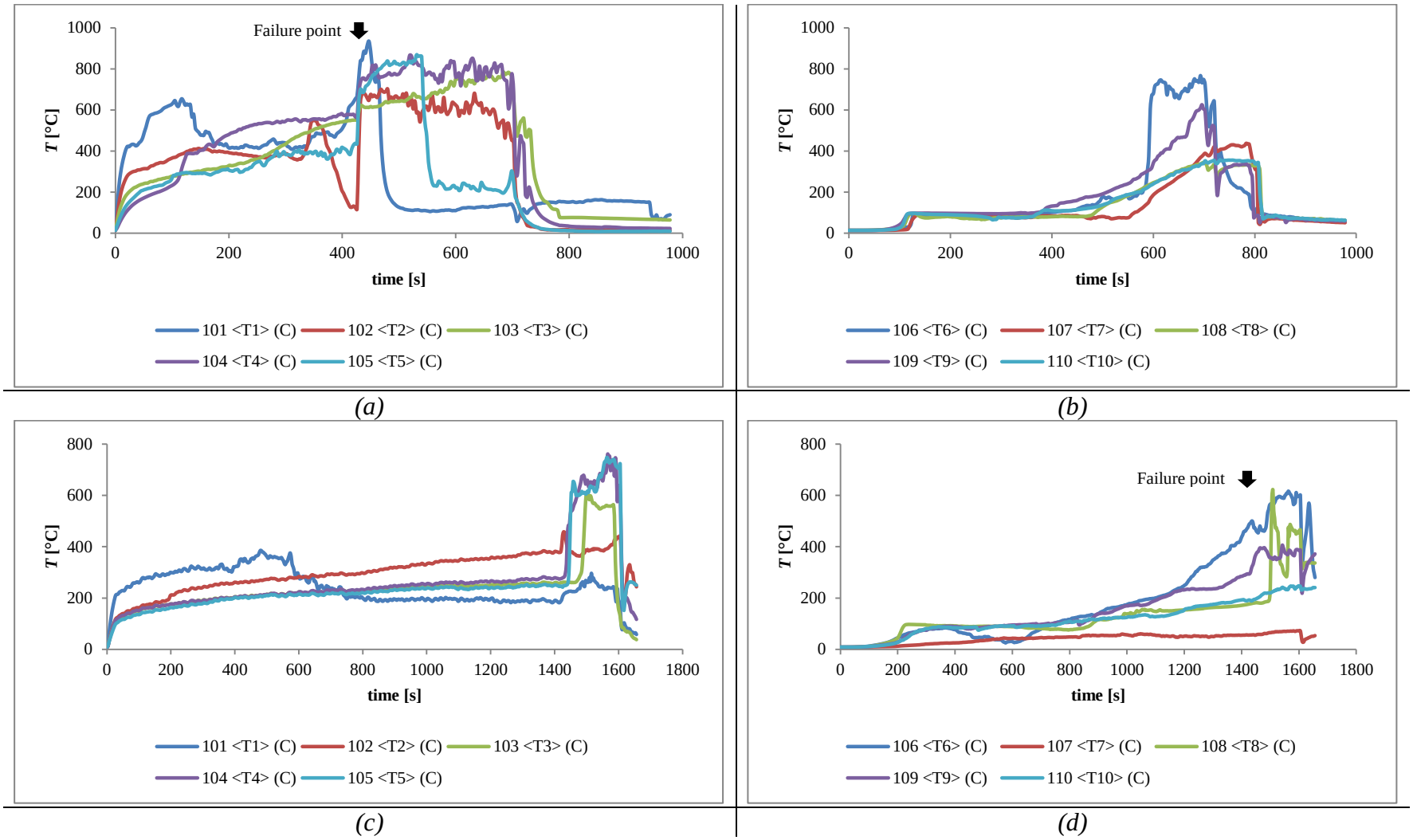

Figure 17 *Transient temperature profiles of the EW for (a) the exposed surface and (b) the interface surface, both under the HHC, and (c) the exposed surface and (d) the interface surface, both under the LHC.*

(a) *(b)*

Figure 18 *Ignition process of the EW prototype under the HHC at (a) the TTI and (b) fully developed flaming ignition.*

Under the LHC, it was observed that flaming ignition process was initiated on the internal surface of the OSB at the interface surface rather than at the exposed surface of the prototype. This was confirmed by the rapid increase in the transient temperatures of the exposed and interface surfaces at the time when ignition occurred, as shown in Figure 17(c) and Figure **17**(d); therefore, under the LHC, the *TTI* was 1437 ± 71.38 s. It can be assumed that the continuous siding material loss that occurred as a result of the slower thermal degradation process eventually left the OSB directly exposed to the incident heat load. Figure 19 shows a comparison between the HHC and LHC ignition processes. In Figure 19(a), it can be observed that the flammable volatile gases that were generated from the EW ignited, whereas in Figure **19** (b), flames were generated on the internal surface of the OSB at the interface of the prototype.

(a) *(b)*

Figure 19 *Comparison of the ignition process of the EW prototype under (a) the HHC and (b) the LHC.*

5.1.4 Fibre cement board (FCB)

Under both the HHC and the LHC, fibre cement board (FCB) siding did not ignite. However, under the HHC, flaming ignition occurred on the internal surface of the OSB at the interface. Under the HHC, the *TTI* was 1197 ± 197.45 s. Figure 20(a) and Figure **20**(b) show the exposed and interface transient surface temperatures profiles of the FCB burn test No. 2 under the HHC, where a rapid increase in the interface surface temperature was indicative of the ignition event.

Under the LHC, tests were terminated at t = 1800 s. Figure 20(c) and Figure **20**(d) show the exposed and interface transient surface temperatures profiles of the FCB burn test No. 3 under this exposure condition. The same approximate linear behaviour was observed on the transient temperature profiles as compared to such from the HHC; although, lower temperatures and no rapid increases occurred.

Figure 21(a) shows the flaming ignition of the FCB prototype; whereas Figure 21(b) shows that no ignition ensued on the FCB surface. Figure 21(c) shows the little damage observed on the internal surface of the OSB at the interface surface after the termination of the tests.

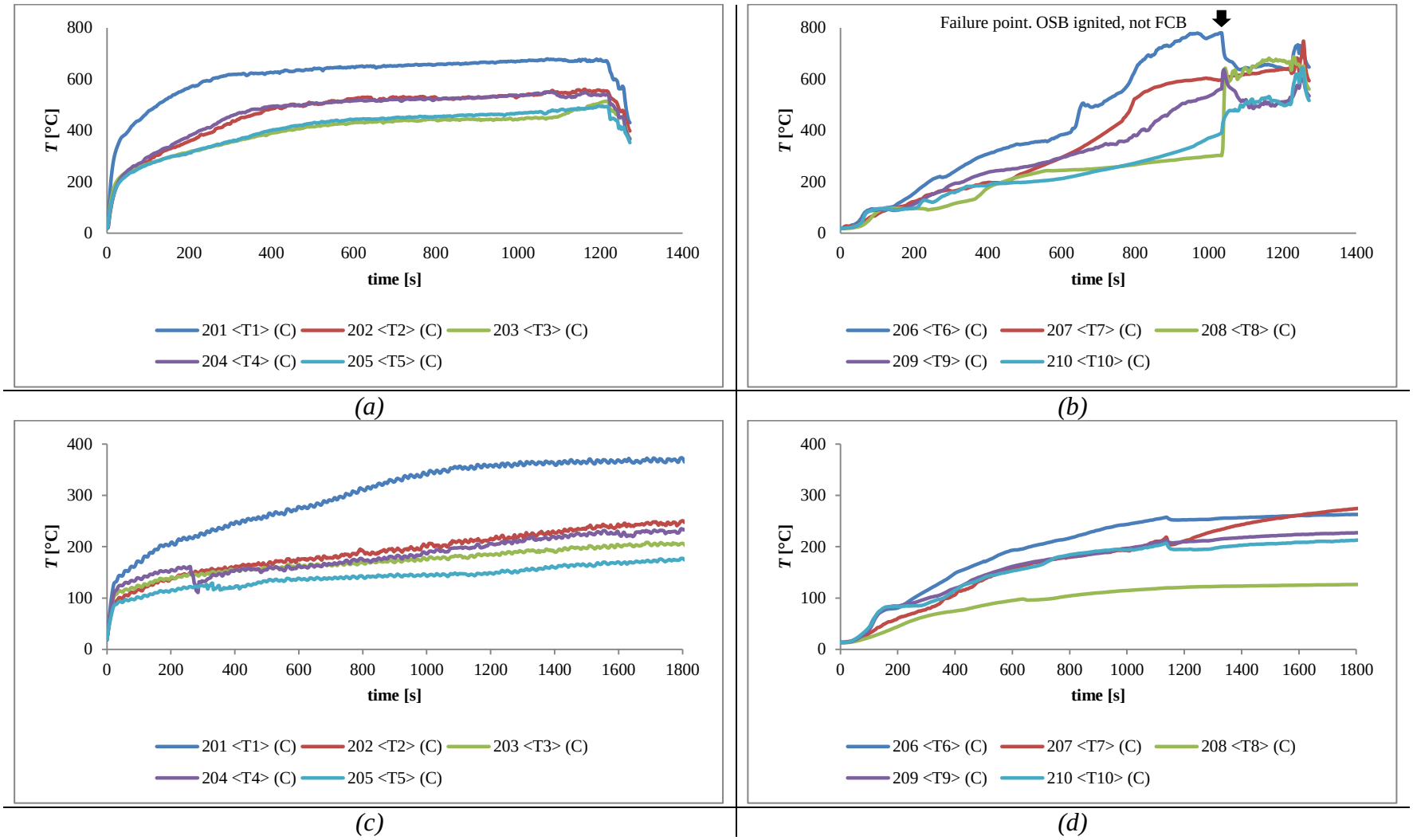

Figure 20 *Transient temperature profiles of the FCB for (a) the exposed surface and (b) the interface surface, both under the HHC, and (c) the exposed surface and (d) the interface surface, both under the LHC.*

(a) *(b)* *(c)*

Figure 21 *Comparison of the ignition process of the FCB prototype under (a) the HHC and (b) the LHC where (c) little damage on the interface surface was observed.*

5.1.5 Cedar siding (CS)

For the cedar siding (CS) material, flaming ignition occurred under both the HHC and the LHC. Under the HHC and the LHC, the *TTI* was $t = 19 \pm 1.73$ s and 666 ± 374.17 s, respectively. For both conditions, flaming ignition occurred at the exposed surface. Only for the burn test No. 3 under LHC, the ignitions process began on the internal surface of the OSB at the interface.

Figure 22(a) and Figure **22**(b) show the transient surface temperature profiles of the cedar siding (CS) prototype burn test No. 1 under the HHC, and Figure 22(c) and Figure **22**(d); show the cedar siding burn test No. 2 under the LHC.

Figure 23 shows a comparison of the cedar siding prototype burn tests between the ignition process under the HHC and LHC. When the samples were exposed to the HHC, the onset of ignition was more intense with visibly larger flame lengths. The larger flame lengths were likely due to a higher generation of flammable gas volatiles under the HHC.

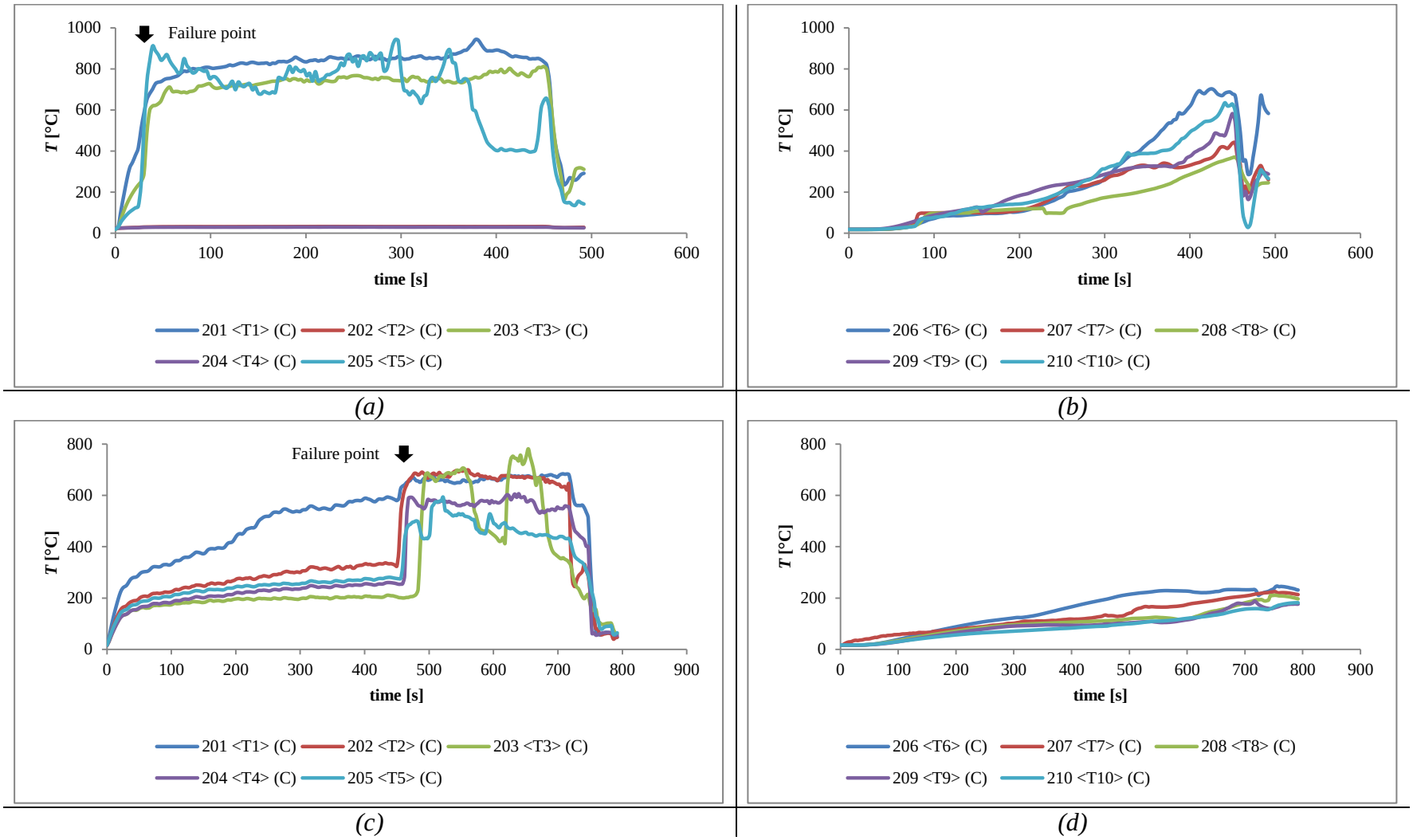

Figure 22 *Transient temperature profiles of the CS for (a) the exposed surface and (b) the interface surface, both under the HHC, and (c) the exposed surface and (d) the interface surface, both under the LHC.*

(a) *(b)*

Figure 23 *Comparison of the ignition process of the CS prototype under (a) the HHC and (b) the LHC.*

5.1.6 Comparison among TTIs of siding materials

The time to ignition (*TTI*) of the different prototypes was compared using statistical software – R Studio. A variance analysis (ANOVA) with a confidence interval of 95% (or P-value, $p < 0.05$) was performed to test the differences between the siding materials and their respective *TTIs*. Mean separation was done using Least Square Differences (LSD) test with a confidence interval of 95%. The results from this analysis showed that some siding materials were significantly different, i.e., there was a measurable difference between the *TTI* of the siding materials, where the probability of obtaining these results by chance was 5%.

Figure 24 shows the average *TTI* of different prototypes under HHC. The tests showed that cedar and vinyl prototypes failed the fastest while the fibre cement board took the longest time to fail. Statistical analysis showed that the difference in *TTI* was not significant

between cedar and vinyl as a pair, owing to their similar *TTIs* and standard deviations. Likewise, statistical differences in *TTI* for engineered wood and bare OSB were also not found. Statistical differences in *TTI* were found for fiber cement board compared to all other products despite its high standard deviation. These results suggest that fibre cement board offers the most resistance to ignition under high radiant heat loads while vinyl and cedar the least resistance under high radiant heat loads.

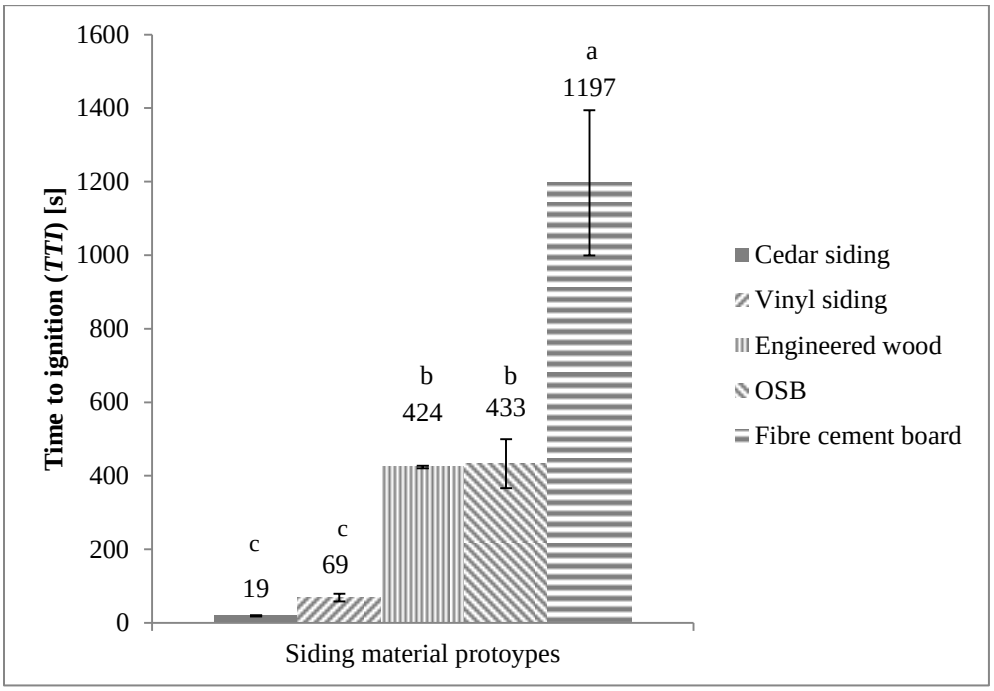

Figure 24 *Time to Ignition of the siding material prototypes under the HHC. Treatments with the same letter (a, b, c) are not significantly different according to the LSD test ($p < 0.05$). Vertical lines represent the standard deviation.*

Figure 25 shows the average *TTIs* of different prototypes under LHC. No *TTI* was shown for fire cement board since the prototype did not fail in the burn tests. Statistical analysis showed that cedar siding and bare OSB did not have significant differences in *TTI*, suggesting that the presence of cedar siding offers no real advantage to protect the OSB in its prototype from radiant heat.

The vinyl siding prototype took more than twice the time to fail when compared to the bare OSB. The engineered wood prototype took the longer time to fail; however, its resistance was not significantly different to the vinyl siding prototype. The large standard deviations of the cedar and the vinyl siding prototype can be attributed to the complex nature of the wood composition that is found in the cedar and to the resins and nature, composition, and orientation of the strands in the OSB. In a study where wooden materials were tested under radiant heat fluxes of 15 to 32 kW/m^2, large standard deviations where also obtained for the *TTI* under heat fluxes lower than 20 kW/m^2 [40].

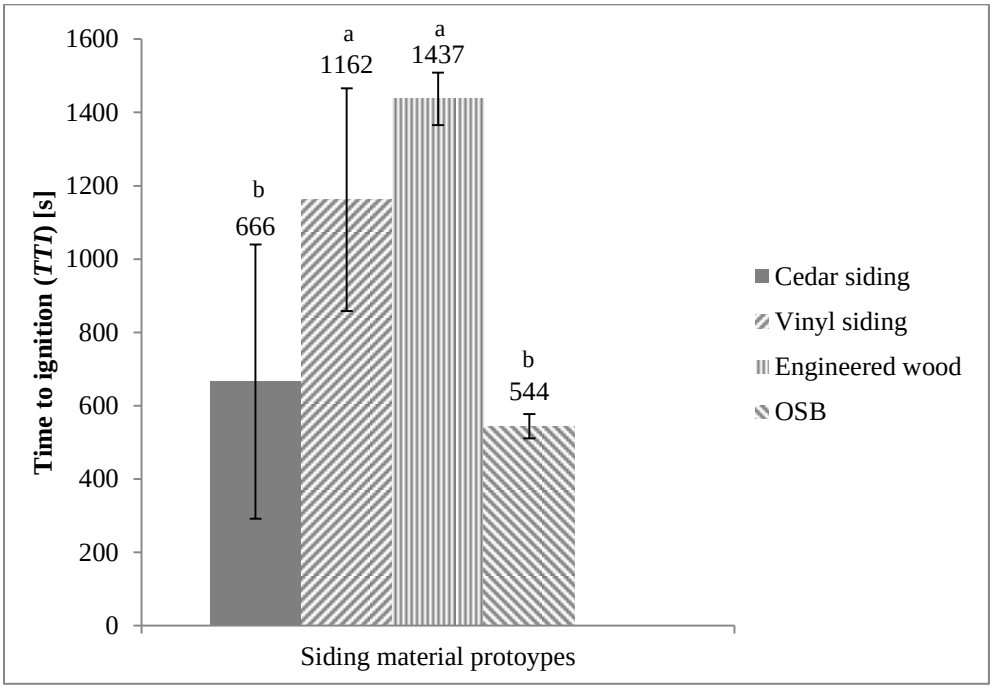

Figure 25 *Time to Ignition of the siding material prototypes under the LHC. Treatments with the same letter (a, b, c) are not significantly different according to the LSD test ($p < 0.05$). Vertical lines represent the standard deviation.*

5.2 Experimental results for the ignition temperatures (T_{ig})

The transient temperature profiles from the thermocouples were used to gather quantitative evidence of the failure of the prototypes, namely the *TTI*. At the *TTI*, the fuel gases ignited when both a specific concentration and temperature, autoignition temperature, were reached (Figure 26). Autoignition depends on the temperature of the vaporized fuel leaving a hot surface; hence, the surface temperature corresponds to the autoignition temperature of a vapour mixture [41], i.e., autoignition temperature of the fuel gases is caused by the surface temperature of the siding materials, the ignition temperature (T_{ig}).

Autoignition occurs in the absence of a pilot. When a pilot is used, the fire process is known as piloted ignition. According to Tran and Cohen [42], "Piloted ignition is defined in ASTM 176 as the initiation of combustion as a result of contact of a material or its vapours with an external high energy source such as a flame, spark, etc.". As shown in Figure 26, piloted ignition occurs at the Lower Flammability Limit (LFL) and at lower temperatures than autoignition. Once a flame results in a small region, the process become much like piloted ignition, as a premixed flame propagates through the remaining flammable mixture [41]. For this reason, from the temperature profiles resulting from the burn tests conducted in this work (Section 5.1), the maximum temperatures exhibited by the siding materials before the sudden increase in temperature that described the ignition event, were defined as the ignition temperatures as these values were likely to onset the autoignition process.

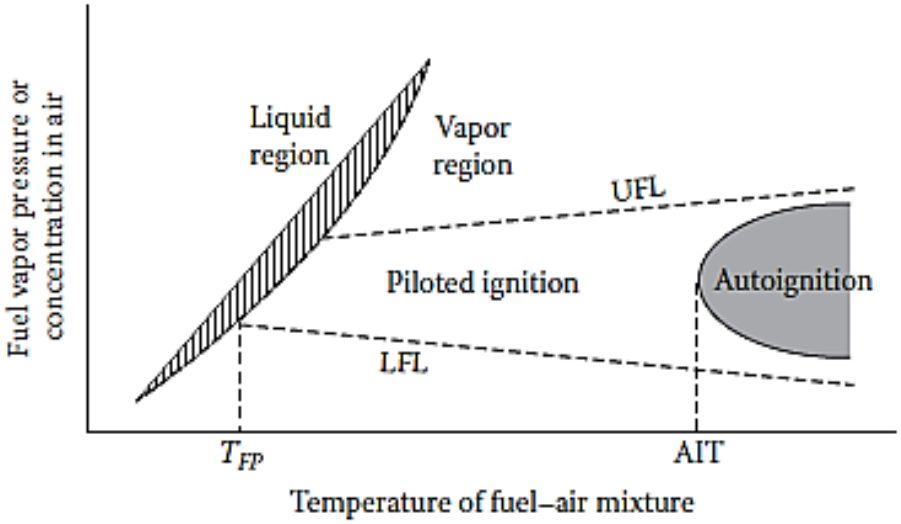

Figure 26 Conditions needed for ignition, where T_{FP} = Flash point temperature, LFL = Lower Flammability Limit, UFL = Upper Flammability Limit, AIT = Autoignition temperature [41].

Table 3 and Table **4** show summaries of the temperatures measured from the burn tests of the siding material prototypes. Temperatures were defined as maximum material temperatures (T_{max}) when no flaming ignition occurred. In Table 3, only the exposed surface of the fibre cement board described a T_{max} since the siding material did not ignite; the rest of the materials described T_{ig} on both the exposed and the interface surfaces. In Table 4, fibre cement board, vinyl siding, and OSB described T_{max} since only glowing ignition was observed.

Table 3 *Surface temperatures under the HHC.*

Materials	***Exposed surface***	***Interface surface***
Fibre cement board	633.95 ± 79.47°C *a*	742.25 ± 20.56°C *a*
Vinyl siding	N/A	448.04 ± 161.92°C *b*
Cedar siding	441.45 ± 55.67°C *b*	31.35 ± 23.11°C *d*
Engineered wood	628.14 ± 82.47°C *a*	244.87 ± 88.97°C *c*
OSB	749.03 ± 27.48°C *a*	277.98 ± 77.91°C (unexposed surface)

N/A: Not applicable. Treatments with the same letter (*a*, *b*, *c*) are not significantly different according to LSD test ($p < 0.05$).

Table 4 *Surface temperatures under the LHC.*

Materials	***Exposed surface***	***Interface surface***
Fibre cement board	350.53 ± 21.95°C *a*	274.17 ± 24.2°C *b*
Vinyl siding	N/A	503.99 ± 113.3°C *a*
Cedar siding	340.01 ± 38.77°C *a*	277.01 ± 167.54°C *b*
Engineered wood	366.82 ± 59.78°C *a*	474.38 ± 99.26°C *a*
OSB	449.01 ± 33.08°C *a*	100.97 ± 9.58°C (unexposed surface)

N/A: Not applicable. Treatments with the same letter (*a*, *b*, *c*) are not significantly different according to LSD test ($p < 0.05$).

Biswas, *et al*. [17] tested fibre cement board (FCB), cedar siding (CS), and vinyl siding (VS) material prototypes under different exposure conditions to simulate likely scenarios in the Wildland Urban Interface (WUI). Such conditions were (1) short-duration (60 s), high intensity radiant heating between 40 and 50 kW/m^2, (2) short-duration, direct flame contact (100 kW propane flame), and (3) long-exposure (900 s), coupled radiant

heating at 25 kW/m^2 and direct flame contact. That research evaluated the response of a 1.2 x 1.2 m^2 FCB under conditions (2) and (3). The measured temperatures reported for the short-duration, direct flame contact (condition (2)), rose to about 300°C. Although the experimental method is not comparable with the present study, there is agreement with the thermal response of the FCB under the LHC (Table 4). Surface temperatures for the coupled condition were not reported to compare them with the HHC results for the FCB of this study.

In the same study [17], for the VS sample under a radiant heat load of 40 kW/m^2, a sharp increase in temperature was observed at the "interior" surface when the siding failed at 230 to 310°C. In the present study, the ignition temperature observed at the interface surface was 448°C ± 161.92°C (Table 3), where the additional radiant energy (10 kW/m^2 higher than the condition used by Biswas, et al. [17]) impinging on the VS, heated the material at a faster rate resulting in higher temperature measurements. The ignition temperatures of solids depend, among other factors, on the decomposed fuel, its components, and the way the solid is heated [41]. Further investigation could be conducted to determine the OSB and VS gas volatiles that were derived from the exposure of the materials to radiant loads under stoichiometric conditions for comparison with measured composition of the flammable gas volatiles.

From a 40 kW/m^2 radiant heating test, cedar siding ignition temperatures were approximately 350°C [17]. In the present study, under the HHC and LHC, the temperatures at ignition of the CS were 441°C and 340°C, respectively. Although there is close agreement with the ignition temperature obtained under the LHC, there is a larger

difference between the temperatures obtained under the HHC and the 40 kW/m^2 test. Again, the different heating conditions yielded different thermal responses.

5.2.1 Comparison among ignition temperatures of siding materials

In Table 3, a large difference was observed between the exposed and the interface surface temperatures of the cedar siding. This temperature difference was due to the thermal inertia of the cedar siding. Thermal inertia is defined as the product of material thermal conductivity, k, density, ρ, and specific heat capacity, c ($k\rho c$). The lower the thermal inertia of the material, the faster the surface temperature will rise [33, 41, 43]. Table 5 shows the thermal inertia of the siding materials analyzed in the present study. It can be observed that the thermal inertia of the cedar siding corresponds to the lowest value for these siding materials.

Table 5 *Thermal inertia of the siding materials analyzed*

Materials	***Thickness* [m]**	***c* [J/kg·K]**	***k* [W/m·K]**	***ρ* [kg/m^3]**	***Thermal inertia* [J^2/m^2·K^4·s]**
Fibre cement board [44]	0.011	840	0.245	1380	2.840 x 10^5
Engineered wood [38]	0.011	1300	0.14	800	1.456 x 10^5
Vinyl siding [38]	0.001	840	0.1	1470	1.235 x 10^5
OSB [44]	0.011	1880	0.092	650	1.124 x 10^5
Cedar siding [44]	0.017	1880	0.085	336	5.369 x 10^4

Under the HHC (Table 1), cedar siding had both the lowest exposed and interface surface temperatures. Results from Table 3 and Table 5, suggest that the use of cedar siding is more unfavourable as compared to the use of bare OSB. From the surface temperatures of the fibre cement board (FCB) prototype, it was observed that the interface surface temperature

was in accordance with such from the exposed surface of the bare OSB at the onset of the ignition event. Comparing the surface temperatures from the FCB and the engineered wood (EW) it can be noted that the exposed surface temperatures were similar; nevertheless, the FCB prototype ignited after 1200 seconds whereas the EW prototype ignited approximately three times faster. This results suggested that FCB siding shielded and resisted the heat more effectively than the EW siding. Regarding the vinyl siding prototype, an important decrease in the ignition temperature of the internal surface of the OSB at the interface was observed when compared with such from the FCB and bare OSB. Further analysis will be required to understand the occurrence of this temperature variation caused by the thermal degradation of both the vinyl siding and OSB.

Under the LHC (Table 4), the temperature difference between the exposed and the interface surface of the cedar siding was much lower as compare to such from the bare OSB at their corresponding failure points; yet flaming ignition occurred in the former, while only glowing ignition occurred in the latter. Similarly as for the HHC, under the LHC, FCB and EW prototypes exhibited approximately the same exposed surface temperatures with the difference that the FCB siding shielded effectively the prototype from the heat (no flaming or glowing ignition ensued on the OSB at the interface of the prototype) while the EW siding degraded to the point of a direct exposure of the OSB that leaded to flaming ignition. The vinyl siding melted at an early stage of the burn test as occurred under the HHC; though, its interface surface temperature was in agreement with the exposed surface of the bare OSB, suggesting that, at this heat flux condition, the thermal degradation of the vinyl siding did not affected the thermal response of the OSB.

6. MATHEMATICAL MODEL RESULTS AND DISCUSSION ANALYSIS

Several mathematical models have been developed to correlate the time to ignition (*TTI*) of materials that are typically used in building construction with the heat flux these materials are exposed to. In addition, materials have been classified based on their thermal response as thermally thin or thermally thick materials [40, 42, 43, 45].

A thermally thin material is typically considered to have a uniform temperature (physically thin materials). Thus, analytical models developed for these materials, consider that the temperature gradient inside the material can be neglected [45], i.e., the lumped capacity system applies [46]. For thermally thick materials, the temperature distribution corresponds to a semi-infinitely thick domain. Ignition, thus, is generally modeled as a one-dimensional heat conduction problem [45].

Janssens [43] proposed a simplified model of piloted ignition considering six oven dry thermally thick wood species (Western red cedar, red wood, Douglas-fir, Radiata pine, Victorian ash, and Blackbutt) exposed to radiant heat loads from 15 to 45 kW/m^2. Experimental data was obtained from cone calorimeter tests conducted in vertical orientation. Some of the considerations used to develop this model were:

- One-dimensional heat transfer perpendicular to the exposed surface.
- Specimens were considered as semi-infinite medium. (Thermally thick material criterion), with constant and temperature-dependant thermal properties.
- Solution for semi-infinite medium was approximated with a truncated series expansion.

- A constant, total heat transfer coefficient of h= 13.5 kW/m^2-K was defined for vertically-oriented Cone Calorimeter tests.

Results suggested that it was possible to plot $TTI^{0.547}$ versus the heat flux load which enabled to find a critical heat flux and to determine the thermal inertia, $k\rho c$, of the wooden materials tested.

Li and Drysdale [40] used the model developed by Janssens [43] to evaluate piloted ignition of four horizontal species of wood under radiant heat fluxes for 15 to 32 kW/m^2. The species of wood were two softwoods (White pine and Western red cedar) and two hardwoods (Brazilian mahogany and Obeche). Results showed that the response of the wooden materials felt into two regimes. At 24 kW/m^2 and above, the ignition event could be timed precisely. At 19.7 kW/m^2, glowing ignition it was observed before flaming initiated where the surface temperatures were higher and the scatter was greater than that for higher heat fluxes.

Lamorlette and Candelier [45] analyzed the theoretical transition to delineate thermally thick and thermally thin materials developing a one-dimensional, finite-length, dimensionless, heat conduction model. For the development of this model, the boundary conditions at both of the surfaces of a solid, considered both convective and radiant heat losses through a total heat transfer coefficient (h), to linearize the approximation for the radiant re-emission. In spite of that additional complexity, solutions suggested for the first zero (first eigenvalue) were used to define a fully analytical expression for large time scale. The transition between the thick and thin material consideration, was assumed to occur at

matching small times scales by performing a time derivative of the difference between the thick and thin equations developed.

Tran and Cohen [42] recognized three approaches to predict piloted ignition, which were:

- The "heat soak" concept, which refers to correlating ignition time with the imposing heat flux from a bench-scale test.
- An assumption of a minimum mass flux of volatiles for a pyrolyzing solid.
- The ignition and flame spread theory developed by Quintiere [41, 47, 48], which is based on the thermally thin or thick material criteria.

Shi and Chew [49] reviewed several studies for the fire process modeling of combustible materials under external heat flux: 27 studies for woods, 14 for non-charring polymers, 7 for charring polymers, and 20 for intumescent polymers. For all these studies, thermal, chemical and physical processes were often included in one-dimensional models.

In this work the thickness of each of the siding materials (Table 5) result in a small area that is much smaller than that of both the exposed and back surfaces, thus, irradiation is predominantly transferred from the exposed surface to the back surface of the siding material prototypes; i.e., in rectangular coordinates, the heat flux transferred in the direction of the axes that are parallel to the centerlines of the front surface of the prototype, are negligible when compared to the heat flux that is transferred in the direction of the axe that is perpendicular to the front surface. From the experimentally measured temperature profiles of this surface (Figures 11, 13, 17, 20, and 22), only the maximum temperatures profiles were relevant since, as afore mentioned (Section 5.2), the maximum temperatures exhibited by the siding materials were likely to onset the autoignition process.

The arrangement of thermocouples along the centerlines of the siding materials prototypes helped to effectively register the ignition event; having a thermocouple close to the region where flaming ignition started, resulted in the quantitative evidence desired of the failure point. However, the objective was to measure ignition temperatures and not to analyze the transient temperature distribution along the surfaces prototypes.

The transient temperature profiles from Figures 11, 13, 17, 20, and 22 varied due to the radiation scattering across a surface (Figure 27). Ideally, the exposed surface of the siding material is subjected to uniform irradiation; nevertheless, radiation between surfaces can propagate in all possible directions. Irradiation (rate at which radiation leaves a surface), and radiosity (rate at which radiation is incident on a surface), are highly dependent on the wavelength, temperature, emissivity, and preferential directions at which radiation propagates [50]; parameters that change as temperature increases with time.

Figure 27 shows fibre cement board during and after its exposure to radiant heat. This material allowed showing how radiation propagated over the surface of this material since it did not ignite under the heating conditions used. The faded circle in the central region of the material shows how radiation scattered across the surface; thereby, thermocouples that did register the *TTI* may have not registered the maximum temperatures required for the analysis. Figure 27(b) and 27(c) also show the location of the drills used to locate the clamps that fixed the thermocouples. A separation of at least one inch was left between the tip of a thermocouple and its corresponding clamp.

.

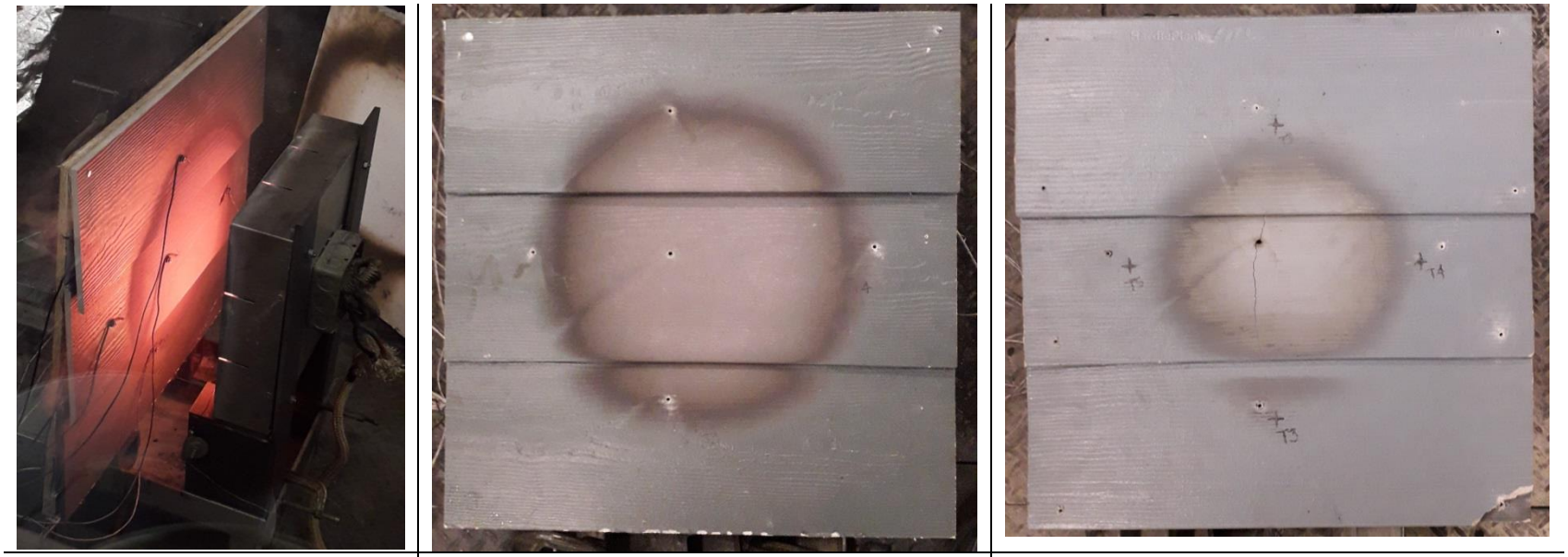

(a) (b) (c)

Figure 27 Radiation scattering over fibre cement board (a) during a burn test, (b) after exposure under the HHC, and (c) after exposure under the LHC. In (b) circular drills used to hold in place the supports for the thermocouples can be observed. In (c) these drills and black-colour marks where the thermocouples were located can also be observed.

Therefore, a one-dimensional, finite length scale, transient heat conduction model was used to predict the time to ignition (*TTI*) by means of an experimentally measured ignition temperature (T_{ig}) of the siding material. Rectangular coordinates were used. The radiant heat load was assumed to be uniform and the radiosity from the top, bottom, and sides of both, the siding and the sheathing material were neglected. All materials were assumed to be homogeneous, isotropic, and with constant thermal properties. Also, for simplicity, the siding material exposed surface was assumed to be flat for all the siding materials.

A schematic of the siding material array is shown in Figure 28. At the exposed surface ($x = 0$ in Figure 28), an incident heat flux q'' emitted from the radiant panel was incident over the complete exposed surface of the siding material. At both the exposed an back surface, convective and radiant heat losses exists; these losses are represented by $q''_{loss,front}$ and $q''_{loss,back}$ for the front and back surfaces, respectively ($x = L$ in Figure 28). As above mentioned, the top and bottom sides of the material can be treated as isolated boundaries.

Nonetheless, the solution of the described model will require numerical evaluation. Including the heat losses directly into the model makes it a non-linear, implicit problem because convective and radiative terms are dependent of the transient surface temperatures. In addition, this model will have to take into account non-linear equations to determine the heat transfer coefficient (h) [38, 45]. Furthermore, gas volatiles were released from the prototypes during the burn tests. These gas volatiles are generated by pyrolysis reactions when combustible materials are exposed under external heat flux. Pyrolysis reactions and the necessary properties to account for the generation of these gases are also non-linear and complex [33, 49, 51–53].

Simplifications can be made for the model to predict the surface temperatures and, thereby, obtain solutions for the *TTI* of the siding materials. A procedure towards the use of a simplified analytical model was proposed as follows:

a) The burn tests of the control material (OSB) were analyzed to estimate the heat losses generated through the entire tests. The control material can be used because (1) the experimental conditions were the same when testing the siding material prototypes and (2) the gas volatiles generated during pyrolysis of wood, the main component of OSB, are well known and their production has been largely analyzed [49]. Conversely, thermal decomposition of vinyl generates hydrogen chloride (HCl) and chlorinated dioxins [54]. Fibre cement board planks used were factory-coated with a primer that contains titanium dioxide, categorized as flammable material [55]. However, the thermal response of the prototypes was, to some extent, related to the response of wooden materials under radiant heating conditions. For example, vinyl siding deformed and left the OSB directly exposed to the radiant heat; cedar siding is a wooden material; and engineered wood is composed of wooden and synthetic fibres [36]. Thus, an analytical model was developed for the control material as a one-dimensional, finite length scale, transient heat conduction model (**Calibration Model**).
b) An extensive evaluation of the heat losses was performed when air properties for both surfaces was considered. Derived from this evaluation, recommendations to simplify this type of analysis were provided on a quantitative basis.

c) Finally, these simplifications were included in a one-dimensional, finite length scale, transient heat conduction model for the siding material prototypes (**Siding material Model**).

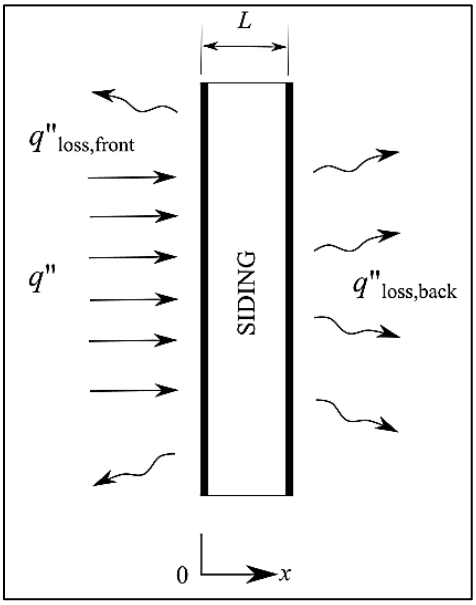

Figure 28 *Schematic of the heat transfer model for the siding material.*

6.1 Total heat losses and radiation between surfaces

6.1.1 Vertical flat plate subjected to natural convection

To determine the total heat losses from the solid shown in Figure 28, it was treated as a vertical flat slab subjected to natural convection which, simultaneously, was radiating energy. Thus, convective and radiant heat losses were considered to obtain the total heat losses for the exposed and back surface of the OSB. For the convective heat losses, values of the heat transfer coefficient (h) are required. Correlation equations that are used to determine h, depend on (1) the orientation and geometry of the samples, (2) the variation of temperature on the surface, (3) the fluid flow regime (laminar, turbulent, or a transition

between laminar and turbulent flow), and (4) the thermophysical properties of the fluid involved [38]. Also, correlation equations for the Nusselt number (Nu = $h \cdot L/k$) that are used to calculate heat transfer coefficients for isothermal plates can also be used for plates subjected to a constant heat flux [38], which is the case of this analysis.

Nusselt number (Nu) correlations were used to determine the transfer heat coefficient. To address the flow regime dependency, a free stream flow velocity was required. The fuel-gas velocity was not measured during the burn tests of the present study. A free stream velocity of 0.1 m/s was measured on a study where fire-retardant chemicals were evaluated under radiant heat [56]. This velocity was used as reference towards the selection of the appropriate Nusselt number (Nu) correlation. When buoyancy effects are dominant, inertia forces are negligible, i.e., natural convection occurs [38]. To evaluate which of either buoyancy or inertial effects dominate, the Grashof number (Gr) and the Reynolds number (Re) need to be compared as follows:

$$\frac{\mathrm{Gr}}{\mathrm{Re}^2} >> 1, \text{ inertia forces are negligible,} \tag{1a}$$

$$\frac{\mathrm{Gr}}{\mathrm{Re}^2} << 1, \text{ inertia forces must be considered,} \tag{1b}$$

$$\frac{\mathrm{Gr}}{\mathrm{Re}^2} \approx 1, \text{ both inertial and buoyancy effects must be considered,} \tag{1c}$$

Depending on the value resulting from Eq. (1), for natural convection condition, the correlation equation for the Nusselt number will be [38]:

$$\mathrm{Nu} = \left(0.825 + \frac{0.387\mathrm{Ra}^{1/16}}{\left(1+\left(\frac{0.492}{\mathrm{Pr}}\right)^{9/16}\right)^{8/27}} \right)^2 = \frac{h \cdot L}{k}, \tag{2}$$

Otherwise, for a forced convection condition, the correlation will be [38]:

$$\mathrm{Nu}_{\mathrm{forced}} = \left(\mathrm{Nu}_{\mathrm{Re}}^3 + \mathrm{Nu}^3 \right)^{1/3}, \tag{3}$$

where

$\mathrm{Nu}_{\mathrm{forced}}$ is the Nusselt number for a forced convection condition,

$\mathrm{Nu}_{\mathrm{Re}} = 0.453 \cdot \mathrm{Re}^{1/2} \cdot \mathrm{Pr}_{\mathrm{air}}^{1/3}$ is the regime-dependent term of $\mathrm{Nu}_{\mathrm{forced}}$ under the laminar flow regime, and

$\mathrm{Nu}_{\mathrm{Re}} = 0.0308 \cdot \mathrm{Re}^{0.8} \cdot \mathrm{Pr}_{\mathrm{air}}^{1/3}$ is the regime-dependant term of $\mathrm{Nu}_{\mathrm{forced}}$ under the turbulent flow regime.

All the fluid properties were calculated at the film temperature,

$$T_{film} = \frac{T(t) + T_\infty}{2}. \tag{4}$$

Regarding the thermal properties required for Eq. (1) to (3), Figure 29(a) shows that fuel-gases were released from the exposed surface of the OSB during a burn test. Although, Figure 29(b) shows that at the back surface of the OBS sheet, little or no gases were released; only the surrounding air took part in the convective heat transfer. Therefore, at the exposed surface, properties of a fuel-gas mixture were used, whereas for the back surface, air properties were used. As a subsequent exercise towards a more simplified model, evaluation of the heat losses was performed considering air properties for both surfaces.

(a) Fuel gases generated at the exposed surface

(b) Air surrounding the back surface

Figure 29 *Heating conditions at (a) the exposed surface with fuel-gases and (b) back surface with surrounding air.*

6.1.2 Multi-component fuel-gas properties

Fuel-gas mixture properties were required to account for the chemical composition that the gases at the exposed surface of the OSB exhibited (Figure 29a). A stoichiometric analysis was conducted to determine the mass fractions of the gas volatiles produced at this surface because at a concentration near the stoichiometric and at the correct surface temperature, fuel vapours ascertain autoignition [47]. Thus, the mass fractions were inputs of multi-component gas mixture relations from which the gas mixture properties were determined. Finally, the convective and radiant heat losses were estimated.

Ragland and Aerts [52], who studied the properties of wood for combustion analysis, stated that the combustion by-products resulting from a combustion process are typically water vapor, carbon monoxide CO, carbon dioxide CO_2, light hydrocarbon gases (normally methane), and tar. Other studies where the prediction of gas volatiles from pyrolysis of wood under external heat fluxes was analysed, modeled the oxidation reactions typical of pyrolysis using the same combustion by-products [47, 49]. Since the combustion of most fuels mainly starts at the reaction of volatiles, it is important to determine the amount of each of the gas volatiles produced. Peters and Weber [57] proposed a two-step model to predict the production of gas volatiles assuming that C_xH_y, a given hydrocarbon generated from the wooden material, oxidizes to CO, H_2O, while intermediate CO oxidizes to CO_2. The resulting expressions and mass fraction coefficients for the stoichiometric reactions were

$$1kgC_xH_y + v_1 kgO_2 \rightarrow \frac{28mf_c}{12} kgCO + \frac{18(1-mf_c)}{2} kgH_2O\,, \tag{5}$$

$$1kgCO + v_2 kgO_2 \rightarrow (1+v_2)\, kgCO_2\,' \tag{6}$$

where

$$v_1 = \frac{32mf_c}{12} + \frac{16(1-mf_c)}{2} - \frac{28mf_c \cdot v_2}{12}$$

$$v_2 = \frac{16}{28}$$

mf_c is the mass fraction of carbon in C_xH_y, in kg/kg

There is no standard chemical formula for wood, which is the major component of the OSB, but a weight percentage of the carbon can be considered depending on the type of wood [49]. Timusk [58] investigated the moisture sorption and permeability properties of mill-fabricated OSB, whose composition was of 60% of Aspen (hardwood), 30% of Lodgepole Pine (softwood), 9% of Birch (hardwood), and 1% peeler cores which are wood elements left over from the veneer making process; hence, OSB was treated as a hardwood. Ragland and Aerts [52] also indicated that the carbon average weight percentage in hardwoods ranges from 50 to 53 %, where a value of 50.2 % of weight percentage of carbon content in hardwood was taken from [49]. Once the carbon mass fraction mf_c is known, the mass fractions mf_i of H_2O, CO, and CO_2 can be obtained from Eq. (5) and (6), and therefore, the fuel-gas composition. The mass fractions will serve to calculate the mole fractions y_i required to determine the gas mixture properties [53]. Several methods to determine the viscosity of low-pressure multicomponent mixtures have been developed. A simple method developed by Wilke (1950) has been extensively tested, showing average deviations of less than 1% when comparing values obtained from the model with data on 17 binary systems [53]. The relation to determine the viscosity of a multicomponent gas mixture proposed by Wilke was

$$\mu_{gas} = \sum_{i=1}^{n} \frac{y_i \mu_i}{\sum_{j=1}^{n} y_i \varphi_{ij}}, \tag{7}$$

where

$$\varphi_{ij} = \frac{\left[1 + \left(\frac{\mu_i}{\mu_j}\right)^{1/2} \left(\frac{M_j}{M_i}\right)^{1/4}\right]^2}{\left[8\left(1 + \frac{M_i}{M_j}\right)\right]^{1/2}}, \tag{8}$$

where

μ_{gas} is the dynamic viscosity of the fuel-gas mixture, in kg/m-s

μ_i or μ_j is the dynamic viscosity of the pure component, in kg/m-s

y_i is the mole fraction the pure component, in kmol/kmol

M_i or M_j is the molecular weights of the pure component, in kg/kmol

i and j are the subscripts corresponding to the pure components where *i, j* = 1, 2, and 3, corresponding to the pure components CO, H_2O, and CO_2, respectively.

Similarly, the relation for estimating mixture viscosities is also applicable to thermal conductivities by simply substituting μ for k [53], resulting

$$k_{gas} = \sum_{i=1}^{n} \frac{y_i k_i}{\sum_{j=1}^{n} y_i \varphi_{ij}}, \tag{9}$$

where

$$\varphi_{ij} = \frac{\left[1 + \left(\frac{k_i}{k_j}\right)^{1/2} \left(\frac{M_j}{M_i}\right)^{1/4}\right]^2}{\left[8\left(1 + \frac{M_i}{M_j}\right)\right]^{1/2}}, \tag{10}$$

where

k_{gas} is the thermal conductivity of the fuel-gas mixture, in W/m-°C

k_i or k_j is the thermal conductivity of the pure component, in W/m-°C

The specific heat c and density ρ for the gas mixture were obtained using common expressions for intrinsic properties of multicomponent gas mixtures [59] such as

$$c_{gas} = \sum_{i=1}^{n} mf_i \cdot c_i \,, \tag{11}$$

$$v_{gas} = \sum_{i=1}^{n} mf_i \cdot v_i \,, \tag{12}$$

where

c_{gas} is the specific heat of the fuel-gas mixture, in J/kg-°C

c_i is the specific heat of the pure component, in J/kg-°C

v_{gas} is the specific volume of the fuel-gas mixture, in m^3/kg

v_i is the specific volume of the pure component, in m^3/kg

The properties for the pure components in Eq. (11) and (12) were calculated using their corresponding partial pressures, $p_i = y_i p_\infty$, where p_∞ is the atmospheric pressure, since the burn test were conducted in a room at open air conditions. The inverse of Eq. (12), will result in the fuel-gas density; value required to determine the kinematic viscosity of the gas mixture. From Eq. (7), (9), and (11), the Prandtl number (Pr) for the gas mixture was determined as

$$\mathrm{Pr}_{gas} = \frac{\mu_{gas} c_{gas}}{k_{gas}} \,, \tag{13}$$

Finally, the heat losses, which comprises the convective, Eq. (14), and radiant heat losses Eq. (15), for both the fuel-gas mixture and air, were determined using the Fourier cooling law and the Stefan-Boltzmann law, respectively as

$$q''_{\text{conv}} = h(T(t)) \cdot \left[T(t) - T_{\infty}\right], \tag{14}$$

$$q''_{\text{rad}} = \varepsilon \cdot \sigma \cdot \left[T(t)^4 - T_{\infty}^4\right], \tag{15}$$

At the commencement of the burn tests, a carbon layer started to form over the exposed surface of the siding material prototypes. Thus, for the exposed surface case, an emissivity value, ε, accounting for the carbon layer was considered. A value of 0.8 was assigned [43], [52]. For the unburnt surface (back surface) a value of 0.9 was used [39].

Equations (1) to (15) depend on the transient temperatures of the surfaces under analysis. For this reason, polynomial regressions were generated for each temperature. The duration of each burn test of the OSB, though, was not the same; therefore, the number of temperature data was uneven, e.g., under the HHC, the *TTIs* for the OSB were 396 s for Test 1, 510 s for Test 2, and 393 s for Test 3. An average regression might be obtained per test, but an average of the total number of measured temperatures profiles (from all tests) would not be accurate. The fact that the dependant variable (temperature) is averaged does not necessarily present any difficulties for regression analysis; however, it may produce inconsistent estimates [60].

Thus, the approach consisted in utilizing all the maximum temperature profiles of each test to obtain linear or non-linear regressions for each of the surfaces. With non-linear regressions for example, there is no need to rearrange the original experimental results prior to analysis, and so there is no distortion of the original error distribution [61].

Figure 30 and 31 show the maximum temperature profiles from the back surface of the control material under the HHC and the LHC, respectively. The number of data points per test (n_{test}) is also shown where the sampling frequency was 0.3 Hertz. Along with these profiles, the resulting polynomic regressions and the R^2, which refers to the proportion of the variance for a dependent variable (T) that is explained by an independent variable (t), are also shown.

Similarly, Figure 32 and 33 show the temperature profiles from the exposed surface under the HHC and the LHC, respectively. To generate more accurate regressions of exposed surface, it was convenient to split the data in two sections. For the HHC, the first section was obtained for the interval $0 < t < 21$ (Figure 34(a)), while the second section was for the interval $21 \leq t \leq 500$ (Figure 34(b)), rounding the longest *TTI* obtained (Test 2 under HHC). Similarly, for the LHC, two sections of the regression were obtained. The first section for the interval $0 < t < 15$ (Figure 34(c)), while the second section for the interval $15 \leq t \leq 600$ (Figure 34(d)).

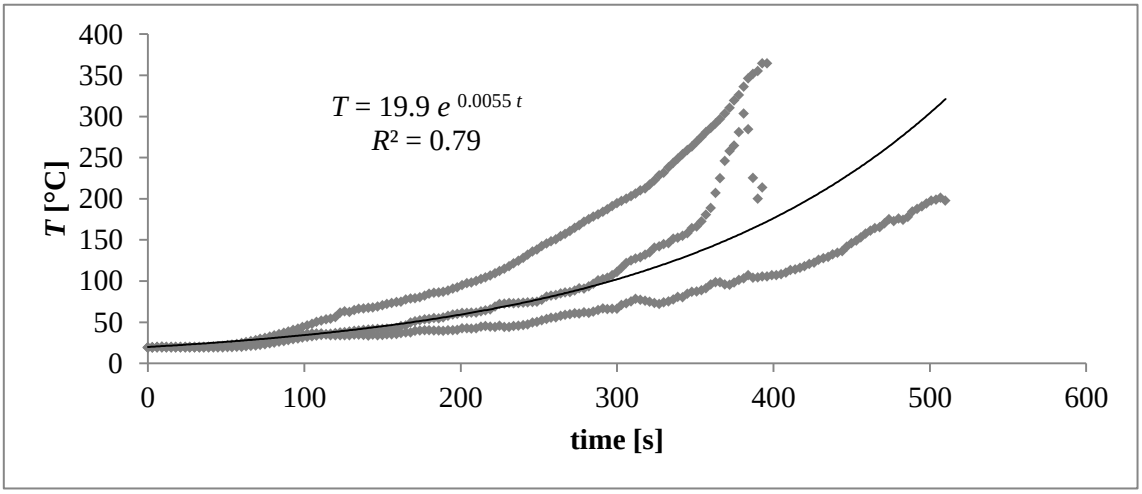

Figure 30 *Maximum, transient temperature profiles and regression for the back surface of the control material under HHC where* n_{test1} = 132, n_{test2} = 170, *and* n_{test3} = 131. *Points represent the raw data and the solid black line represents the regression.*

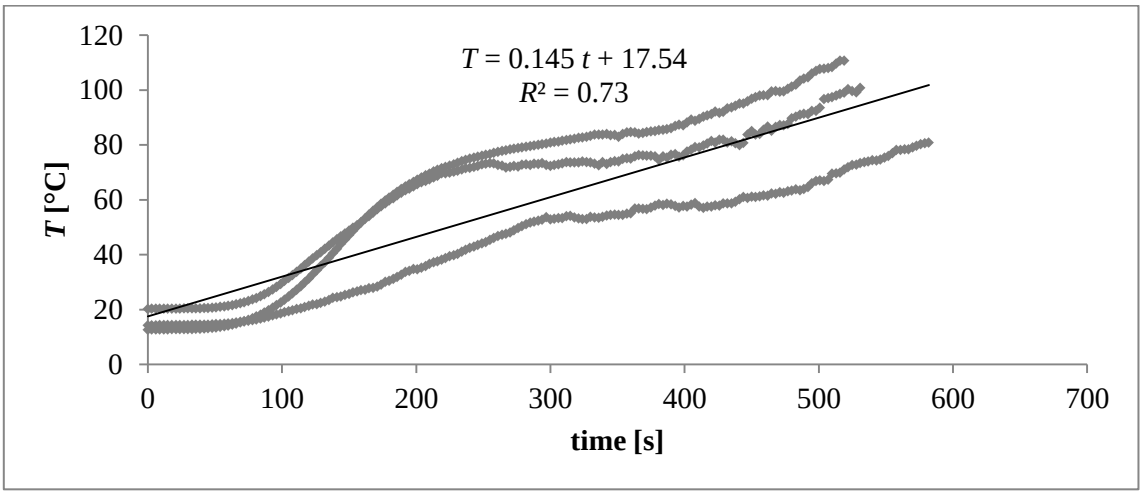

Figure 31 *Transient temperature profiles and regression for the back surface of the control material under LHC where* n_{test1} = 177, n_{test2} = 173, *and* n_{test3} = 194. *Points represent the raw data and the solid black line represents the regression.*

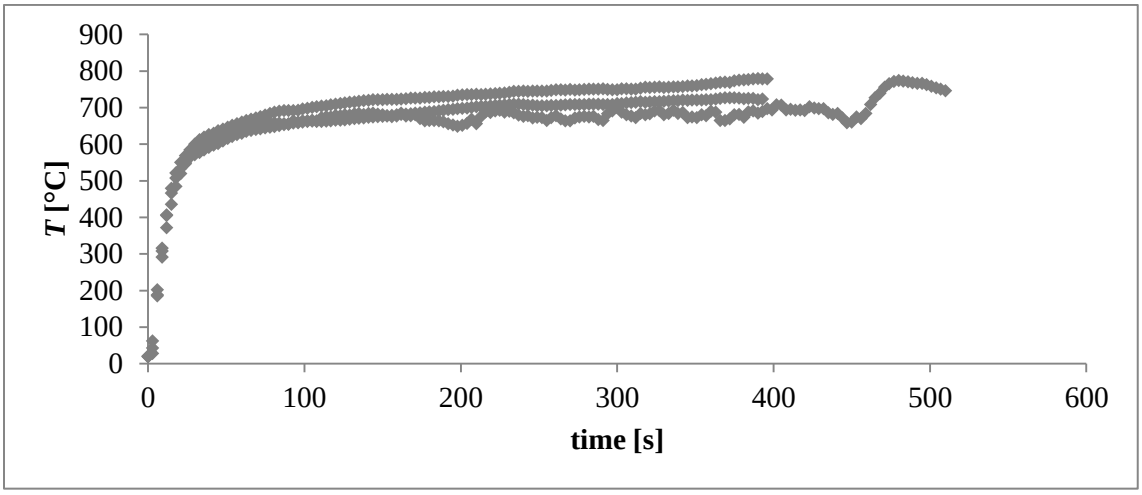

Figure 32 *Transient temperature profiles measured from the exposed surface of the control material under HHC where* n_{test1} = 132, n_{test2} = 170, *and* n_{test3} = 131. *Points represent the raw data.*

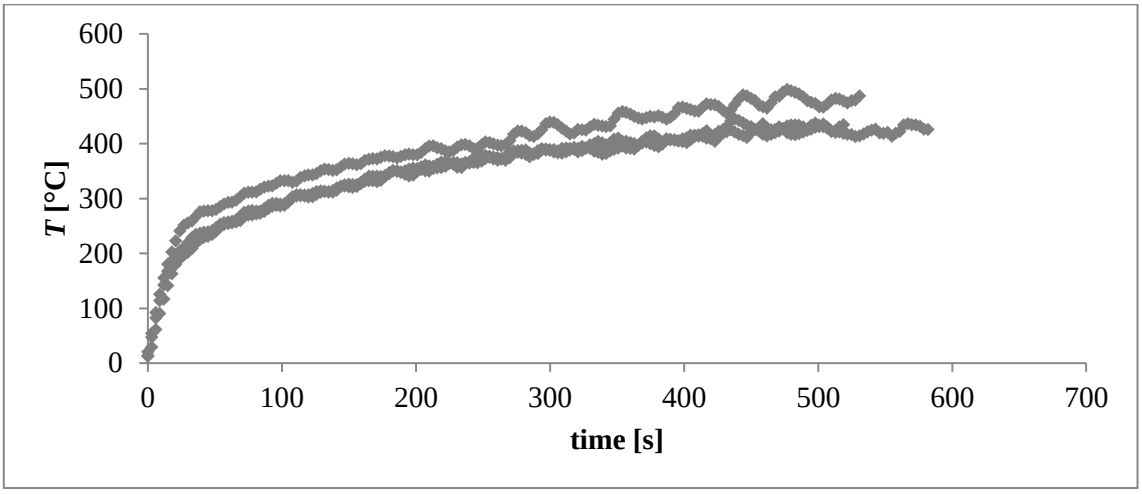

Figure 33 *Transient temperature profiles measured from the exposed surface of the control material under LHC where* n_{test1} = 177, n_{test2} = 173, *and* n_{test3} = 194. *Points represent the raw data.*

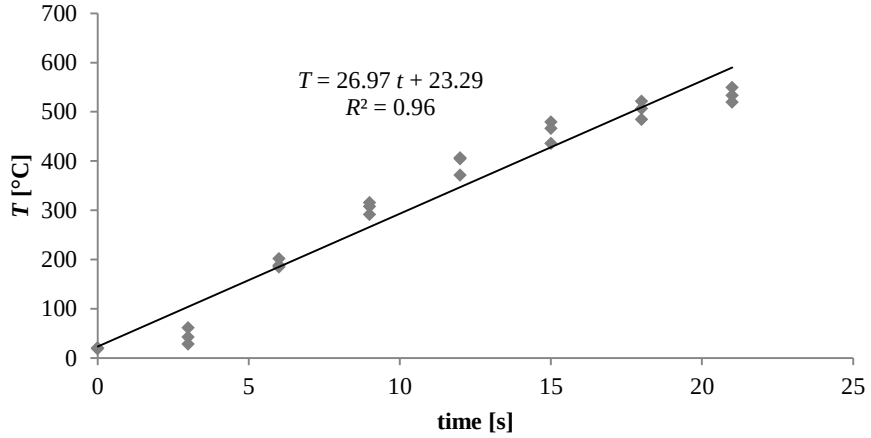

(a) Regression for the interval $0 < t < 21$

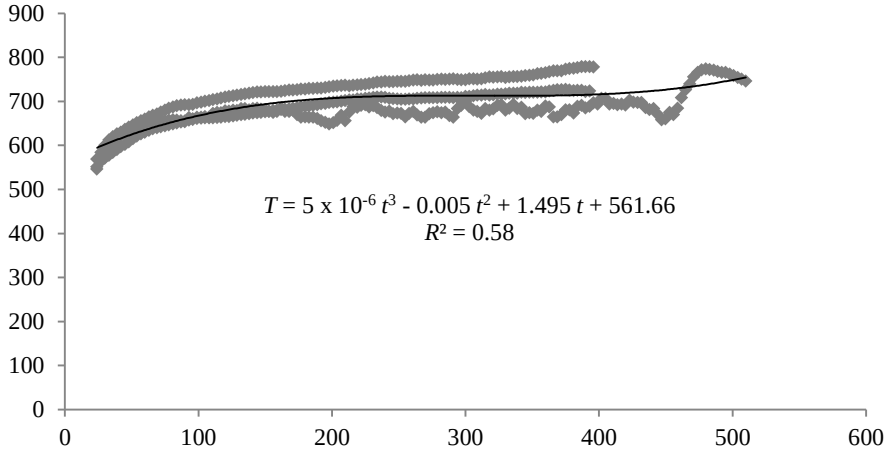

(b) Regression for the interval $21 \le t \le 500$

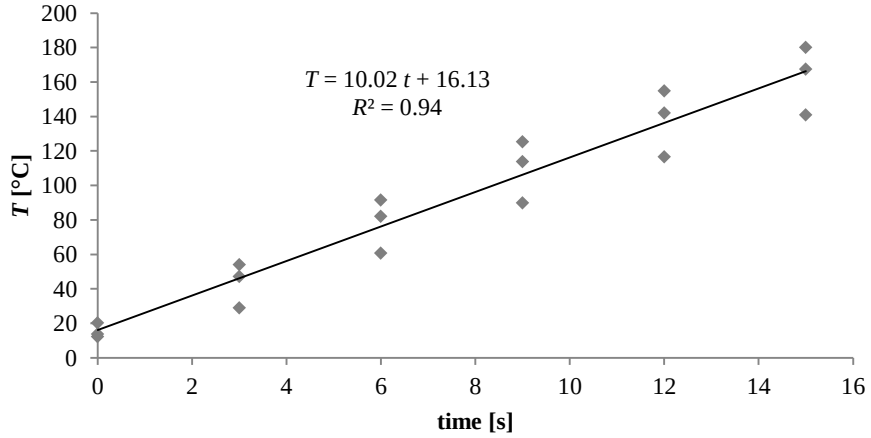

(c) Regression for the interval $0 < t < 15$

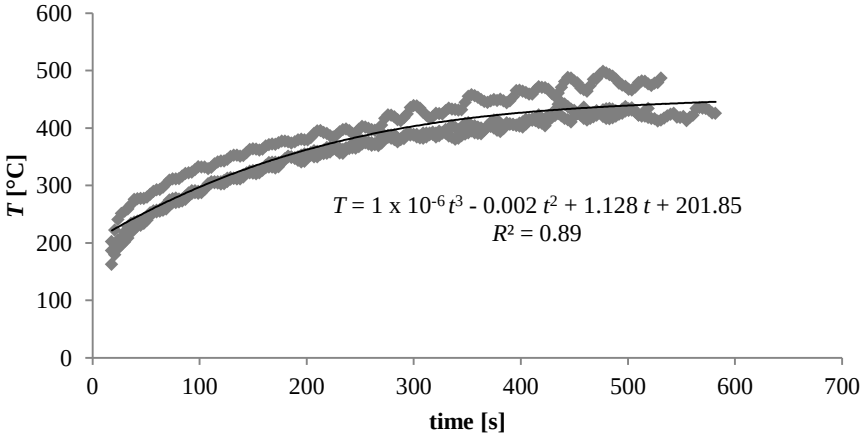

(d) Regression for the interval $15 \le t \le 600$

Figure 34 *Transient temperature profiles and regressions for the exposed surface of the control material under (a) and (b) HHC, and (c) and (d) LHC. Points represent the raw data and the solid black lines represent the regression.*

An EES (F-Chart, F-Chart Software LLC., Madison, WI, USA) code was used to determine the pure compound properties of air, H_2O, CO, and CO_2. These properties were computed using the regressions from Figure 30, Figure 31, and Figure 34. The EES code was also used to evaluate Eq. (1) to (16) obtaining the total heat loss for both the exposed surface and the back surface. The total heat loss for each surface comprises of both convective and radiative terms as follows:

$$q''_{loss} = q''_{conv} + q''_{rad}, \tag{17}$$

where q''_{conv} and q''_{rad} correspond to the convective and radiant heat losses as expressed in Eq. (14) and (15), respectively.

Figure 35 show the resulting transient profiles of the convective heat losses computed under the HHC when gas volatiles and air properties were considered for the exposed surface. Figure 36 show such profiles obtained using the same considerations, but for the LHC. Eq. (18) show the corresponding regressions obtained for the convective heat losses under the HHC and Eq. (19) such for the LHC.

$$q''_{conv,gas} = 2x10^{-9}t^3 - 2x10^{-6}t^2 + 7x10^{-4}t + 0.15 \text{ for } 0 \le t \le 500 \text{ with } R^2 = 0.99, \tag{18a}$$

$$q''_{conv,air\,1} = 0.22\ \ t - 0.14 \text{ for } 0 \le t < 21 \text{ with } R^2 = 0.99, \tag{18b}$$

$$q''_{conv,air\,2} = 4x10^{-8}t^3 - 4x10^{-5}t^2 + 0.012\ \ t + 4.22 \text{ for } 21 \le t \le 500 \text{ with } R^2 = 0.99, \tag{18c}$$

$$q''_{conv,gas} = -3x10^{-7}t^2 + 3x10^{-4}t + 0.03 \text{ for } 0 \le t \le 600 \text{ with } R^2 = 0.99, \tag{19a}$$

$$q''_{conv,air\,1} = 0.066\ \ t - 0.07 \text{ for } 0 \le t < 15 \text{ with } R^2 = 0.99, \tag{19b}$$

$$q''_{conv,air\,2} = -9x10^{-6}t^2 + 0.007\ \ t + 1.35 \text{ for } 15 \le t \le 600 \text{ with } R^2 = 0.99. \tag{19c}$$

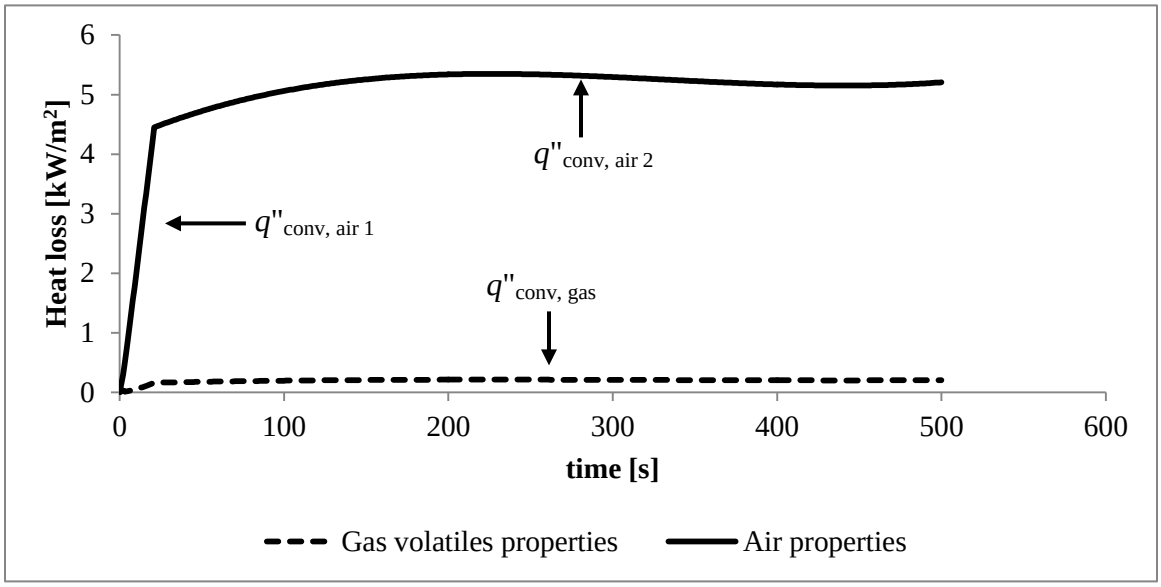

Figure 35 *Convective heat loss profiles from the exposed surface of the control material under HHC.*

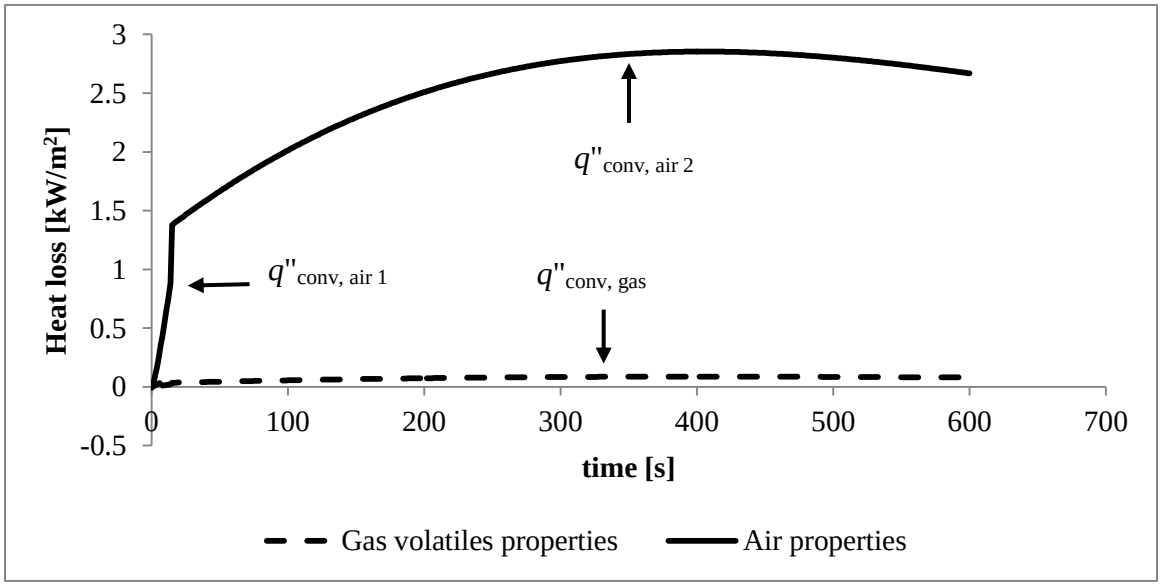

Figure 36 *Convective heat loss profiles from the exposed surface of the control material under LHC.*

Figure 37 and 38 show the resulting transient profiles of the radiant heat losses computed under the HHC and the LHC, respectively. Radiant heat is independent of the properties of the fluid, thus, only one profile resulted for each heating condition.

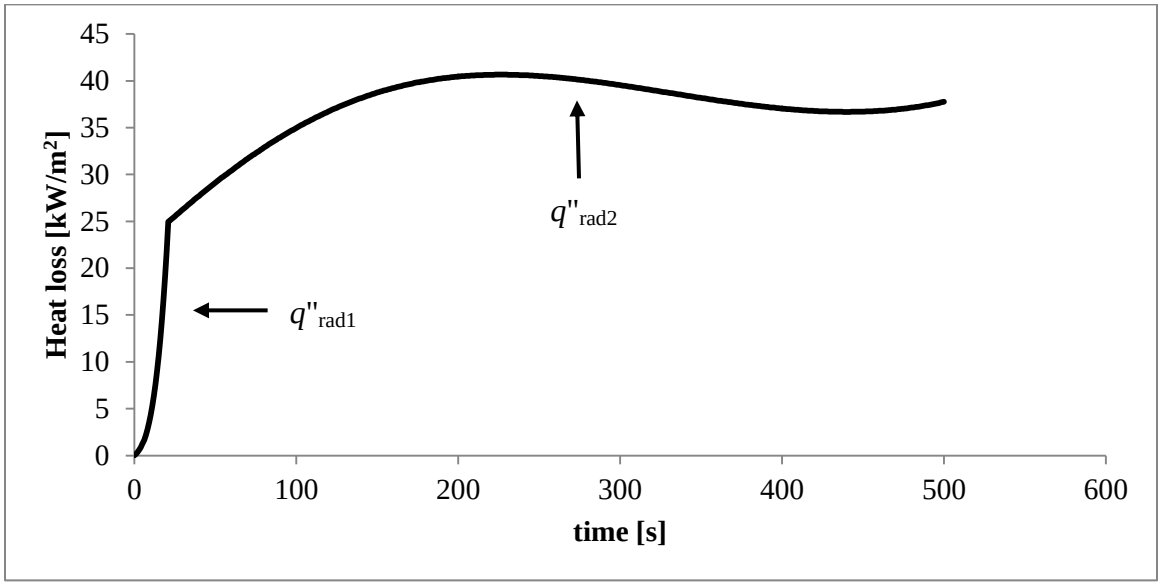

Figure 37 *Radiant heat loss profile from the exposed surface of the control material under HHC.*

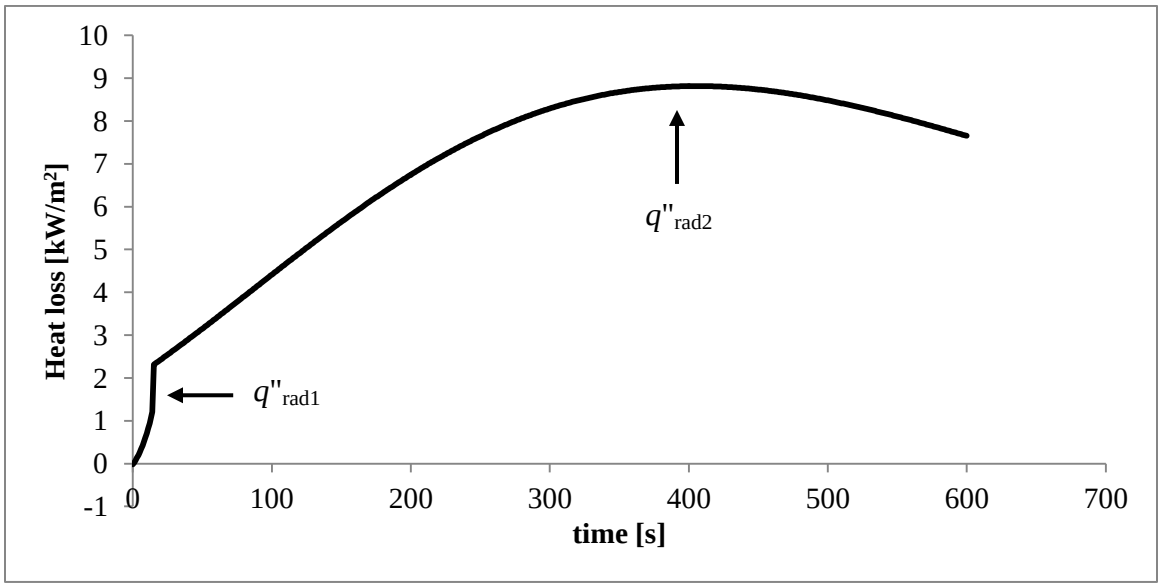

Figure 38 *Radiant heat loss profile from the exposed surface of the control material under LHC.*

Similar to the convective heat losses, Eq. (20) show the corresponding regressions obtained for the radiant heat losses under the HHC and Eq. (21) such for the LHC.

$$q''_{\text{rad }1} = 0.066\ \ t^2 - 0.3\ \ t + 0.66 \text{ for } 0 \le t < 21 \text{ with } R^2 = 0.99, \quad (20a)$$

$$q''_{\text{rad }2} = 7x10^{-7} t^3 - 7x10^{-4} t^2 + 0.22\ \ t + 19.9 \text{ for } 21 \le t \le 500 \text{ with } R^2 = 0.99, \quad (20b)$$

$$q''_{\text{rad }1} = 0.087\ \ t - 0.118 \text{ for } 0 \le t < 15 \text{ with } R^2 = 0.98, \quad (21a)$$

$$q''_{\text{rad }2} = -4x10^{-5} t^2 + 0.035\ \ t + 1.47 \text{ for } 15 \le t \le 600 \text{ with } R^2 = 0.99. \quad (21b)$$

Finally, Figure 39 shows the convective and radiant heat losses for the back surface under the HHC and Figure 40 such for the LHC. In the same manner, Eq. (22) and Eq. (23) show the correlations obtained for the heat losses at the back surface under the HHC and the LHC, respectively.

$$q''_{\text{conv}} = 2x10^{-8} t^3 - 5x10^{-6} t^2 + 0.001\ \ t - 0.024 \text{ for } 0 \le t \le 500 \text{ with } R^2 = 0.99, \quad (22a)$$

$$q''_{\text{rad}} = 0.03\ \ e^{0.012\ t} \text{ for } 0 \le t \le 500 \text{ with } R^2 = 0.98, \quad (22b)$$

$$q''_{\text{conv}} = 5x10^{-7} t^2 + 6x10^{-4} t - 0.018 \text{ for } 0 \le t \le 600 \text{ with } R^2 = 0.99, \quad (23a)$$

$$q''_{\text{rad}} = 7x10^{-7} t^2 + 7x10^{-4} t - 0.01 \text{ for } 0 \le t \le 600 \text{ with } R^2 = 0.99. \quad (23b)$$

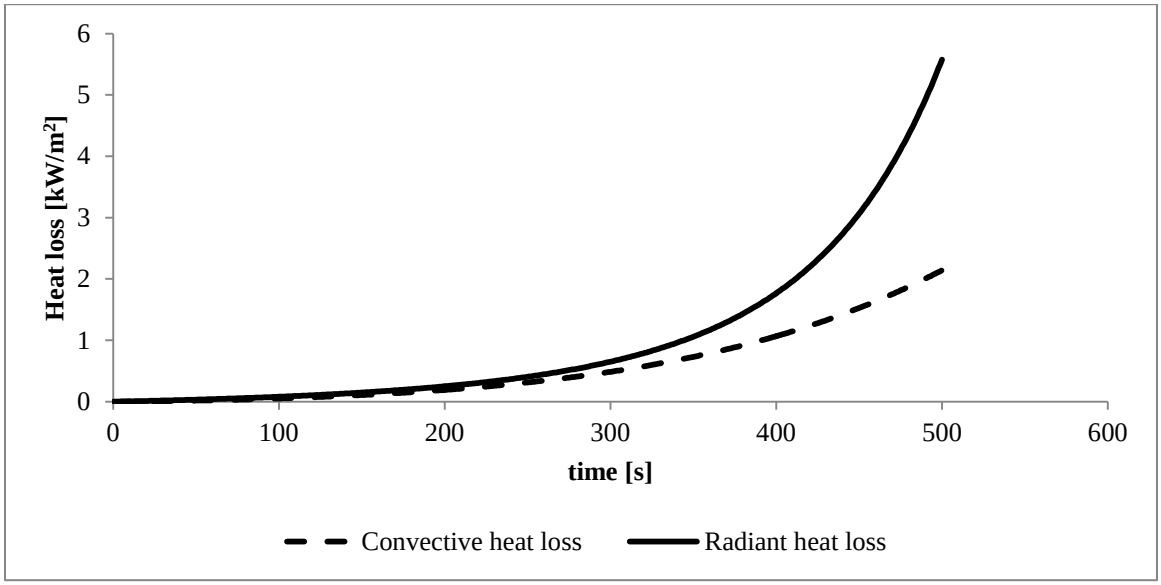

Figure 39 *Convective and radiant heat losses for the back surface under the HHC.*

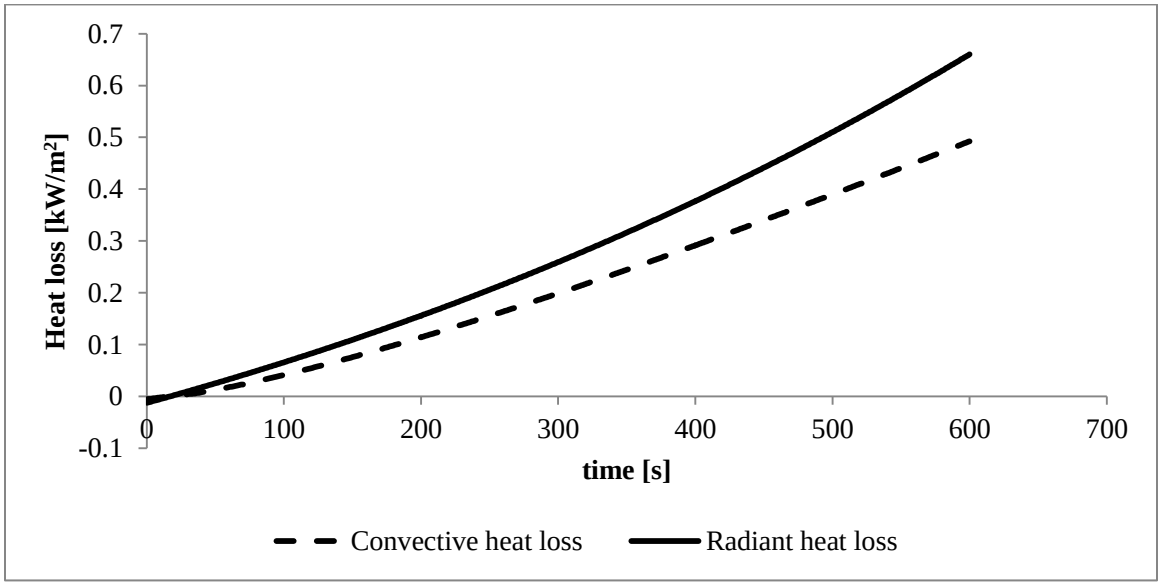

Figure 40 *Convective and radiant heat losses for the back surface under the LHC.*

To totalize the energy loss during the complete test, Δt_{test}, an integration from t = 0 to t = 500 s was performed for the HHC, and from t = 0 to t = 600 s for the LHC. Due that the result of an integration of power over time will be equal to energy units; this energy amount was divided by the corresponding test duration to obtain the total heat losses in congruent units; thus, the total heat losses for the exposed surface (THL_{Exp}) were estimated as

$$THL_{\text{Exp}} = \frac{\int_{t=0}^{t=500} q''_{\text{LossExp}}\, dt}{\Delta t_{test}} = \frac{\int_{t=0}^{t=500} \left(q''_{\text{conv}} + q''_{rad} \right)\Big|_{\text{Exp}}\, dt}{\Delta t_{test}}, \tag{24}$$

while the total heat loses for the back surface (THL_{Back}) were

$$THL_{\text{Back}} = \frac{\int_{t=0}^{t=600} q''_{\text{LossBack}}\, dt}{\Delta t_{test}} = \frac{\int_{t=0}^{t=600} \left(q''_{\text{conv}} + q''_{rad} \right)\Big|_{\text{Back}}\, dt}{\Delta t_{test}}. \tag{25}$$

Finally, when the total heat losses of the exposed surface were subtracted from the HHC and LHC, the remaining heat was an effective heat flux, q''_{EFF}, as this was the effective amount of radiant heat that affected the OSB. The effective heat flux for the HHC q''_{EFF_HHC} was estimated as

$$q''_{\text{EFF, HHC}} = q''_{\text{HHC}} - THL_{\text{Exp}}, \tag{26}$$

whereas for the LHC, the effective heat flux q''_{EFF_LHC} was

$$q''_{\text{EFF, LHC}} = q''_{\text{LHC}} - THL_{\text{Exp}}. \quad (27)$$

Table 6 shows a summary of the results obtained from Eq. (18) to (27). Important differences were distinguished when using air or gas volatiles properties for the computation of the heat losses. This result suggested that a mass of gas volatiles could allow heat to diffuse faster into the solid material than a mass of air, thereby, under the high temperatures reached during the burn tests, air would remove more heat that gas volatiles.

The last two columns in Table 6 show the percentages obtained for the convective and radiant heat losses with respect to the total heat loss estimated at the exposed surface, THL_{Exp}. Derived from these quantitative results, it can be stated that, in spite of the differences observed when using gas volatiles or air properties for the estimation of the convective losses, its contribution to the THL_{Exp} was minimum. Conversely, the estimated radiant heat losses for both surfaces under analysis and heating conditions were predominant. Radiant heat losses accounted for above 70 % of the estimated total heat losses. Therefore, a first simplification to the analytical model can be considered: the convective losses in Eq. (17) can be neglected, thus, the heat losses will only be comprised of radiant losses.

Furthermore, the estimated total heat losses for the back surface, THL_{Back}, where 2.446 kW/m^2 and 0.506 kW/m^2 for the HHC and LHC, respectively, which are thermal losses that can be neglected due to its low magnitudes when compared to the heating condition values. Hence, a second simplification can be proposed: heat losses at the back

surface of the prototypes can be neglected, thereby; a boundary condition of the first kind can be assigned, which in this case, is a transient surface temperature, $T(t)$.

Therefore, the effective heat flux included for the analytical model was determined by subtracting the total radiant heat losses of the exposed surface to the heating condition as:

$$q''_{\text{EFF, HHC}} = q''_{\text{HHC}} - q''_{\text{rad, Exp}} = 19.22 \text{ kW/m}^2, \text{ and} \quad (28a)$$

$$q''_{\text{EFF, LHC}} = q''_{\text{LHC}} - q''_{\text{rad, Exp}} = 13.16 \text{ kW/m}^2. \quad (28b)$$

Implying that, simplifications can be applied to an analytical model provided an extensive analysis for the transient temperature-dependant fluid properties required for estimating the heat transfer coefficient and subsequently the transient convective heat losses from the experimental burn tests. In the following section, the application of the simplified boundary condition mentioned is presented.

Table 6 *Comparison between the heat losses estimated using gas volatiles and air properties for the control material.*

		HHC = 57 kW/m^2			LHC = 20.3 kW/m^2			(HL_{ES}/THL_{Exp})x100	
		Gas volatiles (GV) properties @ES[1]	Air properties @ES	Air properties @BS[2]	Gas volatiles (GV) properties @ES	Air properties @ES	Air properties @BS	HHC	LHC
Heat losses (HL) [kW/m^2]	q''_{conv}	0.221	5.037	0.434	0.084	2.344	0.222	Using GV = 0.58 % Using air = 11.77 %	Using GV = 1.16 % Using air = 24.72 %
	q''_{rad}	37.771	37.771	2.012	7.138	7.138	0.284	Using GV = 99.42 % Using air = 88.23 %	Using GV = 98.84 % Using air = 75.28 %
	THL_{Exp}	37.992	42.808	N/A	7.222	9.482	N/A	N/A	
	THL_{Back}	N/A	N/A	2.446	N/A	N/A	0.506		
Effective heat [kW/m^2]	q''_{EFF}	19.008	14.192	N/A	13.078	10.818	N/A		

[1]ES = Exposed Surface, [2]BS = Back Surface, N/A = Not Applicable

6.2 One-dimensional, finite length scale, transient heat conduction model for the control material (Calibration Model)

For the Calibration Model, the governing equation of the temperature distribution, the boundary conditions, and the initial condition are:

$$\frac{\partial^2 T(x,t)}{\partial x^2} = \frac{1}{\alpha}\frac{\partial T(x,t)}{\partial t}, \tag{29}$$

$$-k\frac{\partial T(x=0,t)}{\partial x} = q'', \tag{30}$$

$$T(x=L,t) = T(t), \tag{31}$$

$$T(x,t=0) = T_{\infty}. \tag{32}$$

Eq. (30) describes the heat flux that was irradiated to the OSB. For this analysis, results from this model were compared when the heat flux input to the model was q'' and q''_{EFF}, i.e., a heat flux with and without considering the heat losses. Also, as described in Subsection 6.1.2, experimentally measured temperatures were used to set the boundary condition at the back surface, Eq. (31). Figure 41 shows a schematic of the model used for the analysis of the control material.

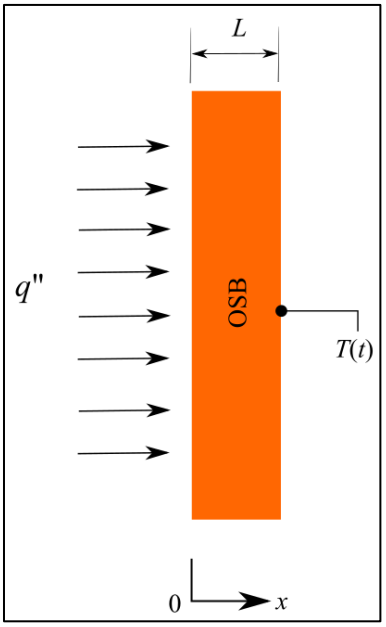

Figure 41 *Schematic of the heat transfer model for the control material.*

Equations (30) and (31) are non-homogeneous boundary conditions. To deal with the non-homogenous boundary conditions, an auxiliary, homogeneous problem was first solved. This auxiliary problem result when the non-homogenous boundary conditions are assumed to be homogeneous, that is, by replacing the non-homogenous terms in the boundary conditions with zero. Next, Green's functions were employed to account for the non-homogenous boundary conditions along with the initial condition. The general solution is expressed, in rectangular coordinates, in terms of the one-dimensional Green's function as [62]:

$$T(x,t) = \int_{L} G(x,t \mid x',\tau)\mid_{\tau=0} F(x')dx' + \frac{\alpha}{k}\int_{\tau=0}^{t} d\tau \sum_{i=1}^{2} G(x,t \mid x',\tau)\mid_{x'=x_i} \frac{1}{k_i} f_i \,, \tag{33}$$

where $G(x,t \mid x',\tau)\mid_{\tau=0}$ is the Green's function determined by solving the homogeneous part of the heat conduction problem, the auxiliary problem. Once $G(x,t \mid x',\tau)\mid_{\tau=0}$ is available,

the general form of the Green's function, $G(x,t\,|\,x',\tau)$, can be determined. F and f represent the non-homogenous initial and boundary conditions of the governing equation, respectively.

Thus, to find $G(x,t\,|\,x',\tau)|_{\tau=0}$, the boundary conditions of the auxiliary problem take the form:

$$-k\frac{\partial T(x=0,t)}{\partial x}=0\,, \tag{34}$$

$$T(x=L,t)=0\,. \tag{35}$$

The method of separation of variables was used to solve the governing equation. This method was applied directly since the governing equation and the boundary conditions are homogeneous for the auxiliary problem. A solution was assumed of the form $T(x,t)=X_n(x)\cdot\tau_n(t)$. Separating the variables and setting the resulting equations equal to the separation constant $\pm\lambda^2{}_n$, yields

$$\frac{d^2X_n(x)}{dx^2}+\lambda_n^2X_n(x)=0\,, \tag{36}$$

$$\frac{d\tau_n(t)}{dt}+\lambda_n^2\tau_n(t)=0\,, \tag{40}$$

where the positive sign was selected for both Eq. (36) and (40) since the problem is transient [46]. When $n = 0$; $\lambda^2{}_0=0$, and the equations become

$$\frac{d^2X_0(x)}{dx^2}=0\,, \tag{41}$$

$$\frac{d\tau_0(t)}{dt} = 0\,. \tag{42}$$

The solutions for the ordinary differential equations (8), (9), (10), and (11) are

$$X_n(x) = A_n \sin(\lambda_n x) + B_n \cos(\lambda_n x)\,, \tag{43}$$

$$\tau_n(t) = C_n \exp(-\alpha\lambda_n^2 t)\,, \tag{44}$$

$$X_0(x) = A_0 x + B_0\,, \tag{45}$$

$$\tau_0(t) = C_0\,. \tag{46}$$

Applying boundary conditions (34) and (35) to Eq. (45), and evaluating the initial condition (32) in Eq. (46), the solution for λ_0 vanishes from the general solution. Applying Eq. (34) to Eq. (43) gives

$$A_n = 0\,. \tag{47}$$

Applying Eq. (35) to Eq. (43) results in the characteristic equation

$$B_n \cos(\lambda_n L) = 0\,, \tag{48}$$

where

$$\lambda_n = \frac{(2n-1)\pi}{2L} \quad \text{for } n = 1,2,3\ldots,\infty. \tag{49}$$

Therefore, the homogeneous solution, is

$$T(x,t) = \sum_{n=1}^{\infty} a_n \cos(\lambda_n x) \exp(-\alpha\lambda_n^2 t) \quad \text{where } a_n = B_n C_n\,. \tag{50}$$

Applying the initial condition (32) to Eq. (50) results in

$$T(x, t=0) = T_\infty = \sum_{n=1}^{\infty} a_n \cos(\lambda_n x)\,. \tag{51}$$

The characteristic functions $\cos(\lambda_n x)$ in Eq. (50) are solutions to Eq. (36) which shows that is a Sturm-Liouville equation with a weighting function $w(x)=1$ [46]. Multiplying both sides of Eq. (50) by $\cos(\lambda_n x)$, integrating from x = 0 to x = L and utilizing the orthogonality property of the eigenfunctions, Eq. (50) gives

$$a_n = \frac{\int_{x'=0}^{L} T_\infty \cos(\lambda_n x')dx'}{\int_{x'=0}^{L} \cos(\lambda_n x')dx} = \frac{\int_{x'=0}^{L} T_\infty \cos(\lambda_n x')dx'}{L/2} \ , \tag{52}$$

where *x'* is used as a dummy integration variable. Substituting Eq. (52) into (51) gives

$$T(x,t) = \int_{x'=0}^{L} \left[\left(\frac{2}{L} \right) \sum_{n=1}^{\infty} \cos(\lambda_n x) \exp(-\alpha \lambda_n^2 t) \cos(\lambda_n x') \right] T_\infty dx' \ . \tag{53}$$

Eq. (53) was reorganized in order to compare it with the first term of Eq. (33), which represents the solution of the homogeneous problem in terms of Green's function. This comparison yields

$$G(x,t \mid x',\tau)\,|_{\tau=0} = \left(\frac{2}{L} \right) \sum_{n=1}^{\infty} \cos(\lambda_n x) \exp(-\alpha \lambda_n^2 t) \cos(\lambda_n x') \ . \tag{54}$$

The desired Green's function is determined by replacing *t* by $(t-\tau)$ [62] in Eq. (54) as

$$G(x,t \mid x',\tau) = \left(\frac{2}{L} \right) \sum_{n=1}^{\infty} \cos(\lambda_n x) \exp\left[-\alpha \lambda_n^2 \left(t-\tau \right) \right] \cos(\lambda_n x') \ . \tag{55}$$

Finally, substituting Eq. (55) into Eq. (33), to obtain the equation that represents the transient temperature distribution of the non-homogeneous problem is

$$T(x,t)=\left(\frac{2}{L}\right)\sum_{n=1}^{\infty}\cos(\lambda_n x)\exp\left(-\alpha\lambda_n^2 t\right)\int_{x'=0}^{L}\cos(\lambda_n x')T_\infty dx'+$$
$$+\alpha\int_{\tau=0}^{t}d\tau\left[\left(\frac{2}{L}\right)\sum_{n=1}^{\infty}\cos(\lambda_n x)\exp\left[-\alpha\lambda_n^2\left(t-\tau\right)\right]\cos(\lambda_n x')\right]_{x'=0}\left(\frac{q''}{k}\right)+ \quad , \qquad (56)$$
$$-\alpha\int_{\tau=0}^{t}d\tau\left[\frac{\partial}{\partial x'}\left\{\left(\frac{2}{L}\right)\sum_{n=1}^{\infty}\cos(\lambda_n x)\exp\left[-\alpha\lambda_n^2\left(t-\tau\right)\right]\cos(\lambda_n x')\right\}\right]_{x'=L}\cdot T(t)$$

where a substitution of the form $\frac{1}{k}G=-\frac{1}{h}\frac{\partial G}{\partial x'}$ was required in the third term of the right hand side (RHS) of Eq. (56) at the boundary condition at $x = L$ since k cannot be zero as in Eq. (33). This substitution comes from the general form of the boundary condition of the auxiliary problem

$$k\frac{\partial G}{\partial x'}+hG=0\text{, where } h=1. \qquad (57)$$

However, when Eq. (56) is evaluated at $x = L$, the solution does not converge to the boundary condition. This problem can be resolved by using integration by parts on the third term of the RHS of the Eq. (56) and replacing the resulting series expressions by their equivalent closed-form expression. Solving and evaluating the defined integrals, partial differentiation, using integration by parts, and rearranging terms, Eq. (56) becomes

$$T(x,t)=\left(\frac{2T_\infty}{L}\right)\sum_{n=1}^{\infty}\left(\frac{1}{\lambda_n}\right)(-1)^{n+1}\cos(\lambda_n x)\exp\left(-\alpha\lambda_n^2 t\right)+$$
$$+\left(\frac{2q''}{kL}\right)\sum_{n=1}^{\infty}\left(\frac{1}{\lambda^2{}_n}\right)\cos(\lambda_n x)\left[1-\exp\left(-\alpha\lambda_n^2 t\right)\right]+ \quad . \qquad (58)$$
$$-\left(\frac{2}{L}\right)\sum_{n=1}^{\infty}\frac{\cos(\lambda_n x)}{\lambda_n}(-1)^{n+1}\left\{T(t)-T(0)\exp\left(-\alpha\lambda_n^2 t\right)-\int_0^t\exp\left[-\alpha\lambda_n^2(t-\tau)\right]dT(\tau)d\tau\right\}$$

The closed-form expressions to introduce to Eq. (58) were obtained from Jolley [63], resulting in

$$T(x,t)=\left(\frac{2T_{\infty}}{L}\right)\sum_{n=1}^{\infty}\left(\frac{1}{\lambda_n}\right)(-1)^{n+1}\cos(\lambda_n x)\exp\left(-\alpha\lambda_n^2 t\right)+$$
$$+\left(\frac{2q''}{kL}\right)\sum_{n=1}^{\infty}\left(\frac{1}{\lambda^2{}_n}\right)\cos(\lambda_n x)\left[1-\exp\left(-\alpha\lambda_n^2 t\right)\right]+ \quad . \quad (59)$$
$$+T(t)-\sum_{n=1}^{\infty}\left\{\left(\frac{2}{L}\right)\frac{\cos(\lambda_n x)}{\lambda_n}(-1)^{n+1}\int_0^t\exp\left[-\alpha\lambda_n^2(t-\tau)\right]dT(\tau)d\tau+T(0)\exp\left(-\alpha\lambda_n^2 t\right)\right\}$$

In this form, the transient temperature distribution of the non-homogeneous problem converges at both boundary conditions. To perform the integral of Eq. (59), τ is used as a dummy integration variable, whereas t is treated as a constant. A MATLAB (MathWorks, Inc., Natick, MA, USA) code was used to solve the infinite series and the defined integral of Eq. (59) for values of λ_n from n = 1 to n = 10.

For the HHC, Figure 42 shows a comparison among (1) the exposed surface temperatures calculated from the Calibration Model using a heat flux of 57 kW/m^2, (2) case of Calibration Model using the heat flux calculated from Eq. (28a), and (3) the maximum experimentally measured temperatures (raw data), Figure 32. For the LHC, Figure 43 shows the comparison between (1) the exposed surface temperatures calculated from the Calibration Model using a heat flux of 20.3 kW/m^2, (2) case of the Calibration Model using the heat flux calculated from Eq. (28b), and (3) the experimental results of the burn tests under the LHC (raw data), Figure 33.

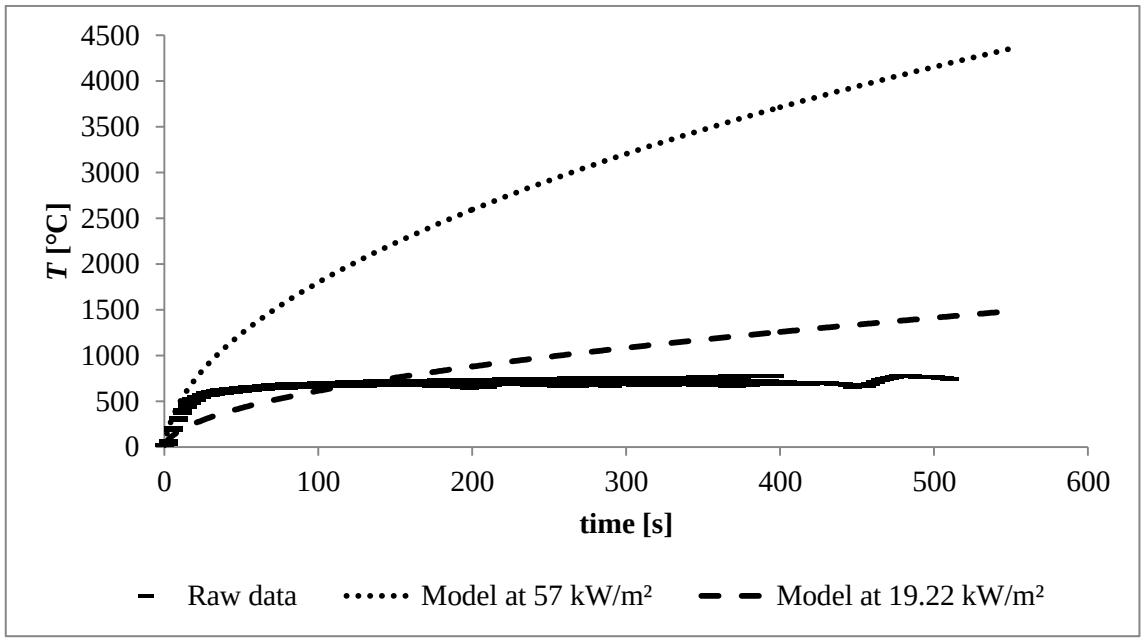

Figure 42 *Comparison of results of the exposed surface temperature form the Calibration Model and the experimentally measured temperatures under HHC.*

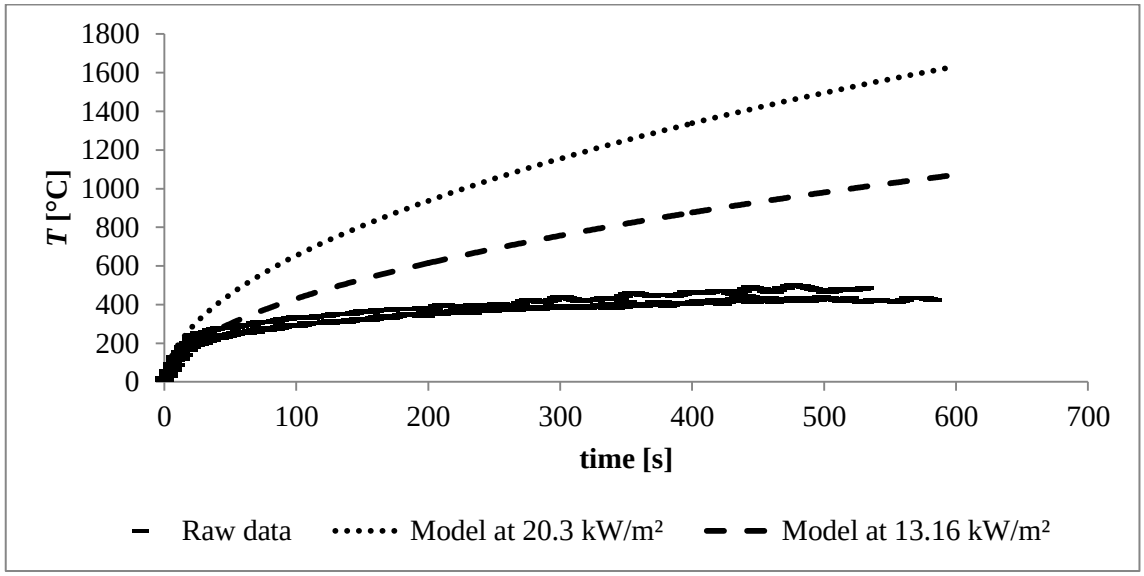

Figure 43 *Comparison of results of the exposed surface temperature form the Calibration Model and the experimentally measured temperatures under LHC.*

Table 7 show, for the HHC, the *TTI* reported in Figure 24 when compared with that obtained from the Calibration Model at the heat flux from Eq. (28a). The comparison was done by relating the time at which the predicted temperatures from the Calibration Model reached the reported surface temperature of the control material in Table 3.

Table 7 *Error of predicted TTI of the OSB under HHC.*

TTI of the exposed surface (Figure 24) @ T_{ig} = 749.03 ± 27.48°C (From Table 3)	*TTI* of the exposed surface @ $T_{ig} \approx 749°C$ (From Calibration Model)	$error = \left\| \frac{TTI_{exp} - TTI_{mod}}{TTI_{exp}} \right\| x100$
433 s	147	66 %

Likewise, for the LHC, Table 8 show the comparison of the *TTI* for the OSB reported in Figure 25 with the time at which the temperatures calculated from the Calibration Model using the heat flux from Eq. (28b) reached the reported surface temperatures of the OSB in Table 4.

Table 8 *Error of predicted TTI of the OSB under LHC.*

TTI of the exposed surface (Figure 25) @ T_{ig} = 449.01 ± 33.08˚C (From Table 4)	*TTI* of the exposed surface @ $T_{ig} \approx 449°C$ (From Calibration Model)	$error = \left\| \frac{TTI_{exp} - TTI_{mod}}{TTI_{exp}} \right\| x100$
544 s	109 s	80 %

High error was expected due to the thermal response of wooden material (principal composition of the OSB). The analytical model was not design to account for thermal degradation of the material such as carbon layer build up. Under heat fluxes below a critical heat flux value (CHF), such as 20 kW/m^2 [30], an enriched, porous carbon layer builds up over the surface of the solid material. This porous layer, which increases over time, allows

volatile gases from the virgin material to easily pass through it, but diminishes the heat transfer by conduction from the radiant heat load to the virgin material [41]; the carbon layer “insulates” the material reducing the temperature increase in the surface, thereby, increasing the temperature difference between the experimentally measured and the predicted temperatures. Also, under such heat fluxes, no singular increase in the surface temperature ensues which complicates the determination of the failure point through experimentally measured temperatures as for the LHC, thereby, increasing the error.

Figure 42 and 43 show how the experimentally measured temperatures had a steep increase at an early stage of the burn tests, but after approximately 600°C, temperatures increased gradually. In contrast, the predicted surface temperatures maintained a relatively constant increase rate due to the exponential terms in Eq. (59). Consequently, the constant increase of the predicted surface temperatures leaded to an overestimation of the *TTI*; it takes less time to the analytical model to reach the T_{ig}. However, considering the heat losses into the Calibration model better approximated the predicted surface temperatures to the experimentally measured temperatures. Therefore, the effective heat flux was considered for the Siding material Model.

6.3 Analytical results of the one-dimensional, finite length scale, transient heat conduction model for the siding materials (Siding material Model, SMM)

Figure 44 shows the modified schematic where the effective heat flux is incident to the siding material. To solve this model, Eq. (59) was applied by substituting the incident heat flux (*q''*) for the effective heat flux (q''_{EFF}) determined in Eq. (28a) and (28b) for the HHC and LHC, respectively.

$$T(x,t)=\left(\frac{2T_\infty}{L}\right)\sum_{n=1}^{\infty}\left(\frac{1}{\lambda_n}\right)(-1)^{n+1}\cos(\lambda_n x)\exp\left(-\alpha\lambda_n^2 t\right)+$$
$$+\left(\frac{2q''_{EFF}}{kL}\right)\sum_{n=1}^{\infty}\left(\frac{1}{\lambda^2{}_n}\right)\cos(\lambda_n x)\left[1-\exp\left(-\alpha\lambda_n^2 t\right)\right]+ \quad . \quad (60)$$
$$+T(t)-\sum_{n=1}^{\infty}\left\{\left(\frac{2}{L}\right)\frac{\cos(\lambda_n x)}{\lambda_n}(-1)^{n+1}\int_0^t\exp\left[-\alpha\lambda_n^2(t-\tau)\right]dT(\tau)d\tau+T(0)\exp\left(-\alpha\lambda_n^2 t\right)\right\}$$

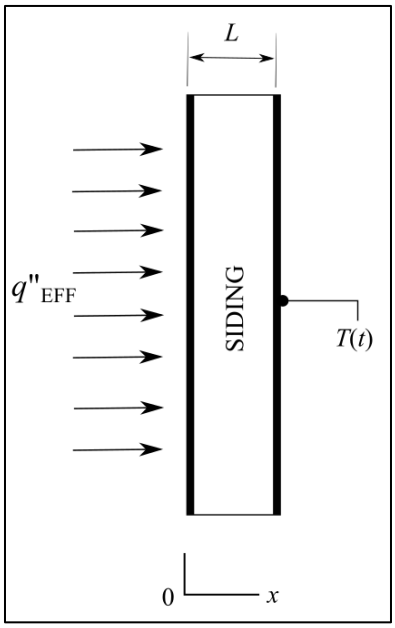

Figure 44 *Schematic of the heat transfer model for the siding materials.*

Results of the predicted *TTI* from this model were compared with one of the three approaches to predict ignition as described by Tran and Cohen [42] (Section 6).

The first approach, which was utilized in the Structure ignition assessment model (SIAM) [20], was based on the model developed by Janssens [43]. The second assumption requires the acquisition of transient mass loss data. Anderson and McDonald [64] used transient mass loss data that was obtained from a Cone Calorimeter test to validate the *TTI* of vegetative fuel samples that were subjected to heat fluxes of 13 and 42 kW/m^2. Nevertheless, such additional test was out of the scope of the present study. The third approach mentioned, however, was explored because (1) the formulations presented by Quintiere [47] are not designed or tested specifically for wooden materials and (2) the ignition theory of the ASTM E 1321 [19] is based on these formulations, which are:

$$t_{ig} = \frac{\rho c \delta \left(T_{ig} - T_{\infty} \right)}{q''} \text{ for a thermally thin material,} \tag{61}$$

$$t_{ig} = \frac{\left(\pi / 4 \right) k \rho c \left(T_{ig} - T_{\infty} \right)^2}{q''^2} \text{ for a thermally thick material.} \tag{62}$$

Thermally thin refers to a material that has a nearly uniform temperature during heating [41]. A criterion for a thermally thin material is

$$\text{Physical thickness} \leq \frac{2k \left(T_{ig} - T_{\infty} \right)}{q''} \tag{63}$$

Then, Eq. (63) was evaluated first and then, *TTI* was determined using Eq. (61) or Eq. (62) accordingly.

Eq. (60) compared to models from [43, 45] does not include truncated series expressions other than the closed-form expression utilized for the convergence of the boundary condition, nor is designed for a specific material.

As in Eq. (61) and (62), the methodology to compare the experimentally measured time to ignition (TTI_{test}) and those analytically determined (TTI_{SMM}), was done by relating the time at which the predicted temperatures obtained from Eq. (60) reached the reported surface temperatures in Table 3 and Table 4.

During the experiments, it was observed that the vinyl siding material was completely deformed at an early stage of the test, leaving the OSB directly exposed to the heat load. This deformation mechanism was not possible to reproduce with the model developed for this analysis. Thus, for the analytical solution, it was considered that the vinyl siding remained in place. However, due to the little thickness of the vinyl siding (1.27 mm), the "exposed surface" temperature values were compared with those from the interior surface of the OSB at the interface.

Table 9 and 10 show the results from the predicted *TTI* and its comparison with the formulations developed by Quintiere [47]. From Table 9, it can be observed that results for cedar and vinyl siding the analytically determined transient temperature profiles yielded in a more accurate prediction of the *TTI* using the Siding material Model than formulations developed by Quintiere [47]. Errors for the engineered wood and fibre cement board, although high, were lower as when Eq. (62) was used.

Table 9 *Predicted time to ignition (TTI) of siding materials under the HHC.*

Material	***TTI* from tests (TTI_{test}) Figure 24**	**Predicted *TTI* (TTI_{SMM}) @ T_{ig} from Table 3**	**Predicted TTI (Quintiere [47])**	*TTI* error (TTI_{test} vs. TTI_{SMM})	*TTI* error (TTI_{test} vs. **Quintiere [47]**)
Engineered wood	424 s	128 s	49.3 s (From Eq.(62))	69 %	88.4 %
Fibre cement board	1197 s	239 s	98.01 s (From Eq.(62))	80 %	91.8 %
Cedar siding	19 s	28 s	8.66 s (From Eq.(62))	47 %	54.4 %
Vinyl siding	69 s	63 s	22.83 s (From Eq.(61))	9.5 %	67 %

Table 10 *Predicted time to ignition (TTI) of siding materials under the LHC.*

Material	***TTI* from test (TTI_{test}) Figure 25**	**Predicted *TTI* (TTI_{SMM}) @ T_{ig} from Table 4**	**Predicted TTI (Quintiere [47])**	*TTI* error (TTI_{test} vs. TTI_{SMM})	*TTI* error (TTI_{test} vs. **Quintiere [47]**)
Engineered wood	1437 s	45 s	521.85 s (From Eq.(61))	97 %	64 %
Fibre cement board	N/A	N/A	N/A	N/A	N/A
Cedar siding	666 s	17 s	73 s (From Eq.(62))	97 %	89 %
Vinyl siding	1162 s	No solution	99.2 s (From Eq.(61))	N/A	91.7 %

In Table 10, similar errors were obtained between the Siding material Model and Eq. (61) and (62). However, the siding materials prototypes used were of larger dimensions than the samples used by Quintiere [47]. In this study, at three planks of 200 mm (8 in) by 533 mm (21 in) of a siding material were used for each siding material prototype while other bench-scale tests use small samples. The size of the samples that the apparatus uses in the ASTM E 1321, allows $155 \pm \frac{0}{5}$ mm by $155 \pm \frac{0}{5}$ mm specimens. CAN/ULC S114 requires a specimen size of 38 mm wide, 38 mmm thick, and 50 mm long [16]. In other tests, such as [40], the sample size was 64 mm^2 by 18 mm thick. There were no values to be shown for the FCB since this prototype did not fail under the LHC (as in Figure 25). Also, for the vinyl siding, it was not possible to obtain results under the LHC because an indetermination in Eq. (60); under this heating condition, the exponential terms of Eq. (60) increased significantly due to the longer duration of the test compared to the HHC.

Nonetheless, errors in Table 9 and 10 were high. Sources of error can be attributed to the thermal response of the OSB under heating conditions below a critical heat flux (Section 6.1); glowing ignition increases the error when measuring the failure point of the materials. Other sources of error can be tracked down to, for example, radiation scattering over the exposure surface. Non-uniform propagation of radiation lead to variation in the temperature profiles which were utilized to generate the correlations for the total heat loss calculations. For the mathematical model, the siding materials where considered as homogeneous and with constant thermal properties. Realistically, the chemical composition of these materials changes with temperature affecting its properties. In general, ignition temperatures published in the literature can only be taken as rough indications [41].

7. CONCLUSIONS AND REMARKS

The test methodology provided useful information to evaluate the performance of siding materials subjected to two radiant heat loads, a high heat flux condition (HHC) of 57 kW/m^2 and a low heat flux condition (LHC) of 20.3 kW/m^2. A failure criterion was established as the time to ignition of the prototype, where ignition could be due to flaming ignition of the siding material, or flaming or glowing ignition or the OSB behind the siding material. The transient temperature profiles from the thermocouples used provided quantitative evidence of the failure point of the prototypes. A variance analysis (ANOVA) confirmed that some siding materials were significantly different when comparing their time to ignition (*TTI*) and ignition temperatures (T_{ig}).

Under the HHC, it was found that the cedar and vinyl prototypes were the fastest prototypes to fail while the fibre cement board (FCB) prototype had the longest *TTI*. The FCB siding did not ignite; in contrast, flaming ignition occurred on the internal surface of the OSB at the interface of this prototype, this further illustrated the ignition resistance of the fibre cement board. No significant differences were obtained between the bare OSB and the engineered wood prototype, suggesting that using the latter to protect the sheathing materials of a composite will not represent any advantage.

Under the LHC, FCB prototype did not fail, cedar siding had the least *TTI*, and vinyl and engineered wood prototypes were found to have statistically similar *TTI*s; this result suggests that regardless of the different failure mechanism that these two materials experienced (flaming ignition or melting of the siding material); the time to reach the failure point was the same.

It was possible to simplify the analytical model developed through a quantitative basis estimating the heat losses that occurred during the burn tests of the control material. A comparison between the convective heat losses using gas volatiles and air properties showed that it was possible to neglect such losses since radiant heat losses were predominant. A better approximation was obtained between the experimentally measured temperatures and the analytically determined temperatures once the heat losses were included into the model. Based on this result, an effective heat flux was utilized to predict the *TTI* of the siding materials.

In spite of the more complex solution obtained to predict the *TTI* of the siding materials, lower error resulted when compared to other solutions proposed. Moreover, the model developed provided values with a similar level of error considering the dimensions of the samples that are typically tested under special laboratory equipment. Thus, the method developed to predict the *TTI* can be used to test the fire-resistance performance of other siding materials as it approaches to standard methods.

Derived from this study, recommendations can be provided as to not consider cedar, vinyl siding, or engineered wood for home protection in Wildland Urban Interface building provisions. Under a radiant heat load of 57 kW/m^2, which can be the irradiation emitted in a structure-to-structure fire scenario, cedar siding will ignite generating large flames that may aid the fire spread to an upper stories. Regarding the vinyl siding, the sheathing materials underneath vinyl siding can ignite within a minute, leaving no time to the first responders to control the fire spread. Engineered wood reached autoignition temperatures under 20 kW/m^2, whereas, in spite of the complete deformation of the vinyl siding, these prototypes did not reach autoignition temperatures. Conversely, if cedar, vinyl and

engineered wood siding materials are to be used in the WUI, stringent vegetation management around the buildings such as the FireSmart Priority Zones need to be ascertained.

Further research will be needed to determine the OSB and vinyl siding flammable gas volatiles that were derived from the exposure of the materials to radiant loads under stoichiometric conditions for comparison with measured composition of the flammable gas volatiles.

8. REFERENCES

[1] P. F. Hessburg and J. K. Agee, “Dry forests and wildland fires of the inland Northwest USA: Contrasting the landscape ecology of the pre-settlement and modem eras,” p. 23.

[2] “NFPA 1710, Standard for the Organization and Deployment of Fire Suppression Operations, Emergency Medical Operations, and Special Operations to the Public by Career Fire Departments.” National Fire Protection Association, 18-May-2019.

[3] R. White, P. Hessburg, S. Larkin, and M. Varner, “Smoke in a new era of fire.” US Department of Agriculture, Forest Service, Pacific Northwest Research Station, 2017.

[4] L. M. Johnston and M. D. Flannigan, “Mapping Canadian wildland fire interface areas,” *Int. J. Wildland Fire*, vol. 27, no. 1, p. 1, 2018.

[5] L. M. Johnston, “Mapping Canadian Wildland Fire Interface Areas,” Master of Science, University of Alberta, Edmonton, AB, Canada, 2016.

[6] KPMG, “Lessons Learned and Recommendations from the 2016 Horse River Wildfire,” KPMG LLP, Edmonton, AB, Canada, Jul. 2017.

[7] S. J. Prichard, C. S. Stevens-Rumann, and P. F. Hessburg, “Tamm Review: Shifting global fire regimes: Lessons from reburns and research needs,” *For. Ecol. Manag.*, vol. 396, pp. 217–233, Jul. 2017.

[8] S. E. Caton, R. S. P. Hakes, D. J. Gorham, A. Zhou, and M. J. Gollner, “Review of Pathways for Building Fire Spread in the Wildland Urban Interface Part I: Exposure Conditions,” *Fire Technol.*, vol. 53, no. 2, pp. 429–473, Mar. 2017.

[9] A. Westhaver, “Why some homes survived: Learning from the Fort McMurray wildland/urban interface fire disaster,” Institute for Catastrophic Loss Reduction, Toronto, ON, Canada, Mar. 2017.

[10] A. A. Mamuji and J. L. Rozdilsky, “Wildfire as an increasingly common natural disaster facing Canada: understanding the 2016 Fort McMurray wildfire,” *Nat. Hazards*, Sep. 2018.

[11] FireSmart Canada, “FireSmart Protecting your Community.” Partners in Protection, 2003.

[12] FireSmart Canada, “Firesmart Priority Zones 2017,” *FireSmart Canada*, 2017. [Online]. Available: https://www.firesmartcanada.ca/mdocs-posts/firesmart-priority-zones-2017/.

[13] S. Walkinshaw, D. Schroeder, and S. Hvenegaard, “Evaluating the effectiveness of FireSmart Priority Zones for Structure Protection | FireSmart Canada.” Jan-2012.

[14] A. Maranghides and E. J. Johnsson, “NIST Technical Note 1600: Residential Structure Separation Fire Experiments.” U.S Department of Commerce, National Institute of Standards and Technology, Aug-2008.

[15] *Alberta Building Code*, 9th ed., vol. 2. National Research Council of Canada, 2014.

[16] National Standard of Canada, “CAN/ULC S114-05 Standard Method of test for determination of non-combustibility in building materials.” Underwritters Laboratories of Canada, 2005.

[17] K. Biswas, D. Werth, and N. Gupta, “A Home Ignition Assessment Model Applied to Structures in the Wildland-Urban Interface,” presented at the Thermal Performance of the Exterior Envelopes of Whole Buildings XII International Conference, Clearwater, Florida, US, 2013, pp. 262–232.

[18] M. A. Dietenberger, "Ignitability Analysis of Siding Materials Using Modified Protocol for Lift Apparatus," *Fire Mater.*, vol. 20, pp. 115–121, 1996.
[19] ASTM 1321, "Standard Test Method for Determining Material Ignition and Flame Spread Properties," ASTM International, West Conshohocken, PA, United States, Standard, 2013.
[20] J. D. Cohen, "Structure ignition assessment model (SIAM)," presented at the Biswell Symposium: Fire issues and solutions in Urban Interface and Wildland Ecosystems, Walnut Creek, California, 1995, vol. 158, pp. 85–92.
[21] S. L. Quarles and M. Sindelar, "Wildfire Ignition Resistant Home Design (WIRHD) Program: Full-scale Testing and Demonstration Final Report," Insurance Institute for Business & Home Safety, Richburg, South Carolina, USA, Dec. 2011.
[22] S. L. Manzello, S. Suzuki, and Y. Hayashi, "Exposing siding treatments, walls fitted with eaves, and glazing assemblies to firebrand showers," *Fire Saf. J.*, vol. 50, pp. 25–34, May 2012.
[23] S. Suzuki and S. L. Manzello, "Firebrand production from building components fitted with siding treatments," *Fire Saf. J.*, vol. 80, pp. 64–70, Feb. 2016.
[24] S. L. Manzello, S. Suzuki, and D. Nii, "Full-Scale Experimental Investigation to Quantify Building Component Ignition Vulnerability from Mulch Beds Attacked by Firebrand Showers," *Fire Technol.*, vol. 53, no. 2, pp. 535–551, Mar. 2017.
[25] B. Bahrani, V. Hemmati, A. Zhou, and S. L. Quarles, "Effects of natural weathering on the fire properties of intumescent fire-retardant coatings," *Fire Mater.*, vol. 42, no. 4, pp. 413–423, 2018.
[26] A. Zhou, "Performance evaluation of ignition-resistant materials for structure fire protection in the WUI," in *Proceedings of the 13th Int. Conference and Exhibition on Fire and Materials*, San Francisco, CA, 2013, pp. 355–366.
[27] M. Dobson, "Vinyl Siding: Fire-safe and right for Fort McMurray," *Vinyl Institute of Canada*. [Online]. Available: http://vinylinstituteofcanada.com/vinyl-siding-fire-safe-and-right-for-fort-mcmurray/. [Accessed: 11-Jan-2019].
[28] U.S Department of Homeland Security, "Home Builder´s Guide to Construction in Wildfire Zones." Sep-2008.
[29] C. K. Randall, "Fire in the Wildland-Urban Interface: Understanding fire behavior." University of Florida IFAS Extension, USDA Forest Service, 2003.
[30] S. Hirle and K. Balog, "The Effect of the Heat Flux on the Self-Ignition of Oriented Strand Board," *Res. Pap. Fac. Mater. Sci. Technol. Slovak Univ. Technol.*, vol. 25, no. 40, pp. 123–129, Jun. 2017.
[31] F. Takahashi, T. M. Murray, A. Abbott, S.-Y. Hsu, J. S. T'Ien, and S. L. Olson, "Performance evaluation criteria of fire blanket materials for structure protection in wildland-urban interface fires," presented at the Fall Meeting of the Eastern States Section of the Combustion Institute, 2009, pp. 645–650.
[32] S. Sudheer, L. Kumar, B. S. Manjunath, A. Pasi, G. Meenakshi, and S. V. Prabhu, "Fire safety distances for open pool fires," *Infrared Phys. Technol.*, vol. 61, pp. 265–273, Nov. 2013.
[33] N. N. Daeid, "Fire Investigation," 1st Ed., CRC Press, 2005, pp. 6–12.
[34] X. Silvani and F. Morandini, "Fire spread experiments in the field: Temperature and heat fluxes measurements," *Fire Saf. J.*, vol. 44, no. 2, pp. 279–285, Feb. 2009.

[35] California Department of Forestry & Fire Protection, “Fire Engineering - Building Materials Listing Program,” Fontana, California, US, Listing Service 8140–2026:0001, Jul. 2018.
[36] Louisiana-Pacific Corporation, “LP SmartSide,” *LP Building Solutions*, 2019. [Online]. Available: https://lpcorp.com/blog/did-you-know-the-lp-smartside-limited-warranty-beats-hardie-s-by-20-years.
[37] S. A. Anderson, “Quantification of Performance of Wildfire Chemicals using Custom-Built Heat Flux Sensors,” Master of Science, University of Alberta, Edmonton, AB, Canada, 2015.
[38] Y. A. Çengel and A. Ghajar, *Heat and mass transfer fundamentals and applications*, Fifth Edition. McGraw-Hill Education, 2015.
[39] “Dual Laser Video IR Video Thermometer Model VIR50 User’s Manual.” FLIR Systems, Inc., 2014.
[40] Y. Li and D. D. Drysdale, “Measurement Of The Ignition Temperature Of Wood,” *Fire Saf. Sci.*, vol. 1, pp. 380–385, 1992.
[41] J. G. Quintiere, “Principles of Fire Behavior,” 2nd. Edition., FL, USA: Taylor and Francis Group, 2017.
[42] H. C. Tran, J. D. Cohen, and R. A. Chase, “Modeling ignition of structures in the Wildland/Urban Interface fires,” presented at the 1st International Fire and Materials Conference, Arlington, VA, London, UK, 1992, pp. 253–262.
[43] M. Janssens, “A thermal model for piloted ignition of wood including variable thermophysiscal properties,” in *Proceedings of the 3rd International Symposium*, University of Edinburg, Scotland, 1991, vol. XVIII, pp. 167–176.
[44] S. V. Glass, V. Kochkin, S. C. Drumheller, and L. Barta, “Moisture Performance of Energy-Efficient and Conventional Wood-Frame Wall Assemblies in a Mixed-Humid Climate,” *Buildings*, vol. 5, no. 3, pp. 759–782, Sep. 2015.
[45] A. Lamorlette and F. Candelier, “Thermal behavior of solid particles at ignition: Theoretical limit between thermally thick and thin solids,” *Int. J. Heat Mass Transf.*, vol. 82, pp. 117–122, Mar. 2015.
[46] L. Jiji, “Heat Conduction,” in *Heat Conduction*, 3rd Edition., Berlin: Springer, 2009, pp. 132–137.
[47] J. G. Quintiere, “A theoretical basis for flammability properties,” *Fire Mater.*, vol. 30, no. 3, pp. 175–214, 2006.
[48] M. J. Spearpoint and J. G. Quintiere, “Predicting the piloted ignition of wood in the cone calorimeter using an integral model - effect of species, grain orientation and heat flux,” *Fire Saf. J.*, p. 25, 2001.
[49] L. Shi and M. Y. L. Chew, “A review of fire processes modeling of combustible materials under external heat flux,” *Fuel*, vol. 106, pp. 30–50, Apr. 2013.
[50] T. L. Bergman, A. S. Lavine, F. P. Incropera, and D. P. Dewitt, *Introduction to heat transfer*, 6th Ed. Hoboken, NJ, USA: John Wiley & Sons Inc., 2011.
[51] L. Shi, M. Y. L. Chew, X. Liu, X. Cheng, B. Wang, and G. Zhang, “An experimental and numerical study on fire behaviors of charring materials frequently used in buildings,” *Energy Build.*, vol. 138, pp. 140–153, Mar. 2017.
[52] K. W. Ragland, D. J. Aerts, and A. J. Baker, “Properties of wood for combustion analysis,” *Bioresour. Technol.*, vol. 37, no. 2, pp. 161–168, Jan. 1991.
[53] B. E. Poling, J. M. Prausnitz, and J. P. O’Connell, *The properties of gases and liquids*, 5th Ed. USA: McGraw-Hill Education, 2001.

[54] M. Hishler, “Fire properties of polyvinyl chloride.” The Vinyl Institute, 2017.
[55] Product Stewardship, “Prime Plus Primer Safety Data Sheet.” Valspar Industries, Dec-2016.
[56] R. Refai, “Quantification of performance of wildfire chemicals using a custom-built sensible enthalpy rise calorimeter,” Master of Science, University of Alberta, Edmonton, AB, Canada, 2017.
[57] A. A. F. Peters and R. Weber, “Mathematical Modeling of a 2. 25 MW Swirling Natural Gas Flame. Part 1: Eddy Break-up Concept for Turbulent Combustion; Probability Density Function Approach for Nitric Oxide Formation,” *Combust. Sci. Technol.*, vol. 110–111, no. 1, pp. 67–101, Dec. 1995.
[58] P. C. Timusk, “An investigation of the moisture sorption and permeability properties of mill-fabricated oriented strandboard,” Doctor of Philosophy, Univeristy of Toronto, 2008.
[59] M. J. Moran and H. N. Shapiro, *Fundemanetals of engineering thermodynamics*, 5th Ed. Chicherster, England: John Wiley & Sons Inc., 2006.
[60] J. B. Lewis and D. A. Linzer, “Estimating regression models in which the dependent variable is based on estimates,” *Polit. Anal.*, vol. 13, pp. 345–364, 2005.
[61] R. J. Leatherbarrow, “Using linear and non-linear regression to fit biochemical data,” *Trends Biochem. Sci.*, vol. 15, no. 12, pp. 455–458, Dec. 1990.
[62] M. N. Özişik, *Heat Conduction*, Second Ed. John Wiley & Sons Inc., 1980.
[63] L. B. W. Jolley, “Summation of Series 2nd review,” in *Summation of series*, 2nd Ed., New York: Dover Publications, Inc., 1961, pp. 96, Case 506.
[64] S. A. Anderson and A. G. McDonald, “Performance testing of wildland fire chemicals using a custom-built heat flux sensor,” *J. Fire Sci.*, vol. 33, no. 6, pp. 473–492, Nov. 2015.

APPENDIX A: Code used for solving the heat transfer model

Code for the HHC

```
%%Declaring variables for x coordinate and time
syms t x te
T_amb=20; %°C

%%MATERIAL PROPERTIES, transform to vectors: k[i]=k[1]...k[5]
%%1=OSB, 2=EW, 3=FCB, 4=CDR, 5=VNL
L=[0.0111125 0.0111125 0.0111125 0.0174625 0.00127]; %m
k=[0.092 0.14 0.245 0.085 0.1]; %W/m-°C
cp=[1880 1300 840 1880 840]; %J/kg-°C
den=[650 800 1380 336 1470]; %kg/m3

%%Regressions for Interface temperature for HHC.
%%Regressions considering max temps
TI1=19.919*exp(0.0055*t);
TI2=4E-08*t^4-3E-05*t^3+0.0062*t^2+0.0882*t+6.941;
TI3=0.4667*t+33.807;
TI4=0.172*t+17.859;
TI5=0.0118*t^2+3.179*t+15.712;

TI=[TI1 TI2 TI3 TI4 TI5]; %Vector containing regressions for each material
[zTI1, zTI2, zTI3, zTI4, zTI5] = zeroTI(0);
zTI=[zTI1 zTI2 zTI3 zTI4 zTI5]; %Vector containing regressions evaluated @t=0

%%HEAT LOSSES UNDER HHC USING GAS VOLATILES PROPERTIES
int_qExp_conv=int(2e-9*te^3-2e-6*te^2+7e-4*te+0.15,te,[0 500]);
int_qExp_rad1=int(0.066*te^2-0.3*te+0.66,te,[0 20]);
int_qExp_rad2=int(7e-7*te^3-7e-4*te^2+0.22*te+19.9,te,[21 500]);
int_qBack_conv=int(2e-8*te^3-5e-6*te^2+0.001*te-0.024,te,[0 500]);
int_qBack_rad=int(0.03*exp(0.012*te),te,[0 500]);
totalExp_conv=int_qExp_conv/500; %kW/m2
totalExp_rad=(int_qExp_rad1+int_qExp_rad2)/500; %kW/m2
totalBack_conv=int_qBack_conv/500; %kW/m2
totalBack_rad=int_qBack_rad/500; %kW/m2
Exp_totLoss=totalExp_conv+totalExp_rad; %kW/m2
Back_totLoss=totalBack_conv+totalBack_rad; %kW/m2

%%HEAT LOSSES UNDER HHC USING AIR PROPERTIES
int_qExp_c1=int(0.22*te-0.14,te,[0 20]);
int_qExp_c2=int(4e-8*te^3-4e-5*te^2+0.012*te+4.22,te,[21 500]);
totalExp_c=(int_qExp_c1+int_qExp_c2)/500; %kW/m2
Exp_totLoss_air=totalExp_c+totalExp_rad; %kW/m2

%%HEAT LOAD
q_HHC=57000-totalExp_rad*1000; %W/m2 %%For unit agreement
%%q_HHC=57000;

ii=1:5;  %TO CONTROL MATERIALS LOOP
nn=1:10; %TO CONTROL SUMMATION LOOP

%%Initializing variables
alfa=sym(zeros(1,length(ii)));
sum_Term1=sym(zeros(1,length(ii)));
sum_Term2=sym(zeros(1,length(ii)));
sum_Term3=sym(zeros(1,length(ii)));
T=sym(zeros(1,length(ii)));
```

```
for i=1:length(ii);
alfa(i)=k(i)/(cp(i)*den(i)); %Thermal diffusivity

sumTerm1=0;
sumTerm2=0;
sumTerm3=0;

    for n=1:length(nn);
        lambda=((2*n-1)*pi)/(2*L(i)); %Eigenvalue
        %Temperature distribution using Green's function: T=Term1+Term2+Term3
        %Summation for Term1
        Term1=(1/lambda)*((-1)^(n+1))*cos(lambda*x)*exp(-alfa(i)*(lambda^2)*t);
        sumTerm1=sumTerm1+Term1;
        %Summation for Term2
        Term2=(1/lambda^2)*cos(lambda*x)*(1-exp(-alfa(i)*(lambda^2)*t));
        sumTerm2=sumTerm2+Term2;
        %Summation for Term3
        etao=exp(alfa(i)*(lambda^2)*t);
        multi=diff(TI(i))*etao;
        int_multi=int(multi,t,[0 t]);
        Term3=(1/lambda)*cos(lambda*x)*((-1)^(n+1))*exp(-
alfa(i)*(lambda^2)*t)*(zTI(i)+int_multi);
        sumTerm3=sumTerm3+Term3;
    end
%%Terms are assigned for each material
sum_Term1(i)=sumTerm1;
sum_Term2(i)=sumTerm2;
sum_Term3(i)=sumTerm3;

%%Transient temperature distribution for each material
T(i)=(2*T_amb/L(i))*sum_Term1(i)+(2*q_HHC/(k(i)*L(i)))*sum_Term2(i)+TI(i)-
(2/L(i))*sum_Term3(i);
end

        %%%%%%%%%% EVALUATION OF THE TEMPERATURE DISTRIBUTIONS %%%%%%%%%%
%1=OSB, 2=EW, 3=FCB, 4=CDR, 5=VNL
d=3; %Variable to define divisions in material
time1=550; %Variable to define time for OSB
xp1=linspace(0,L(1),d);
TOSB=zeros(length(d),length(time1+1));
 for j=1:d;
    x=xp1(j);
    for t=0:time1;
        TOSB(j,t+1)=eval(T(1)); %Evaluating temperature distribution of the OSB
    end
 end

time2=500; %Variable to define time for EW
xp2=linspace(0,L(2),d);
TEW=zeros(length(d),length(time2+1));
 for j=1:d;
    x=xp2(j);
    for t=0:time2;
        TEW(j,t+1)=eval(T(2)); %Evaluating temperature distribution of the EW
    end
 end

time3=1250; %Variable to define time for FCB
xp3=linspace(0,L(3),d);
TFCB=zeros(length(d),length(time3+1));
 for j=1:d;
    x=xp3(j);
    for t=0:time3;
```

```
        TFCB(j,t+1)=eval(T(3)); %Evaluating temperature distribution of the FCB
    end
 end

time4=150; %Variable to define time for CDR
xp4=linspace(0,L(4),d);
TCDR=zeros(length(d),length(time4+1));
 for j=1:d;
    x=xp4(j);
    for t=0:time4;
        TCDR(j,t+1)=eval(T(4)); %Evaluating temperature distribution of the CDR
    end
 end

time5=200; %Variable to define time for VNL
xp5=linspace(0,L(5),d);
TVNL=zeros(length(d),length(time5+1));
 for j=1:d;
    x=xp5(j);
    for t=0:time5;
        TVNL(j,t+1)=eval(T(5)); %Evaluating temperature distribution of the VNL
    end
 end
```

Code for the LHC

```
%%Declaring variables for x coordinate and time
syms t x te
T_amb=20; %°C

%MATERIAL PROPERTIES, transform to vectors: k[i]=k[1]...k[5]
%1=OSB, 2=EW, 3=FCB, 4=CDR, 5=VNL
L=[0.0111125 0.0111125 0.0111125 0.0174625 0.00127]; %m
k=[0.092 0.14 0.245 0.085 0.1]; %W/m-°C
cp=[1880 1300 840 1880 840]; %J/kg-°C
den=[650 800 1380 336 1470]; %kg/m3

%Regressions for Back temperature for LHC
%%Regressions considering max temps
TI1=0.145*t+17.54;
TI2=7E-05*t^2+0.0455*t+29.634;
TI3=-8E-05*t^2+0.2549*t+23.17;
TI4=4E-07*t^3-0.0005*t^2+0.4049*t+6.5052;
TI5=1E-07*t^3-0.0005*t^2+0.5969*t+25.295;

TI=[TI1 TI2 TI3 TI4 TI5]; %Vector containing regressions for each material
[zTI1, zTI2, zTI3, zTI4, zTI5] = zeroTB(0);
zTI=[zTI1 zTI2 zTI3 zTI4 zTI5]; %Vector containing regressions evaluated @t=0

%HEAT LOSSES UNDER LHC USING GAS VOLATILES PROPERTIES
int_qExp_conv=int(-3e-7*te^2+3e-4*te+0.03,te,[0 600]);
int_qExp_rad1=int(0.087*te-0.118,te,[0 14]);
int_qExp_rad2=int(-4e-5*te^2+0.035*te+1.47,te,[15 600]);
int_qBack_conv=int(5e-7*te^2+6e-4*te-0.018,te,[0 600]);
int_qBack_rad=int(7e-7*te^2+7e-4*te-0.01,te,[0 600]);
totalExp_conv=int_qExp_conv/600; %kW/m2
totalExp_rad=(int_qExp_rad1+int_qExp_rad2)/600; %kW/m2
totalBack_conv=int_qBack_conv/600; %kW/m2
totalBack_rad=int_qBack_rad/600; %kW/m2
Exp_totLoss=totalExp_conv+totalExp_rad; %kW/m2
Back_totLoss=totalBack_conv+totalBack_rad; %kW/m2

%%HEAT LOSSES UNDER LHC USING AIR PROPERTIES
int_qExp_c1=int(0.066*te-0.07,te,[0 14]);
int_qExp_c2=int(-9e-6*te^2+0.007*te+1.35,te,[15 600]);
totalExp_c=(int_qExp_c1+int_qExp_c2)/600; %kW/m2
Exp_totLoss_air=totalExp_c+totalExp_rad; %kW/m2

%HEAT LOAD
%%q_LHC=20300-totalExp_rad*1000; %W/m2
q_LHC=20300; %W/m2

ii=1:5;  %TO CONTROL MATERIALS LOOP
nn=1:10; %TO CONTROL SUMMATION LOOP

%Initializing variables
alfa=sym(zeros(1,length(ii)));
sum_Term1=sym(zeros(1,length(ii)));
sum_Term2=sym(zeros(1,length(ii)));
sum_Term3=sym(zeros(1,length(ii)));
T=sym(zeros(1,length(ii)));

for i=1:length(ii);
alfa(i)=k(i)/(cp(i)*den(i)); %Thermal diffusivity

sumTerm1=0;
sumTerm2=0;
```

```
sumTerm3=0;

    for n=1:length(nn);
        lambda=((2*n-1)*pi)/(2*L(i)); %Eigenvalue
        %Temperature distribution using Green's function: T=Term1+Term2+Term3
        %Summation for Term1
        Term1=(1/lambda)*((-1)^(n+1))*cos(lambda*x)*exp(-alfa(i)*(lambda^2)*t);
        sumTerm1=sumTerm1+Term1;
        %Summation for Term2
        Term2=(1/lambda^2)*cos(lambda*x)*(1-exp(-alfa(i)*(lambda^2)*t));
        sumTerm2=sumTerm2+Term2;
        %Summation for Term3
        etao=exp(alfa(i)*(lambda^2)*t);
        multi=diff(TI(i))*etao;
        int_multi=int(multi,t,[0 t]);
        Term3=(1/lambda)*cos(lambda*x)*((-1)^(n+1))*exp(-
alfa(i)*(lambda^2)*t)*(zTI(i)+int_multi);
        sumTerm3=sumTerm3+Term3;
    end
%Terms are assigned for each material
sum_Term1(i)=sumTerm1;
sum_Term2(i)=sumTerm2;
sum_Term3(i)=sumTerm3;

%Transient temperature distribution for each material
T(i)=(2*T_amb/L(i))*sum_Term1(i)+(2*q_LHC/(k(i)*L(i)))*sum_Term2(i)+TI(i)-
(2/L(i))*sum_Term3(i);
end

        %%%%%%%%%% EVALUATION OF THE TEMPERATURE DISTRIBUTIONS %%%%%%%%%%

%1=OSB, 2=EW, 3=FCB, 4=CDR, 5=VNL
d=3; %Variable to define divisions in material
time1=600; %Variable to define time for OSB
xp1=linspace(0,L(1),d);
TOSB=zeros(length(d),length(time1+1));
 for j=1:d;
    x=xp1(j);
    for t=0:time1;
        TOSB(j,t+1)=eval(T(1)); %Evaluating temperature distribution of the OSB
    end
 end

time2=1600; %Variable to define time for EW
xp2=linspace(0,L(2),d);
TEW=zeros(length(d),length(time2+1));
 for j=1:d;
    x=xp2(j);
    for t=0:time2;
        TEW(j,t+1)=eval(T(2)); %Evaluating temperature distribution of the EW
    end
 end

time3=1900; %Variable to define time for FCB
xp3=linspace(0,L(3),d);
TFCB=zeros(length(d),length(time3+1));
 for j=1:d;
    x=xp3(j);
    for t=0:time3;
        TFCB(j,t+1)=eval(T(3)); %Evaluating temperature distribution of the FCB
    end
 end
```

```
time4=750; %Variable to define time for CDR
xp4=linspace(0,L(4),d);
TCDR=zeros(length(d),length(time4+1));
 for j=1:d;
    x=xp4(j);
    for t=0:time4;
        TCDR(j,t+1)=eval(T(4)); %Evaluating temperature distribution of the CDR
    end
 end

time5=1200; %Variable to define time for VNL
xp5=linspace(0,L(5),d);
TVNL=zeros(length(d),length(time5+1));
 for j=1:d;
    x=xp5(j);
    for t=0:time5;
        TVNL(j,t+1)=eval(T(5)); %Evaluating temperature distribution of the VNL
    end
 end
```

APPENDIX B: Code used to obtain the heat losses and the multi-component gas and air properties

```
PROCEDURE BACKTEMP (t:Tback)
   Tback:=0.1448*t+17.542 "°C"
END

PROCEDURE EXTEMP (t:Tig)
IF (t<15) THEN
   Tig:=10.02*t + 16.13 [°C]
ELSE
   Tig:=1*10^(-06)*t^3 - 0.002*t^2 + 1.128*t + 201.85 [°C]
ENDIF
END

PROCEDURE PROPERTIES (Tsurf,T_a,P_amb,L,g,vel:Tf,
beta,Pr_air,mu_air,rho_air,nu_air,k_air,Ra,Gr,Re,comb) "FOR AIR PROPERTIES"
Tf=(Tsurf+T_a)/2
beta=1/(Tf+273.15) "K"
Pr_air=Prandtl(Air_ha,T=Tf,P=P_amb)
mu_air=Viscosity(Air_ha,T=Tf,P=P_amb)
rho_air=Density(Air_ha,T=Tf,P=P_amb)
nu_air=mu_air/rho_air
k_air=Conductivity(Air_ha,T=Tf,P=P_amb)
Ra=(g*beta*abs(Tsurf-T_a)*(L^3)*Pr_air)/nu_air^2
Gr=Ra/Pr_air
Re=vel*L/nu_air
comb=Gr/(Re^2)
END

PROCEDURE COMBINEDFLOW
(comb,Ra,Pr,Re,L,kf,ess,k,Tig,T_a:NU,h,Bi,NUre,NUra,q_loss)
IF (comb>1) THEN "No forced convection effects"
   NU:=(0.825+((0.387*Ra^(1/6))/(1+(0.492/Pr)^(9/16))^(8/27)))^2
   h:=NU*kf/L "W/m2-K"
   Bi:=h*ess/2*k
   NUre:=0
   NUra:=0
   q_loss:=h*(Tig-T_a)/1000 "kW/m2"
ELSE
     IF (Re<5*10^5) THEN
     NUre:=0.453*(Re^0.5)*(Pr)^(1/3) "Laminar regime"
     ELSE
     NUre:=0.0308*(Re^0.8)*(Pr)^(1/3) "Turbulent regime"
   ENDIF
   NUra:=(0.825+((0.387*Ra^(1/6))/(1+(0.492/Pr)^(9/16))^(8/27)))^2
   NU:=(NUre^3+NUra^3)^(1/3)
   h:=NU*kf/L "W/m2-K"
   Bi:=h*ess/2*k
   q_loss:=h*(Tig-T_a)/1000 "kW/m2"
ENDIF
END

"!GENERAL PROPERTIES"
T_amb= 20 "°C"
P_amb=0.99 "bar"
L=21*0.0254 "m"
g=9.81 "m/s2"
q_radHHC=57 "kW/m2"
q_radLHC=20.3 "kW/m2"
```

```
vel=0.2 [m/s]
sigma=5.67*10^(-8) "W/m-K^4"

"!OSB: CONTROL MATERIAL"
ess_OSB=(7/16)*0.0254 "m"
k_OSB=0.092 "W/m-K"

"! STOICHIOMETRIC COEFFICIENTS OF VOLATILES FOR OSB PYROLYSIS/COMBUSTION:
[kg]CxHy+v1*O2 --> (28*yC/12)*CO+(18/2)*(1-yC)*H2O
[kg] CO+v2*O2 --> (1+v2)*CO2"
yC=0.502 "WEIGHT OF CARBON IN OSB"
vol_OSB=ess_OSB*L^2 "m3"
rho_OSB=650 "kg/m3"
m_OSB=rho_OSB*vol_OSB "kg"

mfC=0.502
mfCO=(28*mfC/12)*m_OSB
mfH2O=((18/2)*(1-mfC))*m_OSB
mfCO2=(1+16/28)*m_OSB
m_gases=mfCO2+mfH2O+mfCO
MCO2=MolarMass(CarbonDioxide)
MCO=MolarMass(CarbonMonoxide)
MH2O=MolarMass(H2O)
nCO=(mfCO/MCO)
nH2O=(mfH2O/MH2O)
nCO2=(mfCO2/MCO2)
n_gases=nCO2+nH2O+nCO
yCO=nCO/n_gases
yH2O=nH2O/n_gases
yCO2=nCO2/n_gases
CALL EXTEMP (TIME: Tig_OSB)
muCO=Viscosity(CarbonMonoxide,T=Tig_OSB,P=yCO*P_amb)
muH2O=Viscosity(Water,T=Tig_OSB,P=yH2O*P_amb)
muCO2=Viscosity(CarbonDioxide,T=Tig_OSB,P=yCO2*P_amb)
kCO=Conductivity(CarbonMonoxide,T=Tig_OSB,P=yCO*P_amb)
kH2O=Conductivity(Water,T=Tig_OSB,P=yH2O*P_amb)
kCO2=Conductivity(CarbonDioxide,T=Tig_OSB,P=yCO2*P_amb)
phi12=((1+((muCO/muH2O)^(0.5))*(MH2O/MCO)^(1/4))^2)/(8*(1+MCO/MH2O))^0.5
phi13=((1+((muCO/muCO2)^(0.5))*(MCO2/MCO)^(1/4))^2)/(8*(1+MCO/MCO2))^0.5
phi21=((1+((muH2O/muCO)^(0.5))*(MH2O/MCO)^(1/4))^2)/(8*(1+MH2O/MCO))^0.5
phi23=((1+((muH2O/muCO2)^(0.5))*(MCO2/MH2O)^(1/4))^2)/(8*(1+MH2O/MCO2))^0.5
phi31=((1+((muCO2/muCO)^(0.5))*(MCO/MCO2)^(1/4))^2)/(8*(1+MCO2/MCO))^0.5
phi32=((1+((muCO2/muH2O)^(0.5))*(MH2O/MCO2)^(1/4))^2)/(8*(1+MCO2/MH2O))^0.5
mu_gases=(yCO*muCO)/(yCO+yH2O*phi12+yCO2*phi13)+(yH2O*muH2O)/(yCO*phi21+yH2O+yCO2
*phi23)+(yCO2*muCO2)/(yCO*phi31+yH2O*phi32+yCO2)

k12=((1+((kCO/kH2O)^(0.5))*(MH2O/MCO)^(1/4))^2)/(8*(1+MCO/MH2O))^0.5
k13=((1+((kCO/kCO2)^(0.5))*(MCO2/MCO)^(1/4))^2)/(8*(1+MCO/MCO2))^0.5
k21=((1+((kH2O/kCO)^(0.5))*(MH2O/MCO)^(1/4))^2)/(8*(1+MH2O/MCO))^0.5
k23=((1+((kH2O/kCO2)^(0.5))*(MCO2/MH2O)^(1/4))^2)/(8*(1+MH2O/MCO2))^0.5
k31=((1+((kCO2/kCO)^(0.5))*(MCO/MCO2)^(1/4))^2)/(8*(1+MCO2/MCO))^0.5
k32=((1+((kCO2/kH2O)^(0.5))*(MH2O/MCO2)^(1/4))^2)/(8*(1+MCO2/MH2O))^0.5
k_gases=(yCO*kCO)/(yCO+yH2O*k12+yCO2*k13)+(yH2O*kH2O)/(yCO*k21+yH2O+yCO2*k23)+(yC
O2*kCO2)/(yCO*k31+yH2O*k32+yCO2)

cpCO=Cp(CarbonMonoxide,T=Tig_OSB,P=yCO*P_amb)
cpH2O=Cp(Water,T=Tig_OSB,P=yH2O*P_amb)
cpCO2=Cp(CarbonDioxide,T=Tig_OSB,P=yCO2*P_amb)
cp_gases=mfCO*cpCO+mfH2O*cpH2O+mfCO2*cpCO2

vCO=Volume(CarbonMonoxide,T=Tig_OSB,P=yCO*P_amb)
vH2O=Volume(Water,T=Tig_OSB,P=yH2O*P_amb)
vCO2=Volume(CarbonDioxide,T=Tig_OSB,P=yCO2*P_amb)
```

```
v_gases=mfCO*vCO+mfH2O*vH2O+mfCO2*vCO2
rho_gases=1/v_gases
nu_gases=mu_gases/rho_gases
Pr_gases=mu_gases*cp_gases/k_gases

"CALCULATION FOR GAS-MIXTURE PROPERTIES"
Tf1=(Tig_OSB+T_amb)/2
beta1=1/(Tf1+273.15) "K"
Ra1=(g*beta1*abs(Tig_OSB-T_amb)*(L^3)*Pr_gases)/nu_gases^2
Gr1=Ra1/Pr_gases
Re1=vel*L/nu_gases
comb1=Gr1/(Re1^2)

CALL COMBINEDFLOW
(comb1,Ra1,Pr_gases,Re1,L,k_gases,ess_OSB,k_OSB,Tig_OSB,T_amb:Nu1,h1,Bi_OSB,NUre1
,NUra1,q_convlossOSB)
q_radlossOSB=0.8*sigma*((Tig_OSB+273.15)^4-(T_amb+273.15)^4)/1000 "kW/m2"
q_ExpLoss=q_convlossOSB+q_radlossOSB "kW/m2"
convLoss1=(q_convlossOSB/q_ExpLoss)*100 "PERCENTAGE OF THE CONVECTIVE LOSSES AT
EXPOSED SURF"
radLoss1=(q_radlossOSB/q_ExpLoss)*100 "PERCENTAGE OF THE RADIANT LOSSES AT
EXPOSED SURF"

CALL BACKTEMP (TIME: Tback_OSB)
CALL PROPERTIES (Tback_OSB,T_amb,P_amb,L,g,vel:Tf11,
beta11,Pr_air11,mu_air11,rho_air11,nu_air11,k_air11,Ra11,Gr11,Re11,comb11)
CALL COMBINEDFLOW
(comb11,Ra11,Pr_air11,Re11,L,k_air11,ess_OSB,k_OSB,Tback_OSB,T_amb:Nu11,h11,Bi_OS
Bb,NUre11,NUra11,q_convlossOSBb)
q_radlossOSBb=0.9*sigma*((Tback_OSB+273.15)^4-(T_amb+273.15)^4)/1000 "kW/m2"
q_BackLoss=q_convlossOSBb+q_radlossOSBb "kW/m2"
convLoss2=(q_convlossOSBb/q_BackLoss)*100 "PERCENTAGE OF THE CONVECTIVE LOSSES AT
BACK SURF"
radLoss2=(q_radlossOSBb/q_BackLoss)*100 "PERCENTAGE OF THE RADIANT LOSSES AT BACK
SURF"
```